Institut für Angewandte Physik/ Photophysik
Fachrichtung Physik
Fakultät Mathematik und Naturwissenschaften
Technische Universität Dresden

Strain-Mediated Coupling in Magnetoelectric Composite Materials

Diplomarbeit
zur Erlangung des akademischen Grades
Diplom-Physiker

vorgelegt von
Robert Streubel
geboren am 5. Oktober 1987 in Dippoldiswalde

Dresden, Juni 2011

Eingereicht am 14. Juni 2011

1. Gutachter: Prof. Dr. Lukas M. Eng
2. Gutachter: Prof. Dr. Rudolf Groß

Abstract

The present thesis reports on the strain-mediated coupling between the magnetic domain structure of magnetostrictive nickel and the polarization of the ferroelectric barium titanate substrate. A series of samples was prepared for the investigation of the dependence on deposition rate and temperature as well as thickness of the magnetic layer. The symmetry-induced topographical steps in the substrate, observed by Piezoresponse Force Microscopy, cause a correlation between topography and ferroelectric domains. The investigation of the magnetic domain structure is proceeded, using Magneto-Optical Kerr Microscopy and Magnetic Force Microscopy. Both magnitude of anisotropy (15 to 35 $\mathrm{kJ/m^3}$, intrinsic value of $\approx 1\,\mathrm{kJ/m^3}$ excluded) and orientation of the easy axis show remarkable dependence on deposition conditions and underlying ferroelectric domain. An appropriate configuration of the deposition conditions allows locally the rotation of the easy axis by 90°. Both saturation magnetization and integral hysteresis are measured by a Superconducting Quantum Interference Device magnetometer. Additionally, the stress distribution within the magnetostrictive film is modeled using an analytical approach.

Kurzfassung

Im Rahmen der vorliegenden Diplomarbeit wird die spannungsinduzierte Kopplung in magnetoelektrischen Heterostrukturen am Beispiel von magnetostriktivem Nickel, aufgebracht auf ferroelektrischem Bariumtitanateinkristall, diskutiert. Die von veränderten Gitterkonstanten herrührende Spannung wird auf Abhängigkeiten von Depositionrate and Temperature, sowie Filmdicke untersucht. Mithilfe der Piezoresponse-Kraftmikroskopie wird der Zusammenhang zwischen Topographie und ferroelektrischen Domänen bestätigt. Die Untersuchung der magnetischen Eigenschaften wird mittels Magnetkraftmikroskopie und Magnetooptischer Kerr-Mikroskopie durchgeführt. Aufgrund unterschiedlicher Spannungswerte, bedingt durch variierender Depositionsbedingungen und elektrischen Schaltens des Substrates, ergeben sich induzierte Anisotropien im Bereich von 15 bis 35 $\mathrm{kJ/m^3}$, intrinsische Anisotropie von $\approx 1\,\mathrm{kJ/m^3}$ ausgeschlossen. Entsprechend der Depositionbedingungen können lokal magnetische leichte Achsen parallel und senkrecht zu den topographischen Stufen eingestellt werden. Die Sättigungsmagnetisierungen werden mithilfe einer Supraleitenden Quanteninterferenzeinheit (SQUID) bestimmt (255 - 300 $\mathrm{kA/m}$). Der Vergleich mit einkristallinem Nickel ergibt eine relative Volumendichte von 52 bis 62%. Für die Simulation der Spannungsverteilung im Film wird ein analytischer Ansatz aufgegriffen.

Contents

1. Introduction

Among all electric and magnetic materials multiferroic and magnetoelectric materials exhibt certain interesting properties. Whereas magnetoelectric (ME) materials show a coupling between the electric and magnetic properties, multiferroic materials have several states of remanence, e.g. ferroelectric, ferromagnetic or ferroelastic. Materials, which exhibit simultaneously multiferroic and magnetoelectric properties, allow, therefore, the configuration of magnetic equilibrium states with the aid of electric or stress fields, or vice versa.

The pioneering research on magnetoelectric materials can be traced back to the late 1950s [see EMS06], though, a revival of these materials has been noticed. The recent increase of interest is both caused by improved theoretical understanding and advanced experimental preparation. For instance, single-phase magnetoelectric materials require high quality single-crystals, whereas accuracy within nanometer range is necessary for composites. Single-phase ME materials are very limited by the coexistence of both ferroelectric and antiferromagentic properties, though. Contrary, different kind of compositions, such as multilayer core-shell systems, can be prepared to match exactly the desired purpose. Moreover, since the composition is only limited by the magnetostriction of the ferromagnetic phase, allowing a strain-mediated coupling between the ferroelectric and the ferromagnetic phases, a large variety exists.

Among multiple approaches of affecting the stress distribution within magnetostrictive media, bending of the substrate, ion implantation and the use of magnetoelectric materials are common techniques. Whereas bending and stretching of a non-ferroelectric substrate induce continuously varying stress into the film, ion implantation [see MMF+09] causes a permanent change of the lattice constants. The use of magnetoelectric heterostructures combines localization and reversibility of both techniques, allowing both pre-structuring and dynamic switching after deposition.

Within this thesis the strain-mediated coupling in amorphous nickel deposited on barium titanate single-crystal ($Ni/BaTiO_3$) was investigated. Although this system has already been studied macroscopically by [GBO+10], microscopic observations to clarify the coupling are still not published.

Part I.

Fundamentals

2. Theory

This chapter provides a brief introduction into piezo- and ferroelectricity as well as ferromagnetism, required within this thesis. Because of the interest in strain-mediated coupling both stress and electric field dependence of the dielectric substrate are considered. Within the magnetic section the focus is set on the energy contributions, which affect magnetic domains. Additionally, the magneto-optical Kerr effect is treated. Finally, a technique for calculation of the stress distribution in thin films, caused by a change of the lattice constant of the substrate, is presented.

2.1. Dielectric Media

One large group of media are dielectrics, which show usually high electric susceptibility due to localized electric charges. Piezoelectric and ferroelectric materials belong to this group, showing additional properties.

2.1.1. Piezoelectricity

Whereas the stress tensor of non-piezoelectric dielectrics shows a quadratic dependence on external electric fields ($\propto D_j E_i$), piezoelectric media exhibit an additional linear relation [see LL85]. This behavior is commonly described by the piezoelectric tensor γ_{ijk} and the free enthalpy Φ [SL98]:

$$\mathrm{d}\Phi = -S\,\mathrm{d}T + u_{ij}\,\mathrm{d}\sigma_{ij} - \frac{1}{4\pi} D_j\,\mathrm{d}E_j\,, \tag{2.1.1}$$

$$D_j = D_{j0} + \varepsilon_{jk} E_k + 4\pi\gamma_{jkl}\sigma_{kl}\,, \tag{2.1.2}$$

$$u_{ij} = -\left(\frac{\partial\Phi}{\partial\sigma_{ij}}\right)_{T,E} = s_{ijkl}\sigma_{kl} + \gamma_{lij}E_l\,. \tag{2.1.3}$$

Here, u_{ij}, σ_{ij}, s_{ijkl} and ε_{jk} are strain tensor, stress tensor, compliance and dielectric tensor, respectively. Moreover, entropy S, temperature T, electric $\boldsymbol{E}$ and displacement field $\boldsymbol{D}$ are

used. Here, the Einstein convention for summation is applied. (2.1.3) describes the strain of the continuous material due to the attraction between fixed charges and an external electric field, and an external stress field. Hence, the piezoelectric tensor represents the expansion constant of both the displacement with respect to the stress field, and of the strain tensor with respect to the electric field. Due to the symmetry of σ_{ij} in equilibrium state, both compliance and piezoelectric tensor can be expressed using the Voigt notation as s_{kl} and d_{jk}. Whereas k and l are numbers from 1 to 6, j remains unchanged, identical to full tensor notation. Further simplification is achieved by considering the symmetry of the unit cell, e.g. tetragonality:

$$d_{jk} = \begin{pmatrix} 0 & 0 & 0 & 0 & d_{15} & 0 \\ 0 & 0 & 0 & d_{15} & 0 & 0 \\ d_{31} & d_{31} & d_{33} & 0 & 0 & 0 \end{pmatrix} . \tag{2.1.4}$$

2.1.2. Ferroelectricity

Ferroelectrics are materials that exhibit equilibrium states, which are transferrable into each other by applying an electric field. The non-centrosymmetric, polarized unit cell originates from a hybridization of d^0 and p orbitals [Spa07]. In case of perovskites, which have a unit cell of ABO_3 structure, the B-atom is oxidized to B^{4+}, leading to a closed-shell ion. These media can be described within the framework of the phenomenological Landau theory [see LL91] by the the free enthalpy Φ. Since this theory is based on symmetry, external fields, such as electric and stress fields, can be considered easily. The corresponding Φ reads for materials with tetragonal symmetry, such as barium titanate at room temperature, exposed to a stress field [see SL98]:

$$\begin{aligned} \Phi = \Phi_0 &+ \frac{1}{2}\alpha(T - T_c)(\eta_1^2 + \eta_2^2) + \frac{1}{4}\beta_1(\eta_1^2 + \eta_2^2)^2 + \frac{1}{2}\beta_2\eta_1^2\eta_2^2 - \\ &- g(\sigma_{11} + \sigma_{22}) - r_1(\eta_1^2 + \eta_2^2)(\sigma_{11} + \sigma_{22}) - r_2(\eta_1\sigma_{22} + \eta_2\sigma_{11}) - \\ &- r_3\eta_1\eta_2\sigma_{12} - \frac{1}{2}s_1(\sigma_{11}^2 + \sigma_{22}) - \frac{1}{2}s_2\sigma_{12}^2 - s_3\sigma_{11}\sigma_{22} \,, \end{aligned} \tag{2.1.5}$$

where r_i, s_i and g are constants, describing the elastic properties. α and β_i are coefficients, determined by the non-distributed free enthalpy Φ_0. However, in the absence of any external stress fields but exposed to an electric field, the free enthalpy becomes simply $\Phi(T, \eta, \boldsymbol{E}) = \Phi(T, \eta) - \boldsymbol{EP}$ with the polarization $\boldsymbol{P}$. Because ferroelectric media are also piezoelectric, the contribution (2.1.1) has to be added to obtain the complete Φ.

2.1.3. Tetragonal Ferroelectrics

Ferroelectric perovskites, consisting of ABO_3 unit cells, exhibit different symmetries according to the atom radii. For the investigation of strain-mediated coupling, specimens of the tetragonal group, such as barium titanate (BTO) [Spa07], are very suited. In principle, there are two different types of ferroelectric domains possible. Domains with a polarization normal to the surface are called c-domains, which exhibit either negative (c^-) or positive (c^+) electric surface charges. In-plane polarized domains are named a-domains. In finite samples the equilibrium state is a multidomain state with ferroelectric domain walls. Due to the mismatch of the lattice constants of a and c-domains [see Fig. 2.1(a)], a slight distortion of the unit cell in the vicinity of the domain wall occurs (b). The experimentally determined angle of 0.6 degrees leads macroscopically to straight topographical steps (c). The feature of homogeneity along the steps represents one advantage of tetragonal ferroelectrics over other substrates, used for magnetoelectric composites. Other symmetry groups either do not show a change of lattice constants, e.g. rhombohedral, or exhibit several possible lattice constants. Moreover, the orientation of the crystal axes and, hence, the changed lattice constant varies for polycrystals. Thus, the mentioned homogeneity is absent.

The a-domains with a polarization perpendicular to the topographical steps are called a_1. Although rather unusual, a_2-domains exhibit polarization vectors parallel to the steps.

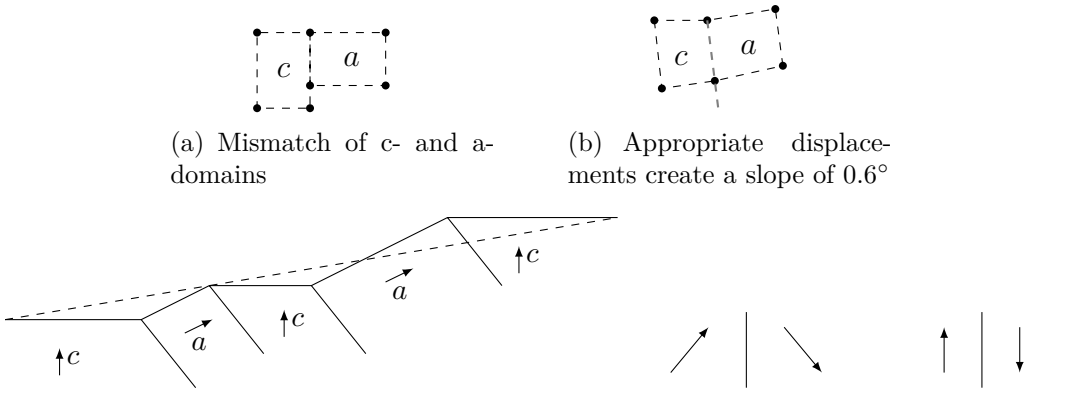

(a) Mismatch of c- and a-domains

(b) Appropriate displacements create a slope of 0.6°

(c) Typical topographical steps of BTO

(d) 90° wall

(e) 180° wall

Fig. 2.1.: *Correlation between the topography and the ferroelectric domain configuration of BTO. (a) and (b): qualitative microscopic explanation of the slope creation, (c): cross-section of barium titanate. The arrows represent the polarization of the ferroelectric domains, here only c^+ and a^+ domains. The dashed line corresponds to the sample surface. Due to the minimization of the field energy, 180° and 90° walls with head-to-tail configuration are formed leading to multi-domain structures. The slope has a value of 0.6° for BTO. Hence, they are 90.6° and 89.4° rather than 90° walls.*

According to the slope of the steps, a^+ and a^- can be declared as well.

2.2. Ferromagnetic Media

Ferromagnets are electron systems with a non-vanishing momentum and several equivalent equilibrium states with respect to the spin alignment. Contrary to dielectrics, ferromagnets are conductors, exhibiting non-localized electrons. Within this section, a brief overview on the important energy contributions within any magnetic medium, following [HS09], is given. The actual state of equilibrium is influenced by the ratio between these energies and their history, leading to a hysteresis.

2.2.1. Exchange Energy

Ferromagnets are electron systems with strong coupling between adjacent electron spins. In the lowest order the coupling can be expressed using the Heisenberg correlation [HS09]:

$$\mathcal{H} = -\sum_{(ij)} J_{ij} \boldsymbol{S}_i \boldsymbol{S}_j \tag{2.2.1}$$

with the exchange tensor J_{ij}, the spin operators $\boldsymbol{S}_i$ at the i-th lattice point and a summation over nearest neighbors. Hence, ferromagnets exhibit positive exchange values J with a favored uniform orientation, whereas antiferromagnets have negative J. (2.2.1) can be easily extended to sublattice systems. Since we are dealing with single-atom unit cells, it is omitted here. The given formula can be transferred into (see A.1):

$$\mathcal{H} = \frac{J}{2a} \int (\nabla \boldsymbol{S})^2 \, \mathrm{d}^3 r = \frac{J}{2a} \int \left\{ (\nabla S_x)^2 + (\nabla S_y)^2 + (\nabla S_z)^2 \right\} \mathrm{d}^3 r \,, \tag{2.2.2}$$

assuming a constant exchange tensor and lattice constant a and neglecting an offset, originating from the expansion of the scalar product. Since (2.2.2) is used within this thesis, the exchange constant is redefined as $A = \frac{J}{2a}$. This value for crystalline nickel is, for instance, $A = 4.6 \cdot 10^{-12}\,\mathrm{J/m}$ [Lee55].

2.2.2. Field Energies

There are two different kinds of field energies related to magnetic samples. The first one originates from the stray field generated by the sample itself. The second is caused by the interaction with an external magnetic field (Zeeman), which will be treated at the end of this paragraph.

According to the Maxwell equation $\nabla \boldsymbol{B} = \mu_0 \nabla(\boldsymbol{H} + \boldsymbol{M}) = 0$ for the magnetic induction $\boldsymbol{B}$, each source and sink of the magnetization $\boldsymbol{M}$ cause a stray field $\boldsymbol{H}$:

$$\left.\begin{aligned} \rho &= -\nabla \boldsymbol{M}\,, \\ \sigma &= \boldsymbol{M}\boldsymbol{n}\,, \\ \phi &= \frac{1}{4\pi}\left[\int \frac{\rho(\boldsymbol{r}')}{|\boldsymbol{r}-\boldsymbol{r}'|}\,\mathrm{d}V' + \oint \frac{\sigma(\boldsymbol{r}')}{|\boldsymbol{r}-\boldsymbol{r}'|}\,\mathrm{d}S'\right]. \end{aligned}\right\} \tag{2.2.3}$$

Here, ρ and σ are volume divergence and surface charge with the surface normal $\boldsymbol{n}$. The calculation of the magnetostatic potential ϕ is in total analogy to the electrostatics with an integration over the whole sample. Using both the definition of the field energy [HS09]:

$$E = -\frac{\mu_0}{2} \int\limits_{sample} \boldsymbol{H}\boldsymbol{M}\,\mathrm{d}V \tag{2.2.4}$$

and $\boldsymbol{H} = -\nabla\phi$, we obtain:

$$E = \frac{\mu_0}{2}\left(\int \rho\phi\,\mathrm{d}V + \oint \sigma\phi\,\mathrm{d}S\right), \tag{2.2.5}$$

which is the effective energy contribution due to the stray field. Notice the quadratic dependence on the magnetization. Because the stray field is strongly affected by the geometry of the sample it is both important and difficult to be determined. For instance, only infinitely extended plates as well as ellipsoids can be calculated analytically. The calculation leads to the demagnetization factors N, or rather general N_{ij}. For an infinitely extended, homogeneous plate lying within the xy-plane one obtains:

$$\left.\begin{aligned} \boldsymbol{H} &= -\boldsymbol{M}_s \\ e &= \frac{\mu_0}{2} N M_s^2 = N K_d \end{aligned}\right\} \tag{2.2.6}$$

with the energy density e, $N = 1$ and the stray field constant K_d ($\approx 10^6\,\mathrm{J/m^3}$) [HS09].

External magnetic fields can be considered by substitution of ϕ in (2.2.5) by $2\phi_{ext}$, if there are sources and sinks such as magnetic tips. Otherwise it can be calculated by $E = -\mu_0 \int \boldsymbol{H}\boldsymbol{M}\,\mathrm{d}V$.

2.2.3. Anisotropy Energy

For an arrangement of atoms, such as crystals and glasses, the spin-orbit coupling between adjacent atoms leads to a favored direction of magnetization due to an overlap or distortion

of the electron orbitals. These directions are called either easy axis or easy plane with respect to the sign of anisotropy. As the angle between the actual direction and the easy axis increases, the anisotropy energy increases as well. Mathematically this is treated as a perturbation of spherical harmonics up to the second order [LL85]. Exploiting the symmetry of cubic unit cells the corresponding crystalline anisotropy is:

$$K = K_1(m_1^2 m_2^2 + m_2^2 m_3^2 + m_1^2 m_3^2) + K_2 m_1^2 m_2^2 m_3^2 \,. \tag{2.2.7}$$

Here, K_1 and K_2 are the first and second anisotropy constants, and m_j represent the sine of the angle between the magnetization vector $\boldsymbol{M}$ and the equivalent three crystal axes. According to the ratio between the anisotropy constants, three different directions of the easy axis are possible: <100>, <110> and <111>. Crystalline Ni shows the latter orientation to be preferred, corresponding to a negative first anisotropy constant. Usually deviations from that isotropic case occur due to any ex- or internal fields, which are considered by an additional uniaxial contribution:

$$K = K_{u1} \sin^2 \theta + K_{u2} \sin^4 \theta \,, \tag{2.2.8}$$

with the angle θ between $\boldsymbol{M}$ and the easy axis and K_{u1} and K_{u2} as first and second anisotropy constant of uniaxial symmetry, which are usually much higher than K_1 and K_2 ($K_1 \approx 10^4\,\mathrm{J/m^3}$, $K_{u1} \approx 10^7\,\mathrm{J/m^3}$ [HS09]).

Polycrystalline or even amorphous media show macroscopically a reduced and rather isotropic anisotropy constant, due to locally varying crystallographic directions. The corresponding anisotropy K constant is of the range of $K \approx 10^2\,\mathrm{J/m^3}$.

Magnetostrictive media, such as Fe, Co, Ni, exhibit stress-sensitive magnetic properties, whose origin is explained by Van Vleck in [VV53]. Accordingly, the ground states are mixed multiplets of d-orbitals. In cubic/ isotropic crystals the momenta are largely quenched, which suppresses the hybridization. If the environment is slightly distorted due to ex- or internal stress, the electric potential changes, leading to a deformation of the electron orbitals, the mentioned hybridization and a change of the direction of the easy axis. Because the resulting symmetry is uniaxial, magnetostriction can be considered by an uniaxial anisotropy up to the first order with [Lee55]:

$$K_{u1} = -3/2 \lambda \sigma \,. \tag{2.2.9}$$

Here, λ is the average magnetostriction constant ($\lambda_{Ni} \simeq 3.4 \cdot 10^{-5}$ for polycrystalline nickel [Lee55]) and σ the stress along the easy axis. Within glasses the magnetostrictive energy

can considerably contribute to the direction and magnitude of anisotropy due to their amorphous morphology.

2.2.4. Magnetization Curves

Considering application to magnetic hystereses, commonly used to determine the magnetic properties, these energy contributions need to be summed up. Assuming an uniform magnetization in the test volume throughout the whole loop, the exchange energy does not contribute. This is actually only valid for small sizes, since the stray field is usually reduced by multidomain rotation. In the following, we will focus on in-plane and normal hystereses, required within this thesis. Hence, easy axis, magnetization vector and external field lie within on plane, allowing a single-parameter description. The energy density of a uniaxial system, described by an overall anisotropy constant K, becomes for normal hysteresis:

$$E = K \sin^2\theta + \frac{1}{2}\mu_0 N M_s^2 \sin^2\theta - \mu_0 M_s H \cos(\theta - \theta_0) \tag{2.2.10}$$

and for in-plane hysteresis:

$$E = K \sin^2\theta - \mu_0 M_s H \cos(\theta - \theta_0)\,. \tag{2.2.11}$$

θ and θ_0 are tilting angle of the magnetization with respect to the easy axis and the angle between magnetic field and easy axis, respectively. Since in-plane fields do not cause any normal magnetization components, the stray field contribution vanishes. Fig. 2.2 shows the angle dependence of (2.2.11) for the case of hard axis switching ($\theta_0 = \pi$) as a function of the normalized magnetic field $h = M_s H/2K$. The minimization of the energy (2.2.11) with respect to θ leads to a continuous transition, which is described by:

$$M = 2\frac{K}{B}\sin\theta\,. \tag{2.2.12}$$

Consequently, the magnetization vectors will align accordingly. Detecting the magnetization components parallel to the magnetic field during the hysteresis will, therefore, lead to the same dependence. Thus, the anisotropy can be calculated. The system is saturated, when $h = 1/\mu_0$ (red line).

2.2.5. Domain Walls

Within extended magnetic systems the equilibrium state is represented by a multidomain state due to the lower stray field energy. The transition areas are called domain walls. The

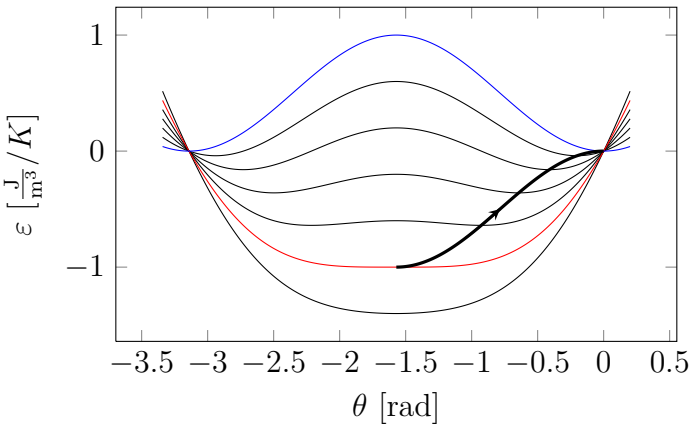

Fig. 2.2.: *Influence of an external magnetic field, perpendicular to the magnetic easy axis, on the equilibrium energy density ε shown as function of the magnitude h and the tilting angle $\theta = \measuredangle(\boldsymbol{M}, easy\,axis)$. Red and blue curves display the energy without and within the switching field, respectively. Each black curve shows the energy with a shift of $0.2h$, illustrating, therefore, the shape of the magnetic hysteresis. The magnetization curve is plotted thick.*

properties, such as width and magnetization rotation, depend on the wall energy, consisting of exchange, anisotropy and stray field energy. To be accurate, the elastic energy has to be considered as well. Due to the thickness of films magnetic domain walls can be assumed to depend only on one parameter [HS09]. The stray field is neglected in thin films, since it would favor two-dimensional* walls, which are suppressed in sufficiently thin films [Hub70]. Writing (2.2.2) in spherical coordinates the wall energy density is:

$$\gamma_w = \int_{-\infty}^{\infty} \left[A(\varphi'^2 \sin\vartheta + \vartheta') + K\cos^2\varphi\right] \mathrm{d}x\,. \tag{2.2.13}$$

In our case we assumed ϑ to be constant, and even zero. With the aid of the Euler-Lagrange formalism and the boundary conditions $\varphi(\pm\infty) = 0$ one obtains:

$$\gamma_w = 4\sqrt{AK}\,, \tag{2.2.14}$$

$$\sin\varphi = \tanh\frac{x}{\sqrt{A/K}}\,, \tag{2.2.15}$$

$$\cos\varphi = \left(\cosh\frac{x}{\sqrt{A/K}}\right)^{-1}\,. \tag{2.2.16}$$

*The differentiation between one- and two-dimensional walls refers to the number of variables, required to describe the transition properly.

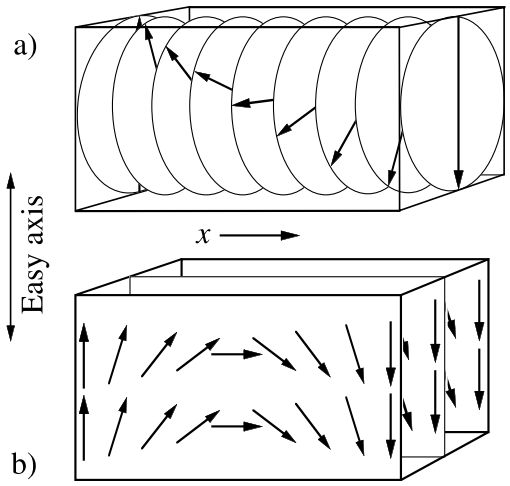

Fig. 2.3.: *Illustration of the magnetization rotation within one-dimensional 180° Bloch (a) and Néel (b) wall. The wall normal is parallel to x. (from [HS09])*

The calculated energy belongs to symmetric Bloch walls (see Fig. 2.3), whose magnetization components can be described by (2.2.16) and (2.2.15). Consequently, the rotation axis is normal to the domain wall, causing magnetic surface charges. Within very thin films another type, namely Néel walls, appears, exhibiting a rotation axis normal to the surface. The surface charges are avoided by inducing volume divergences, which may cause a lower energy contribution.

The restriction to one-dimensional domain walls will be released at a certain thickness, depending on the three energy contributions, already mentioned [HS09]. Derivatives, such as asymmetric Bloch or Néel walls, show a superimposition of both one-dimensional walls.

2.3. Magnetoelectric Materials

Among all different kinds of electron systems magnetoelectric materials show a noticeable coupling between electric and magnetic phases. The free enthalpy of a directly coupled single-phase ME is [EMS06]:

$$\Phi = -\frac{1}{2}\left(\varepsilon_0\varepsilon_{ij}E_iE_j + \mu_0\mu_{ij}H_iH_j + \alpha_{ij}E_iH_j + \beta_{ijk}E_iH_jH_k + \gamma_{ijk}H_iE_jE_k\right) . \qquad (2.3.1)$$

The first two terms on the right side represent the uncoupled field energy, whereas the remaining belong to the linear and second-order ME coupling with its constants α_{ij}, β_{ijk} and γ_{ijk}. Both polarization and magnetization as a function of magnetic and electric field, respectively, can be obtained by derivation with respect to $\boldsymbol{E}$ and $\boldsymbol{H}$. Materials with

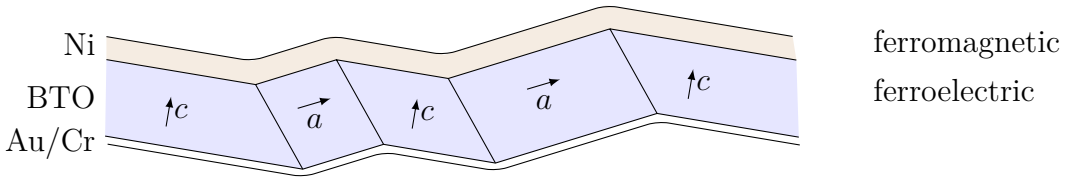

Fig. 2.4.: *Nickel deposited on ferroelectric barium titanate as an example for the magnetoelectric composite material, treated within this thesis.*

both high ε_{ij} and μ_{ij} should, therefore, display large ME coupling since $\alpha_{ij}^2 \leq \varepsilon_0\mu_0\varepsilon_{ij}\mu_{ij}$ [see EMS06]. Since ferroelectricity requires according to [Spa07] d^0 electrons, which do not show magnetic properties except diamagnetism, the unit cell of the single-phase ME has to consist of more than two atoms. Additionally, single-phase ME are due to non-conductivity restricted to antiferromagnets, such as bismuth ferrite, showing poor permeability.

Therefore, composite materials may be more suited for applications, which require large saturation magnetization. Since the coupling is mediated by elastic properties, magnetostrictive ferromagnets, e.g. Fe, Co, Ni, FeCo, are required. Beside a larger variety different kind of compositions, such as multilayer and core-shell systems, can be prepared to match exactly their purpose. For instance, Fig. 2.4 shows a two-component composite consisting of a nickel film deposited on top of barium titanate single-crystal. Since the atoms attach rather stress-free during deposition, stress and anisotropy are induced after changing the ferroelectric domain configuration by applying electric or stress fields.

2.4. Theory of Elasticity

Within this thesis the stress distribution in the magnetostrictive thin film is modeled with the aid of the coherency technique, used for calculating the stress distribution in epitaxially grown thin films [see ALK+04]. In the following a brief overview on elasticity and dislocation theory is given, concluding with the coherency technique itself.

2.4.1. General Remarks

Since the responsible molecular forces are short-ranged within the framework of linear continuum mechanics [see LL91], they can be considered to appear between adjacent atoms only. Consequently, the forces $\boldsymbol{f}$ can be considered by introducing the stress tensor σ_{ij}, defined by:

$$\frac{\partial \sigma_{jk}}{\partial x_k} = -f_j \,. \tag{2.4.1}$$

For isotropic media the relation between stress and strain tensor can be expressed by Young's modulus Y and Poisson ratio ν as: $\sigma_{ij} = \frac{Y}{1+\nu}(u_{ij} + \frac{\nu}{1-2\nu}u_{ll}\delta_{ij})$ and $u_{ij} = \frac{1}{Y}((1+\nu)\sigma_{ij} - \nu\sigma_{ll}\delta_{ij})$ [LL91]. Using the first relation and the definition of the strain tensor, (2.4.1) can be rewritten as a function of the displacement $\boldsymbol{u}$:

$$\Delta\boldsymbol{u} + \frac{1}{1-2\nu}\nabla\nabla\boldsymbol{u} = -\boldsymbol{f}\mu\,. \tag{2.4.2}$$

Here, μ represents the shear modulus, defined by $\frac{Y}{2(1+\nu)}$. Since the coupling is mediated by surfaces, $\boldsymbol{f}$ vanishes [LL91]. In general, this equation needs to be solved with the aid of the Green function. However, in case of plane strain within the xy-plane merely u_{xx}, u_{xy}, u_{yy} will be non-zero, allowing analytical solutions. As shown in [LL91] a function χ, obeying $\Delta\Delta\chi = 0$, can be determined, whose second derivatives with respect to x and y represent the stress fields as follows:

$$\sigma_{xx} = \partial_y^2\chi\,, \qquad \sigma_{xy} = -\partial_x\partial_y\chi\,, \qquad \sigma_{yy} = \partial_x^2\chi\,, \qquad \sigma_{zz} = \nu(\sigma_{xx} + \sigma_{yy})\,. \tag{2.4.3}$$

2.4.2. Dislocations

The occurrence of dislocations, described by the Burgers vector $\boldsymbol{b}$ and the dislocation line $\boldsymbol{\tau}$, causes due to additional planes of atoms internal stress fields. The Burgers vector is defined by the increase of the displacement $\boldsymbol{u}$ over a loop around such a singularity (dislocation line):

$$-b_j = \int \mathrm{d}u_j = \oint \frac{\partial u_j}{\partial x_k}\,\mathrm{d}x_k\,. \tag{2.4.4}$$

As shown in [HL82], the potential $\phi = \Delta\chi$ can be expressed as a sum of products of radial and azimuthal terms:

$$\phi = \alpha_0 + \beta_0 \ln r + \sum_{n=1}^{\infty}(\alpha_n r^n + \beta_n r^{-n})\sin n\theta + \sum_{n=1}^{\infty}(\gamma_n r^n + \delta_n r^{-n})\cos n\theta\,. \tag{2.4.5}$$

For an edge dislocation ($\boldsymbol{\tau} \parallel z$, $\boldsymbol{b} \parallel x$) one obtains in the lowest order with the boundary conditions $\phi \xrightarrow{r\to\infty} 0$ and minimum at $\theta = \frac{\pi}{2}$:

$$\phi = \beta_1 r^{-n}\sin\theta\,, \tag{2.4.6}$$

$$\chi = \frac{\beta_1}{2} r \ln r \sin\theta\,, \tag{2.4.7}$$

with $\beta_1 = -\frac{\mu b}{(1-\nu)\pi}$, obtained by taking both (2.4.3) and (2.4.4) into account. The resulting

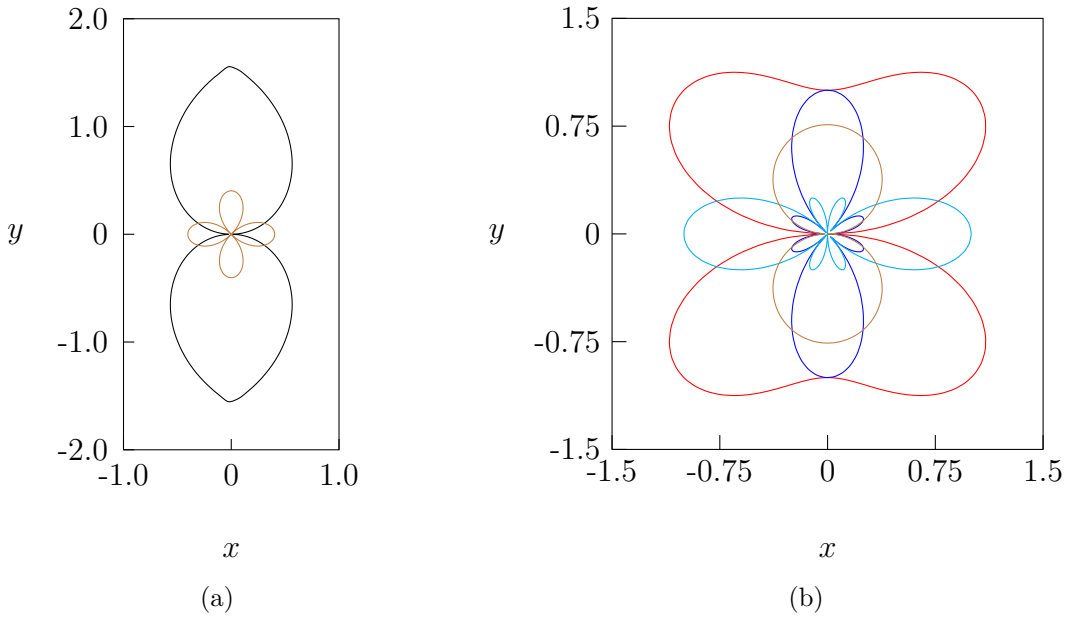

Fig. 2.5.: *Calculation of displacement (a) (u_x: — , u_y: —) and stress field components (b) (σ_{xx}: — , σ_{yy}: — , σ_{xy}: — , σ_{zz}: —) for an infinitely extended xy-plane with plane strain conditions for an edge dislocation ($\boldsymbol{\tau} \parallel z$, $\boldsymbol{b} \parallel x$). The units are $b/2\pi$ and $\mu b/2\pi(1-\nu)$ for left and right graph, respectively.*

stress fields for an infinitely extended xy-plane are accordingly (see Fig. 2.5):

$$\left.\begin{aligned} \sigma_{xx} &= -Dby\frac{3x^2+y^2}{(x^2+y^2)^2}\,, & \sigma_{yy} &= Dby\frac{x^2-y^2}{(x^2+y^2)^2} \\ \sigma_{xy} &= Dbx\frac{x^2+y^2}{(x^2+y^2)^2}\,, & \sigma_{zz} &= \nu(\sigma_{xx}+\sigma_{yy}) \end{aligned}\right\} \tag{2.4.8}$$

with $D = \mu/2\pi(1-\nu)$.

In case of finite expansion, every stress field component and its derivatives with an index similar to the surface normals, e.g. x, has to vanish. A commonly used approach are image charges, here image dislocations, located outside the medium with the same distance l and opposite charge. Since the off-diagonal component σ_{xy} is odd in x, a further term, considering the boundary conditions, is added to χ [see HL82]:

$$\chi = 2Dbl\frac{xy}{((x-l)^2+y^2)^2}\,. \tag{2.4.9}$$

Thus, the stress field consists of the contribution given by (2.4.3), the corresponding image field and the term derived from (2.4.9).

2.4.3. Coherency Technique

As mentioned at the beginning of this section, the coherency technique is used for calculating the stress distribution within epitaxially grown thin films. Within this thesis this approach is adapted to amorphous thin films with locally varying stress due to different change of lattice constants. Therefore, in the following an introduction is given.

The basic idea is the exploitation of analytically known stress field distributions of dislocations to calculate the stress caused by non-uniform elastic distortions, such as stretch, tilting, shearing, within thin films. For this purpose different kinds of dislocations with varying orientation and magnitude of the Burgers vector are appropriately distributed (see Fig. 2.6). Here, it is both convenient and sufficient to introduce only edge dislocations with constant Burgers vector within each ferroelectric domain. The change of lattice constant is considered by Burgers vectors parallel to the surface normal, as indicated in (a), whereas the tilt of the tetragonal unit cell is included by Burgers vectors normal to the substrate [see (b)]. It is worth to mention, that both additional plane within the film and absent plane within the substrate result in the same stress field. Since the domain is transversely extended with a length l, the previously presented stress fields need to be summarized over the entire range [FBPR07]:

$$\sigma_{ij}^{(d)} = \sum_{n=0}^{\infty} \sigma_{ij}(x, y - nh) = \frac{\varepsilon}{b} \int_0^l \sigma_{ij}(x, y - y')\,\mathrm{d}y' \,. \tag{2.4.10}$$

Here, ε represents the relative change of the lattice constant (or the misfit parameter). For this formula $l\varepsilon = Nb$ for $N \to \infty$ has to be fulfilled.

The actual stress fields caused by a change of lattice constant, which are given in A.2, can either be obtained by following the steps shown in this section or by taking them from

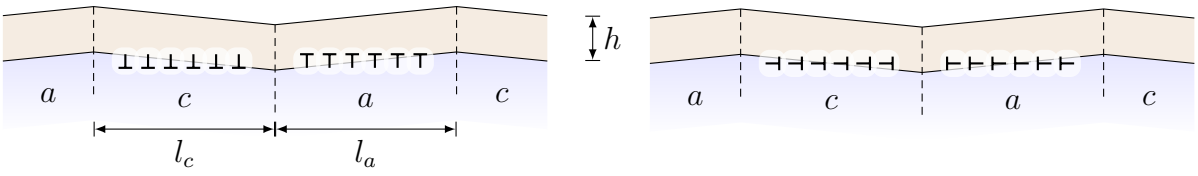

(a) (b)

Fig. 2.6.: *Since elastic distortions can be modeled by plastic dislocations, (a) and (b) show the appropriate distribution of edge dislocations for different lattice constants and topographical steps, respectively. The film is supposed to be deposited on cubic FE. The* ⊤*'s represent the dislocation line with its Burgers vector. Accordingly,* ⊤ *and* ⊥ *display an additional and a missing plane normal to the surface, respectively. Within the limit of linear elasticity the corresponding stress fields are calculated separately.*

[ALK+04] and [FBPR07]. Besides the advantage of analytical formulation, this approach does not depend directly on any morphology but on the elastic coefficients, which depend on the morphology. Therefore, it can be in general used for any kind of morphology, as long as the elastic coefficients of substrate and film do not differ too much.

3. Measurement Techniques

To gain a thorough understanding of the magnetoelectric systems different kinds of measurement technique have been applied within this thesis. In this chapter, the relevant aspects will be given, necessary for an appropriate interpretation and analysis. The focus lies on the origin of contrast for imaging techniques.

3.1. Atomic Force Microscopy (AFM)

Nano- and microscale investigations are usually carried out with the aid of Atomic Force Microscopy and its derivates, such as Piezoresponse Force Microscopy and Magnetic Force Microscopy. The sample is scanned using at least three piezoactors for the three coordinate axes in intermitted, contact or non-contact mode. For instance, PFM and MFM work in contact and non-contact mode, respectively. To increase the range and the precision additional actors can be stacked. If the topography changes, the deflection of the beam, focused on the cantilever and adjusted at the center of the 4-quadrant photodiode, is affected, leading to a change of the top-minus-bottom (tb) or left-minus-right (lr) signal. Supposing the orientation of the photodiode with respect to the tip is appropriate, the tb controls the voltage over the z-piezo adjusting the pressure for contact and distance for non-contact mode. According to the topography and type of sample the control parameters can be modified to proceed effectively.

3.1.1. Piezoresponse Force Microscopy (PFM)

For the last 20 years, PFM has proven to be one of the most appropriate methods to inspect ferroelectric domain structures. Since this technique exploits the piezoelectric effect (see Fig. 3.1), it can be used for any polarizable and polarized media. During the scan an AC-voltage V_0 is applied to the conductive tip, leading to an oscillating electric field. Although off-resonance results in a lower signal, quantitative calculations, such as orientation/ miscut, can be done. If such analysis is not intended, the frequency can be set to a resonant frequency, gaining a higher signal. The PFM spectrum of a barium titanate

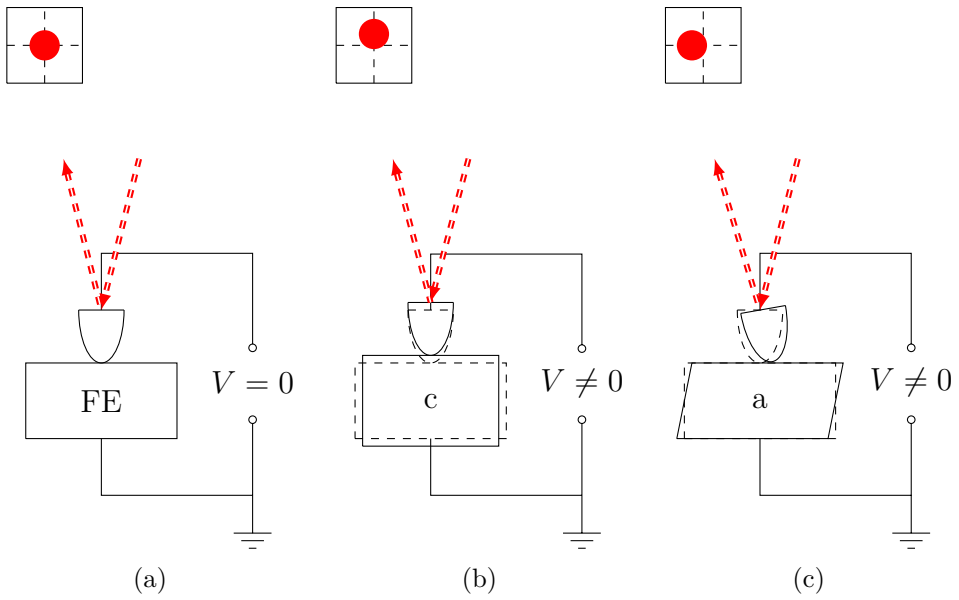

Fig. 3.1.: *Principles of PFM. The piezo- or ferroelectric sample is scanned by a conductive tip, deflecting a collimated beam with respect to the topography. The beam enters the 4-quadrant photodiode centered, allowing top-minus-bottom (tb) and left-minus-right (lr) signals to regulate the circuit. Increasing height causes an increased tb signal (b), whereas additional torsion of the tip leads to a non-zero lr (c). To distinguish between actual topography and piezoelectric signals an electric AC voltage is applied to the sample, resulting in dynamic compression or expansion and tilting. Using the excitation voltage as reference, amplitude and phase can be extracted.*

single-crystal is shown in Fig. 3.2. Since the elongation of the cantilever is measured, the graph shows the spectrum of the correlated system sample-cantilever. Therefore, higher eigenmodes of the cantilever will also appear, which do not originate from the piezoelectric effect.

The response of the piezoelectric sample can be derived in first order from (2.1.3). For tetragonal systems one obtains for out-of-plane:

$$\Delta z_r \approx -d_{33}\, V_0 \cos(\omega t + \varphi)\,, \tag{3.1.1}$$

and for in-plane polarization:

$$\Delta x_r \approx d_{15}\, V_0 \cos(\omega t + \varphi)\,. \tag{3.1.2}$$

Here, z is the axis perpendicular to the surface and the direction of the applied electric field, whereas x is perpendicular to the tip. Although the electric field exhibits x and

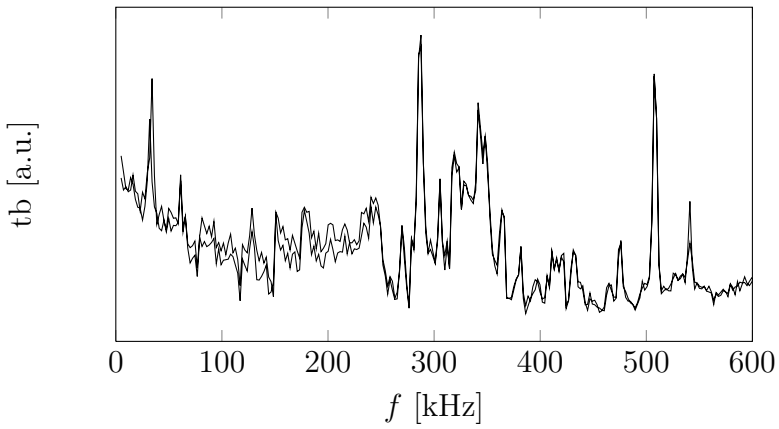

Fig. 3.2.: *The graph shows the PFM spectrum of barium titanate illustrating the different resonant peaks for d_{15}, d_{33} and higher eigenmodes of the cantilever. Since the contribution of d_{15} is mediated by buckling, the resonant peaks are less pronounced. For resonant measurement 285.39 kHz and 34.16 kHz for in-plane and out-of-plane signal, respectively, were used.*

y-components, too, their contribution is low for flat tips. Thus, both formulae describe the change of lattice constant along the polarization axis due to expansion and shearing of the unit cell with respect to external field and orientation. Assuming perfect stiction between tip and sample, the tip will follow the change of the surface, resulting in bending and twisting, and a change of tb and lr signal proportional to (3.1.1) and (3.1.2), respectively. The phase φ depends on the direction of the polarization with respect to the applied electric field according to $\Phi \propto -\boldsymbol{EP}$. Hence, it is zero, if the polarization is either parallel (c^-) to the field or absent. Antiparallel (c^+) alignment leads to a phase shift of π. If the AC-voltage is applied to the bottom, while setting the tip to mass, the phase shift will be reversed. However, as shown in Fig. 3.3, parasite capacitance and inductance cause a phase shift, which do not belong to the piezoelectric effect [Jun06]. The magnitude of the PFM signal is related to the piezoelectric coefficients d_{ij}, which do not depend on the direction.

3.1.2. Magnetic Force Microscopy (MFM)

In contrast to all other AFM methods, a magnetic tip is used in MFM. Usually, the magnetization os achieved by a coating with a ferromagnetic metal, such as Co. In general, the magnetic tip is bent and twisted due to many different kinds of interaction, originating from topography, electric- or magnetic charges. The extraction of electric- magnetic contribution from the rather strong topography signal is obtained by two-pass scan. As long as the control parameters are appropriately chosen and the distance between substrate

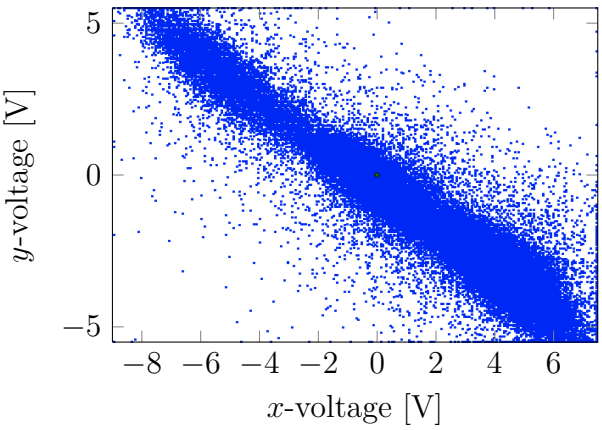

Fig. 3.3.: *PFM: 2D-histogramm of lock-in output, showing phase shift. In ideal case, the y-voltage should vanish.*

and tip is kept constant during each line scan, the topography does not contribute at all. However, since the topography is scanned in intermitted mode, the interaction between sample and tip is quite high, causing a switch of magnetic domains for out-of-plane or displacement of domain walls for in-plane easy axis materials. Thus, the tip magnetization has to be chosen properly, to guarantee low affection and to get strong signal. In our case the magnetostatic interaction was minimized by switching from standard MFM tips (saturation magnetization: 300 kA/m; tip radius: 50 nm) to sharp, low-magnetized MFM tips, exhibiting a saturation magnetization of less than 80 kA/m and a tip radius of < 15 nm. With the aid of a permanent magnet the magnetization of each tip was aligned vertically with respect to the sample, exhibiting south pol near the very tip.

3.1.2.1. Mathematical Treatment

The non-contact, dynamic AFM mode is treated mathematically as an one-dimensional, damped, excited harmonic oscillator (3.1.3) with the eigenfrequency ω_0, the damping factor γ and the external forces $\boldsymbol{F}(z, \dot{z})$ and $f(\omega)$ [Har99]. For simplicity the forces are supposed to be aligned normal to the surface. The latter force is usually caused by an artificial oscillation of the cantilever near its eigenfrequency ($\approx 5\%$ offset) to avoid contrast inversion. The cantilever oscillates normal to the surface at a sample-tip distance z_0. This is valid for rather large distances and flat samples due to the absence of parallel stray field components. Furthermore, ω is the applied angular frequency and m the mass of the tip.

$$\ddot{z} + 2\gamma\dot{z} + \omega_0^2(z - z_0) = \delta_0 \cos\omega t + \frac{1}{m}F(z, \dot{z}) \tag{3.1.3}$$

Neglecting the spatial force $\boldsymbol{F}(z, \dot{z})$, one obtains:

$$z = z_0 + \delta \cos(\omega t + \alpha)\,, \tag{3.1.4}$$

$$\delta = \frac{\delta_0}{\sqrt{(\omega - \omega_0)^2 + (2\gamma\omega)^2}}\,, \tag{3.1.5}$$

$$\alpha = \arctan \frac{2\gamma\omega}{\omega^2 - \omega_0^2}\,. \tag{3.1.6}$$

In general, (3.1.3) is not solvable analytically. Provided $z \gg z_0$ and a Taylor expandable force $F(z, \dot{z})$, F can be considered up to the first order by

$$\omega_0 \to \omega_0 \sqrt{1 - \frac{1}{c}\partial_z F(z_0)}\,, \tag{3.1.7}$$

where c is the spring constant. Due to the spatial force, representing long-range electromagnetic forces, particularly caused by the stray field of the magnetization of the sample, the resonance frequency is shifted locally with respect to the normal derivative. According to (3.1.6) and (3.1.7), attractive forces cause always a positive shift of the eigenfrequency in spite of positive or negative phase offset. However, if the attraction or repulsion is too strong an inversion of contrast occurs. This could be of interest, when measuring domain walls at a small sample-tip distance. Additionally, with respect to the sign of the frequency offset, the AFM will be more sensitive to either repulsive or attractive forces.

3.1.2.2. Physical Origin

To understand the MFM-images, it is necessary to know the origin of F. Since F is the negative gradient of the magnetic energy E, which is defined as the volume integral over the product of the induction $\boldsymbol{B}$ and the stray field $\boldsymbol{H}$, one needs to calculate E first. Considering non-overlapping stray field and magnetization $\boldsymbol{M}$, two equivalent integrals are obtained:

$$E = -\mu_0 \int\limits_{sample} \boldsymbol{H}_t \boldsymbol{M}_s \,\mathrm{d}V = -\mu_0 \int\limits_{tip} \boldsymbol{H}_s \boldsymbol{M}_t \,\mathrm{d}V\,, \tag{3.1.8}$$

where the indices s and t correspond to sample and tip. This equation can be analyzed further, as was shown in 2.2.2, leading to:

$$E = \mu_0 \int\limits_{sample} \rho_s \phi \,\mathrm{d}V + \mu_0 \oint\limits_{sample} \sigma_s \phi \,\mathrm{d}S\,. \tag{3.1.9}$$

Both integrals are taken over the sample, whereas ϕ is calculated over the magnetized tip. Obviously, both surface charges apparent for out-of-plane easy axis materials and volume divergences within domain walls except symmetric Bloch walls can in principal be observed by MFM microscopy. Therefore, even pure in-plane magnetized materials cause a magnetic signal due to domain boundaries. Although only domain walls are apparent, further knowledge of the system can provide the required information to assign the corresponding domain orientations.

3.2. Magneto-Optical Kerr Microscopy (MOKE Imaging)

MOKE imaging is, due to its direct dependence on magnetization, one of the most suited and favored observation techniques for surface sensitive investigations of magnetic samples, such as thin films. In the following both physics of the magneto-optical Kerr effect and the experimental setup are presented.

3.2.1. Magneto-Optical Kerr Effect (MOKE)

3.2.1.1. Phenomenological Approach

Polarized electromagnetic waves penetrating a medium, which exhibits either magnetization or a magnetic field, are known to be affected in their plane of polarization (see Fig. 3.4). The effective permittivity $\tilde{\varepsilon}$ up to the first order of such media consists of the normal diagonal and off-diagonal elements, causing the rotation [see HS09].

$$\tilde{\varepsilon} = \varepsilon \begin{pmatrix} 1 & iQ_z & -iQ_y \\ -iQ_z & 1 & iQ_x \\ iQ_y & -iQ_x & 1 \end{pmatrix} = \varepsilon(1 - i\boldsymbol{Q}\times)\,. \tag{3.2.1}$$

Here, Q_i are the frequency dependent Voigt constants describing the strength of birefringence. For an uniformly magnetized medium only $Q_z(= Qm_z)$ has to be considered, leading to $Q = i\frac{\varepsilon_{xy}}{\varepsilon_{xx}}$ [YS96]. Hence, the eigenmodes of such a system are left- and right-circular plane waves with $n_{R/L} = n(1 \pm \frac{1}{2}\boldsymbol{Qk})$ as the refractive indices. In case of reflection the magneto-optical Kerr effect can be considered by introducing additional Fresnel coefficients r_{ij} [YS96].

Since the angle of rotation is defined as $\theta^s = \frac{r_{ps}}{r_{ss}}$, the longitudinal MOKE signal ($m_y = 1$,

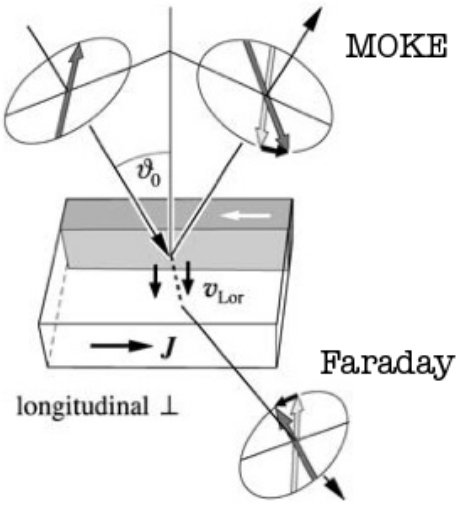

Fig. 3.4: *The sketch shows a magnetic domain, exhibiting a magnetization longitudinally aligned with respect to the incidence light. The polarization plane of the s-polarized light is rotated due to MOKE or Faraday effect [HS09].*

perpendicular to s-polarized light) can be calculated by:

$$\theta_l^s = \frac{in_0 n_1 \cos\vartheta_0 \tan\vartheta_1 Q}{(n_1^2 - n_0^2)\cos(\vartheta_0 - \vartheta_1)}\,. \tag{3.2.2}$$

The indices 0 and 1 refer to non-magnetic and magnetic medium, respectively. ϑ_0 is the angle of incidence. Hence, the magnitude of Kerr rotation depends on the wavelength, as shown in Fig. 3.5, and the angle of incidence. Provided the knowledge of all these parameters quantitative investigations are possible. A Kerr rotation of $\theta_l^s < 0.02\,$degrees for Ni in ambient conditions illustrates the required sensitivity.

Due to the penetration depth $z_d = \lambda/4\pi n''$ depending on wavelength λ, the Kerr rotation θ becomes a function of depth z [see TWH92]:

$$\mathrm{d}\theta(z) = \theta\rho \mathrm{e}^{-\rho z}\,\mathrm{d}z\,, \tag{3.2.3}$$

with $\rho = 4\pi i \cos\vartheta_0 (n' - in'')/\lambda$ and the complex refractive index $n = n' - in''$. This allows, for instance, to differentiate of the magnetization in thin multilayer systems. The information depth $z_0 = \lambda/8n'$ describing the first zero crossing point can be obtained from (3.2.3). If z_d is remarkably larger than z_0, interference occurs. However, that is not the case for nickel, since both z_0 and z_d are approximately 20 nm.

3.2.1.2. Physical Origin

Within this paragraph the motivation for (3.2.1) is given for a simplified case. Due to the polarized light electrons oscillate within the polarization plane. The existing magnetic field, originating from the magnetization, causes according to the Lorentz force (3.2.4) an

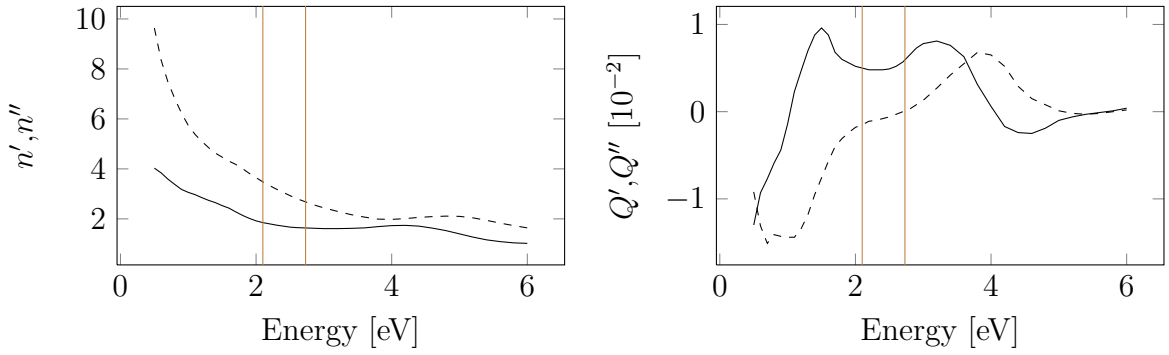

(a) (b)

Fig. 3.5.: *Refractive indices (a) and Voigt constants (b) as a function of energy of nickel. Within visible range: $Q' \approx 0.005$, $n' \approx 2$ [Lab11]. The energy range, used within this thesis, is illustrated by brown vertical lines.*

acceleration perpendicularly to both electric and magnetic field. Here, m is the electron mass, ω_0 the eigenfrequency, τ the relaxation time, e elementar charge and c the speed of light.

$$m\ddot{\boldsymbol{r}} + m\omega_0^2\boldsymbol{r} + \frac{m}{\tau}\dot{\boldsymbol{r}} = -e\boldsymbol{E} - \frac{e}{c}\dot{\boldsymbol{r}} \times \boldsymbol{B} \tag{3.2.4}$$

This results in an avoidance of degeneration of right- and left-circular dipoles leading to a preferred orientation and effective angle of rotation. Because the change of susceptibility is caused by the deformation of the orbitals, which is proportional to the Lorentz force, the angle of rotation depends on the wavelength of the incident light.

3.2.2. Experimental Setup

Supporting dynamic investigations in the range of seconds, the wide-field variant (see Fig. 3.6) requires a high power incoherent light source due to widened beam and imaging. A scanning table is not required. Therefore, three LED's in the range of 455 to 590 nm were simultaneously used. Because the Kerr rotation depends on the angle of incidence (3.2.2), the light is focused on the back confocal plane of the objective to provide a parallel incidence. The observation of the magnetic domains is achieved by the detection of the rotation angle of the polarization plane of the incident light, caused by the Kerr effect (3.2.2). Hence, adjusting a deviation from crossed polarizers, equal to the Kerr rotation θ_l^s, the incidence of s-polarized light leads to a superimposition of topography and three different contrasts, which refer to the magnetization, as follows:

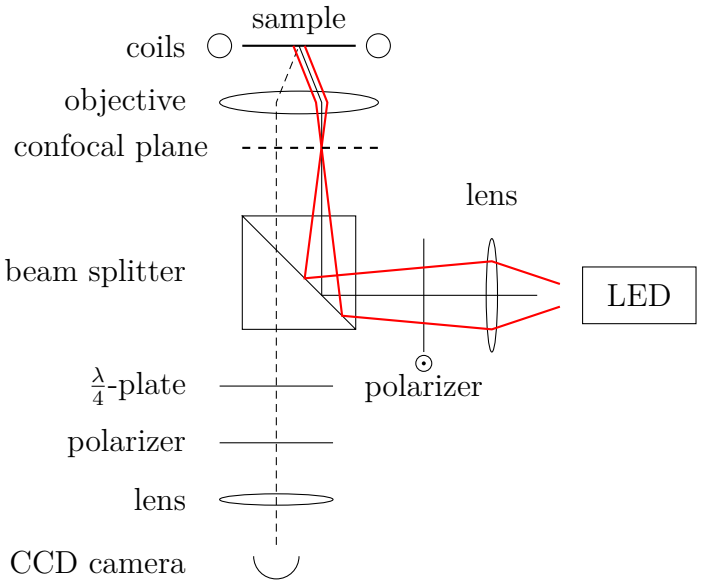

Fig. 3.6.: *Favored setup for wide-field Kerr microscopy. Since the Kerr rotation depends strongly on* $\boldsymbol{E} \times \boldsymbol{B}$ *a small angle distributions is required, which can be achieved by focusing on the back focal plane.*

dark:	longitudinal 1,
bright:	longitudinal 2,
gray:	transverse/ polar.

Taking this image as background and changing the sign of the deviation angle, provides an actual magnetic image due to canceling of the topography. As a result, the Kerr rotation can be calculated.

Within this thesis, a dynamic procedure was used to obtain the magnetic signal. The images were taken with a specialized polarization microscope of the group of Dr. Rudolf Schäfer at the IFW Dresden. The principle setup is shown in Fig. 3.6. The magnetic signal is obtained by background subtraction of an image, taken during the application of a magnetic field, which oscillates at a frequency of 11 Hz with an appropriate amplitude, from the actual demagnetized state. The magnetic ground state is obtained by reducing the oscillating amplitude of the magnetic field perpendicular to the easy axis. Since the demagnetization is confined to the plane of the sample due to the high shape anisotropy of the thin film, the observed ground state represents a quasi-equilibrium state. The distribution of the surface normals caused by the topographical steps of tetragonal BTO does not have an observable influence on the switching behavior, though. Each state was averaged over 16 images within two seconds. To create magnetic fields up to 500 mT iron cores with an adjustable spatial separation were used. The calibration was done by

measuring the Hall voltage. As a result, a vertical displacement of 1 mm causes a relative deviation of the actual magnitude of up to 10%. The magnetic ground state is obtained by reducing the oscillating amplitude of the magnetic field perpendicular to the easy axis. Since the demagnetization is due to the high shape anisotropy of the thin film confined to the plane of the sample, the observed ground state represents a quasi-equilibrium state. The distribution of the surface normals caused by the topographical steps of tetragonal BTO does not have an observable influence on the switching behavior, though.

Every magnetic hysteresis, shown within this thesis, was already corrected with respect to diamagnetic and Faraday rotations, mainly due to the optics of the setup, causing a linear de- or increase of the magnetic intensity with increasing magnetic field. Therefore, images taken at fields higher than roughly 300 mT are either over- or underexposed. Although appropriate fixing of the sample with the aid of silver conducting paste suppresses lateral vibration due to the AC field, any defocused particle, such as dust, will show over- and underexposed edges in the MOKE image due to background subtraction and the slightly changed angle of incidence caused by the interaction with the magnetic field.

3.3. Superconducting Quantum Interference Device (SQUID) Magnetometer

Within this section, the SQUID magnetometer is presented. This technique allows to measure quantitatively magnetic hystereses. For signal correction, certain scaling factors are required. Therefore, both experimental setup and theoretical fundamentals are given in more detail.

3.3.1. Experimental Setup

Fig. 3.7 illustrates the setup of the SQUID magnetometer, fabricated by Quantum Design [Des10b], used within this thesis. The arrangement of the four pick-up coils of two different winding orientations (+ and −) located at $\pm b, \pm l$ has the advantage of suppressing both constant and linear magnetic fields $\boldsymbol{H_0}$. Hence, the homogeneous driving field for magnetic hystereses will not be detected at all. Additionally, the localization accuracy of the sample is much higher than for configurations using less coils.

Since the temperature of the sample can be adjusted, but the SQUID needs to be cooled, a transformer is required as thermal separation. As shown, the dc-SQUID consists of a superconducting ring with two metal junctions ×, also know as Josephson junctions, which

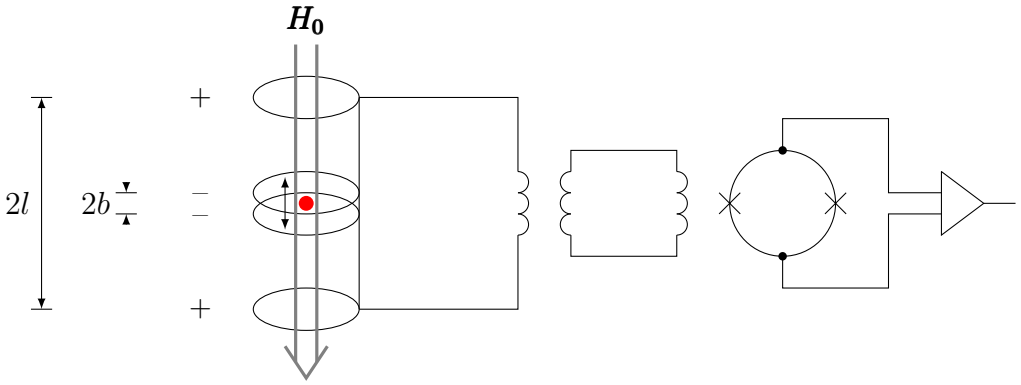

Fig. 3.7.: *Principle of a SQUID magnetometer. The left part illustrates a second-order gradiometer, consisting of four pick-up coils of two different orientations (+ and −). Due to this arrangement neither homogeneous nor linear magnetic fields are detected. The sample (red) oscillates near the center, while a homogeneous magnetic field can be applied to drive magnetic hystereses. The actual SQUID is shown at the right, providing input to the operational amplifier. The crosses demonstrate the two Josephson junctions of the dc-SQUID. A transformer is placed in between to provide a spatial separation, required for adjustable sample temperature.*

determine the current flowing in the ring. The generated magnetic field of the transformer causes a proportional change of the magnitude of the junction current (see A.3) and, hence, of the voltage applied to the operational amplifier. Moreover, the sample oscillates at 14 Hz and an adjustable elongation to minimize the measurement time. Using a lock-in amplifier allows the detection at this frequency. Due to the setup both sensitivity and accuracy are enormously hight (10^{-7} emu). Since $\boldsymbol{H}_0$ is measured inductively the resulting value is accurate, but affected by the enclosed flux lines within the superconductor. Thus, the offset has to be considered.

3.3.2. SQUID Signal and Scaling Factors

Although the investigated samples are usually extended in at least two dimensions, the physical treatment as a magnetic dipole is still valid. The magnetic field of a dipole located at the origin is, as known:

$$\boldsymbol{H} = \frac{(\boldsymbol{m}\boldsymbol{e}_r)\boldsymbol{e}_r - \boldsymbol{m}}{r^3}\,. \tag{3.3.1}$$

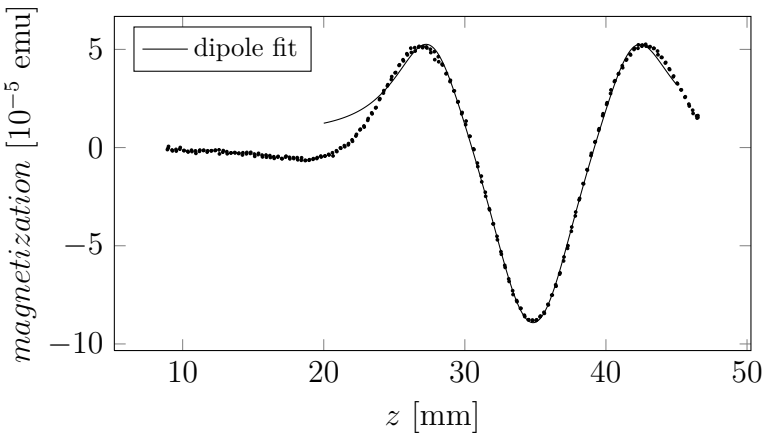

Fig. 3.8.: *The graph shows the magnetization of a 50 nm thick Ni film detected by SQUID as a function of height z. Obviously, the approximation as a magnetic dipole is acceptable, since the fit matches quite well. The sample is positioned near 34 mm. Additionally, the magnetization is simply the magnitude.*

Calculating the overall magnetic flux ϕ for all four coils, positioned at $\pm l$ and $\pm b$, with a radius a ($\approx 3\,\mathrm{mm}$) and a magnetization aligned parallel to the symmetry axis z leads to:

$$\phi(z) = -\frac{a^2 m(z)}{2}\left(\frac{1}{((z+l)^2+a^2)^{3/2}} + \frac{1}{((z-l)^2+a^2)^{3/2}} - \frac{1}{((z+b)^2+a^2)^{3/2}} - \frac{1}{((z-b)^2+a^2)^{3/2}}\right). \tag{3.3.2}$$

Further simplification of constant magnetization, although certainly not accurate, and a potential offset, caused by enclosed flux lines, suits very well the measured distributions, as shown in Fig. 3.8 for a 50 nm thick Ni film without any radial offset. The physical explanations for this proportionality of signal and potential will be elucidated in A.3. As a result, a constant has to be inserted, which can be treated as calibration parameter for magnetization. The corresponding magnetization of the sample is obtained from the second peak. Considering other peaks would increase the error significantly. The distance between the two maxima is equal to the length of the cylinder $2l$.

However, due to lateral expansion, the measured signal of long samples will be much lower, since the stray field does not leave entirely the cylinder. If sample and oscillation amplitude are too small, the stray field will be closed within the cylinder resulting in a lower value, too. The corresponding scaling factor for square samples was published by Q-Design itself, showing quadratic behavior for both in- and out-of-plane hysteresis [see Fig. 3.9(a)]. The deviation, caused by this approximation, is for a $2.2 \times 2.65\,\mathrm{mm}^2$ sample $\approx 2.5\%$. Furthermore, as shown in Fig. 3.9(b), the enclosure of magnetic flux lines

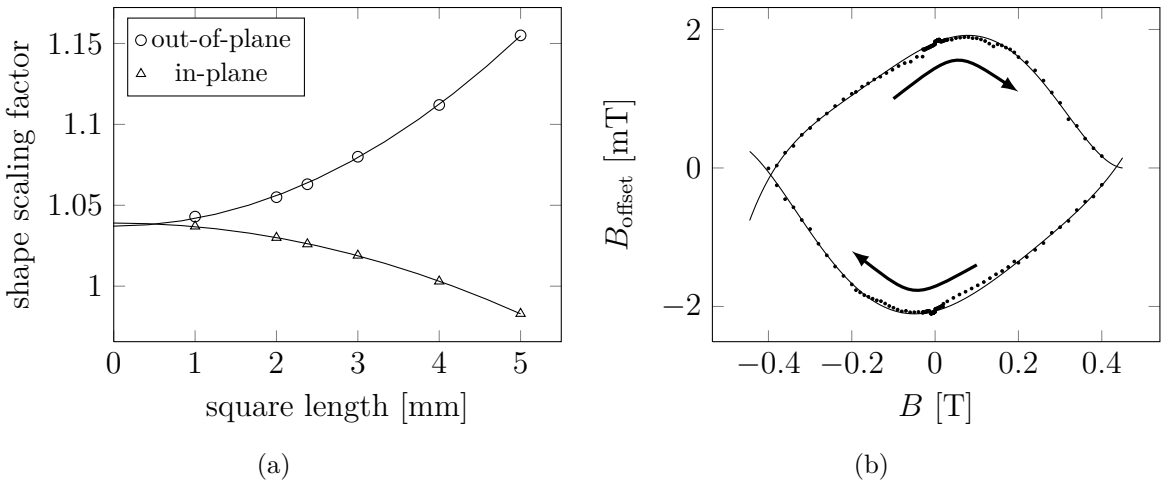

(a) (b)

Fig. 3.9.: *The two graphs show SQUID scaling factors for consideration of extended samples (a) and field correction due to magnetic flux lines (b), obtained with a Pd cylinder. Obviously, the shape scaling factor can be fitted with the aid of second-order polynomial (from [Des10a]). Additionally, changing the discretization of the magnetic field affects the magnetic flux lines within the SQUID. Hence, the corresponding error is quite large.*

within the superconductive ring causes a measured field below the actual one, resulting in a negative coercivity $B_{\text{offset}}(0)$ for paramagnetic samples, such as Pd. Since their distribution and contribution depend on measurement time and discretization, as well as maximum field, it has to be measured for each run.

However, the radial offset has a much larger impact on the magnetic hysteresis, including magnetization and shape, as shown in Fig. 3.10. This influence was investigated with the aid of a 50 nm thick Ni film sputtered on top of a 50 μm thick copper plate. The solid hysteresis was obtained by adjusting the sample at the very center, whereas a 500 μm thick Cu plate was used as a buffer for the dashed line. The corresponding radial offset is similar to those of the investigated Ni/$BaTiO_3$ samples. Since only the radial offset was changed by retaining sample shape and measurement sequence, the ratio between the saturation magnetizations should be the scaling factor describing the radial offset. As can be extracted from Fig. 3.10, the corresponding value is 0.624 ± 0.006. Since the magnetic field gradients differ for centered and misaligned positions, the induced current varies, leading to a slightly broader hysteresis. An actual error can not be given, since it depends on the shape itself. However, for small switching fields, as shown in Fig. 3.10, the value is in the range of 1 to 2 mT, for larger up to 20 mT.

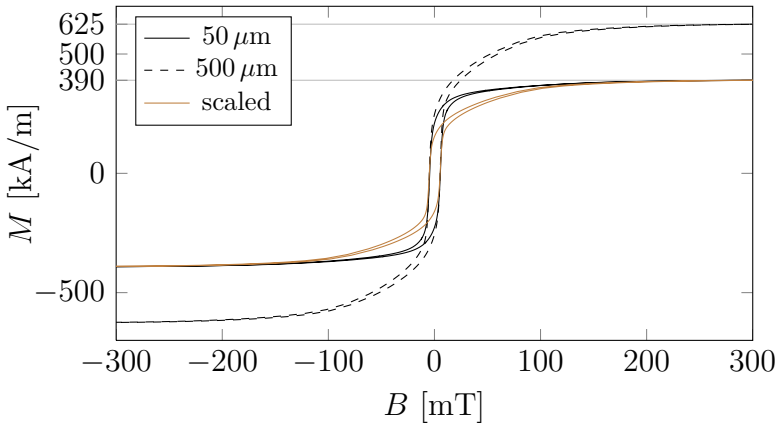

(a)

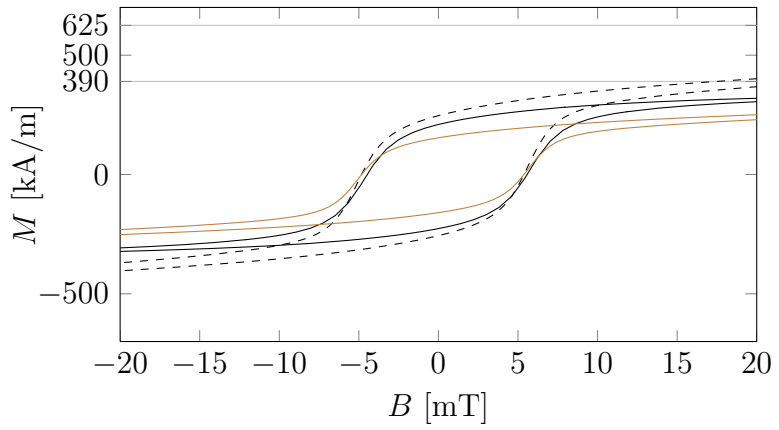

(b)

Fig. 3.10.: *SQUID hystereses of a 50 nm Ni film with a radial offset of 50 μm and 500 μm to determine the corresponding scaling factor of* 0.624 ± 0.006. *Although the saturation magnetization could be adjusted, the shape of the hystereses can not be modified properly due to different field gradients (see brown line).*

3.4. Scanning Electron Microscopy (SEM)

The scanning electron microscope is a rather surface sensitive measurement technique allowing, for instance, the detection of topography, magnetic and electric structures, and element identification. An collimated electron beam originating from an electron gun is pointed at the sample. Due to locally topography, varying Bragg reflection conditions and Lorentz force the electrons are deflected differently, leading to a different amount of detectable electrons. The imaging is proceeded by deflecting the electrons with the aid of tunable magnetic coils. Because of wave-particle duality, the resolution can be adjusted by the kinetic energy of the electrons (10–30 kV), as long as the sample remains unaffected. In general, the image shows a superimposition, which makes it impossible to distinguish between true topography and interactions. However, using a 4-quadrant photodiode solves this discrepancy, since subtraction and summation can be proceeded. For instance, subtraction of the signal of opposite photodiodes reveals only the topography, whereas the summation results in elimination of the topography.

In our case, the purpose of using SEM was the observation of ferroelectric domains. The detectable contrast is caused by different lattice constants, leading to changed Bragg conditions. An effective contribution due to the interaction with the electric field, originating from the polarization, is not observed. This means, that both c^+ and c^-, and a^+ and a^- are not distinguishable by SEM, as reported by [YK98], too.

3.4.1. Electron Backscatter Diffraction (EBSD)

In EBSD mode the electrons hit the cleaned/ as-deposited sample at a shallow angle of approximately 20°, emanating spherically from the incident beam point (see Fig. 3.11, [MS07]). The small angle reduces the penetration depth and, hence, the diffuse background due to unelastic scattering within the sample. Due to the high amount of electrons and rather isotropic scattering each lattice plane is represented by diffraction cones. Placing a crystal lattice, such as a phosphor screen, a short distance from the tilted sample leads to constructive and destructive interference due to channeling. Within the phosphor screen the diffracted electrons are converted into light, detectable by a CCD camera. The nominal angular resolution is 0.5°; the spatial resolution is limited by SEM optics and penetration depth. In case of single-crystal substrate the interference causes so-called Kikuchi bands of a certain width, as shown in Fig. 3.12. Whereas polycrystalline samples would cause similar but split patterns, amorphous samples show a halo due to the lack of any far ordering. With the aid of Kikuchi patterns the crystal structure can be determined and even the distribution of the crystal orientation can be mapped by scanning the sample.

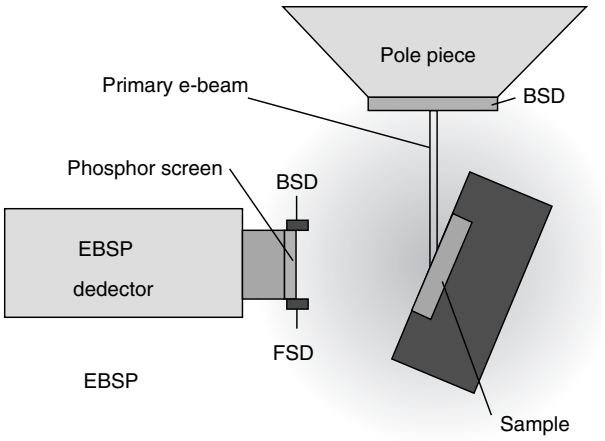

Fig. 3.11.: *Principle of SEM, operating in EBSD mode. The primary electron beam hits the sample at a shallow angle. At the incident point the electrons are diffracted spherically. The phosphor screen converts the electrons into light according to constructive and destructive interference, which is detected by the CCD camera. (from [MS07].)*

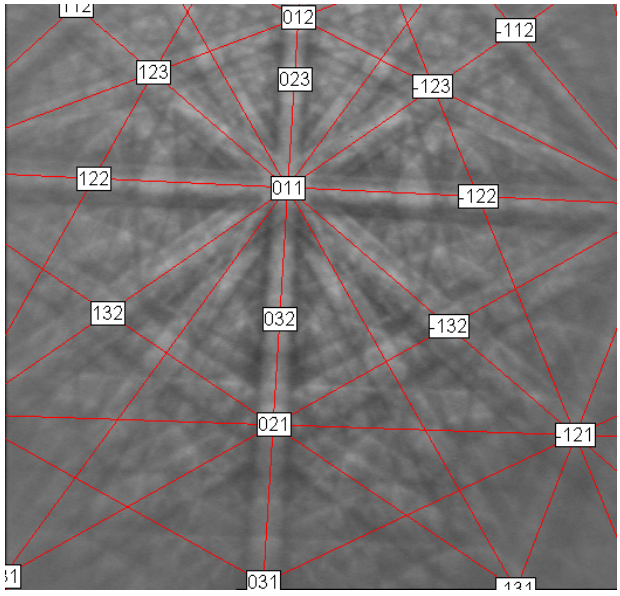

Fig. 3.12.: *Kikuchi pattern of single-crystal barium titanate. Neither cracks nor blurring within the pattern are apparent, indicating perfect single-crystallization. The crystal orientations are illustrated by the Miller indices. As usual, no further scale is shown.*

4. Samples

Since the magnetostrictive film is deposited rather stress-free on top of the substrate, whose lattice constants depend strongly on the deposition conditions, different parameters will affect the resulting displacement of the surface atoms. Hence, a series of different deposition conditions was prepared and investigated. As usually, the investigated thin films were prepared by Sputtering and Electron Beam Vapor Deposition (EBVD), allowing qualitatively high samples.

4.1. Preferences for Ni/$BaTiO_3$

The investigation of the strain-mediated coupling between ferroelectric and ferromagnetic properties in magnetoelectric composites were carried out at a two-component composite consisting of a nickel film deposited on top of single-crystal barium titanate, as shown in Fig. 2.4. The thickness of the crystal was chosen to be 500 μm, leading to optically observable ferroelectric domains. Since we focus on fundamental investigations a minimization of the width of ferroelectric domains is of no particular interest. Additionally, we chose single-crystal instead of polycrystalline substrates to avoid local inhomogeneity.

In particular, barium titanate was the substrate of choice due to its tetragonal unit cell (see 2.1.3). The values of a and c-domains are 4.04 Å and 3.99 Å [Sur11], respectively, illustrating a difference of 5 pm or 1%. At a temperature of 120°C the unit cell becomes cubic with a lattice constant of 4.01 Å. The choice of the magnetostrictive, ferromagnetic layer was determined by a simple composition of one or two elements, preferring elemental Fe, Ni, Co, and a large magnetostriction constant. Although Co would have fulfilled the requirements as well, nickel was chosen.

As shown in Tab. 4.1, six samples, prepared at different deposition conditions, were investigated. Within this series, parameters, such as deposition rate, substrate holder temperature and film thickness of the amorphous Ni layer were varied to determine their influences. Within this thesis the morphology of the magnetostrictive film is assumed to be amorphous. A nanocrystalline arrangement would not affect the volume density and corresponding properties significantly, since intercrystalline areas exhibit amorphous

Tab. 4.1.: *Overview of investigated $Ni/BaTiO_3$ samples. The gas pressure is 10^{-3} mbar and $5 \cdot 10^{-8}$ mbar for Sputtering and EBVD, respectively.*

name	thickness [nm]	deposition rate [nm/min]	holder temperature [K]	deposition technique
NBFL	50	3.6	300	Sputtering
NBPL	50	3.6	470	Sputtering
NBFH	50	33	300	Sputtering
NB50	50	6-12	300	EBVD
NB20	20	6-12	300	EBVD
NB100	100	6-12	300	EBVD

characteristics [HGKM+05].

4.2. Nickel Deposition

Both target and substrate (actual sample) are placed oppositely within a vacuum vessel. In case of sputtering the inert gas, aimed to the target, is ionized inside the electron plasma located above the target. The ions are accelerated up to an energy of 50 to 1000 eV due to an applied electric field [PLW+07]. Within this range few target atoms are dislodged. To guarantee optimal momentum transfer both gas and target atoms should be of the same weight. However, the optimum of efficiency will be of the range of one percent showing a large energy distribution up to tens of eV, which are $\approx 100,000$ K. Therefore, the substrate will be heated during deposition, leading to a change of lattice constants for ferroelectric materials. A transition of straight impact for low pressure to slow random walk for high pressure can be attained, though the pressure should be adjusted for each target separately to obtain the best possible film. For instance, the deposition of nickel is usually carried out at a pressure of $p \approx 10^{-3}$ mbar. Since the total heat is still a summation, it can be reduced using a lower deposition rate. In our case, the samples were prepared at lowest possible (3.6 nm/min) and highest possible (33 nm/min) rates by Mrs. Krien from the Leibniz Institute for Solid State and Materials Research (IFW) Dresden.

Contrary, EBVD uses electrons of adjustable kinetic energies, originating from tungsten anodes, to eject target atoms. Since a plasma is not required, the pressure is much lower ($p \approx 5 \cdot 10^{-8}$ mbar). Samples using this technique were prepared by Mr. Geprägs from the Walther-Meissner-Institute for Low Temperature Research Garching.

Part II.

Results and Discussion

5. Characteristics of Barium Titanate Single-Crystal

In magnetoelectric composites the coupling is mediated by strain, originating from changed lattice constants of the substrate. Therefore, a thorough investigation of the ferroelectric domain structure of the barium titanate substrate was carried out first. For this purpose both on- and off-resonance PFM and SEM/ EBSD were applied.

5.1. Correlation between Topography and Ferroelectric Domains

Since the ferroelectric media exhibit several equilibrium states, the ferroelectric domain structure will differ according to the crystal history. For instance, as-grown barium titanate single-crystal usually exhibits large ferroelectric domains with a width of more than 50 μm. Due to this and the lack of any substructures these substrates are rather uninteresting for both PFM and strain-mediated coupling. Therefore, all samples were heated above the transition temperature of 120°C and cooled again, intending to reduce the period of ferroelectric domain alternation. The results are shown in 5.1.2. In spite of several exceptions discussed below each topographical step was found to cause a change of the lattice constant. Considering this, stripes of different reflected intensity, observed by optical measurement techniques, such as MOKE imaging, can be assigned to ferroelectric domains of different lattice constants.

5.1.1. Typical Domain Patterns

The equilibrium state of tetragonal ferroelectrics is according to 2.1.3 a multidomain state, consisting of *a* and *c*-domains and ferroelastic 90° walls. The orientation of the polarization is only confined to the crystal axes, preferring two equivalent in-plane orientations. In case of rectangular substrates, whose edges are cut along the the crystal axes, a major

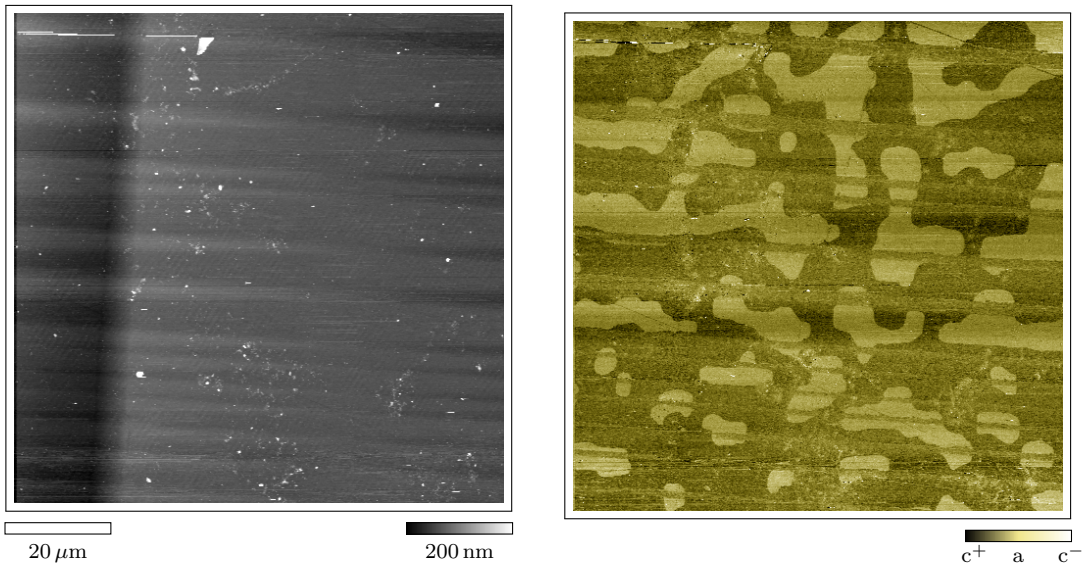

Fig. 5.1.: *Topography (a) and out-of-plane PFM signal (b) of as-grown BTO single-crystal. The PFM signal exhibits patchy distribution of ferroelectric domains for the sake of stray field reduction. The correlation between topography and ferroelectric domains is only valid for small topographical steps, whereas large steps (left), aligned perpendicularly to small ones, exist without any affection.*

orientation of topographical steps is induced, which coincide with the long edge. This is probably due to a lower elastic energy. In principle, there are two possibilities, the system can handle this. If the sizes of the topographical steps are similar, the discrepancy of mismatching lattice constants is solved by forming a_1/a_2-domain patterns within a single step (see 5.2.1). The other case is shown in Fig. 5.1. Apparently, the major axis is determined by the orientation of the smallest steps. The large steps do not even cause any disturbance of the ferro- and piezoelectric properties. This either means an actual imprint or displays an artifact due to polishing. Moreover, Fig. 5.1(b) illustrates the typical patchy c-domain patterns, that appears during growth, electric switching or heating quite often, with an c^--to-c^+ ratio of ≈ 1, minimizing the stray field contribution. Since the polarization is normal to the surface, uncharged domain walls of any shape are favored leading to either straight or curved walls at the surface.

Although the existence of charged 180° domain walls within narrow a-domains is rather unfavored, the local nucleation results in a distribution of charged zig-zag walls within large ones, as shown in Fig. 5.2. Since the unit cells will not shear, zig-zag walls represent nanoscopical steps shielding parts of the electrostatic charges and reducing, therefore, the stray field. Because the energy, required either to flip the polarization or to move the

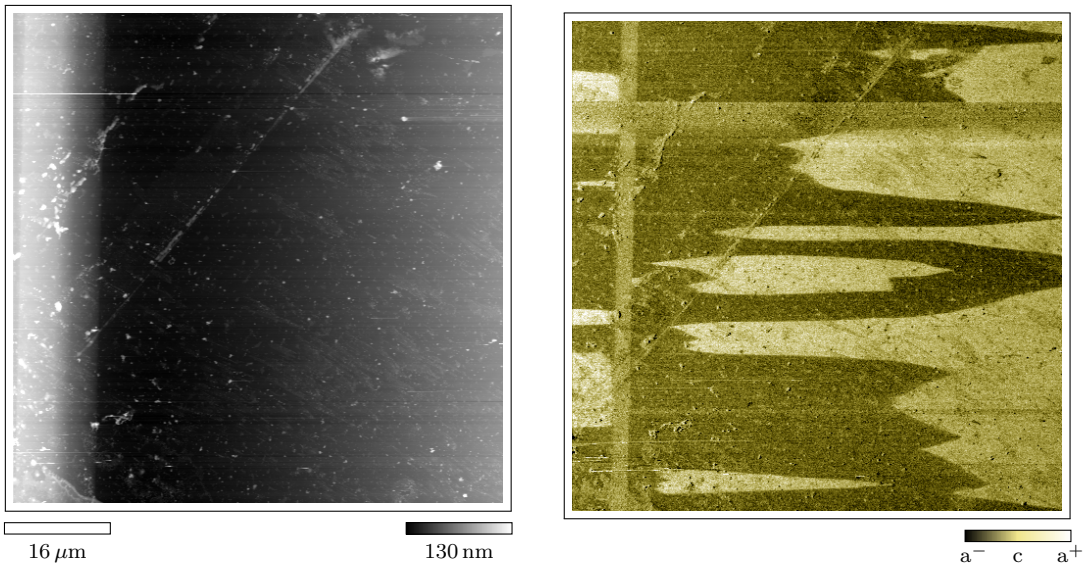

Fig. 5.2.: *(a) and (b) display the topography and the in-plane PFM signal. Since local nucleations result in non-uniform distributions, charged a-domain walls are generated. Contrary to c-domain walls, these walls exhibit a zig-zag form.*

corresponding wall, is larger than the stray field energy, even embedded a-domains with opposite orientation of polarization are stable. The topographical steps, which do not affect the PFM signal, are polishing artifacts. If the substrate is not entirely single-domain during polishing, peaks are cut off, leading to artificial steps with a slope, which may differ from 0.6°. Within these stripes the lattice constant is slightly different due to reorientation of the surface atoms. A change of properties could be observed by both off-resonant PFM and MFM of a nickel-coated area.

5.1.2. Thermal Treatment

To ensure a likely transition into the cubic phase, the barium titanate crystal was heated up to 300°C and kept at the temperature for at least three hours to guarantee a complete phase transition. Cooling in ultra-high vacuum with temperature gradients lower than 0.5 K/min leads to uncharged straight a-domain walls, as shown in Fig. 5.3, with few bubble-like c-domain substructures. The reason for the strong cross-talk of ip into the oop signal is assigned to be due to a miscut of the crystal of few angles, as will be discussed later. An artificial cross-talk due to measurement would have been expected otherwise.

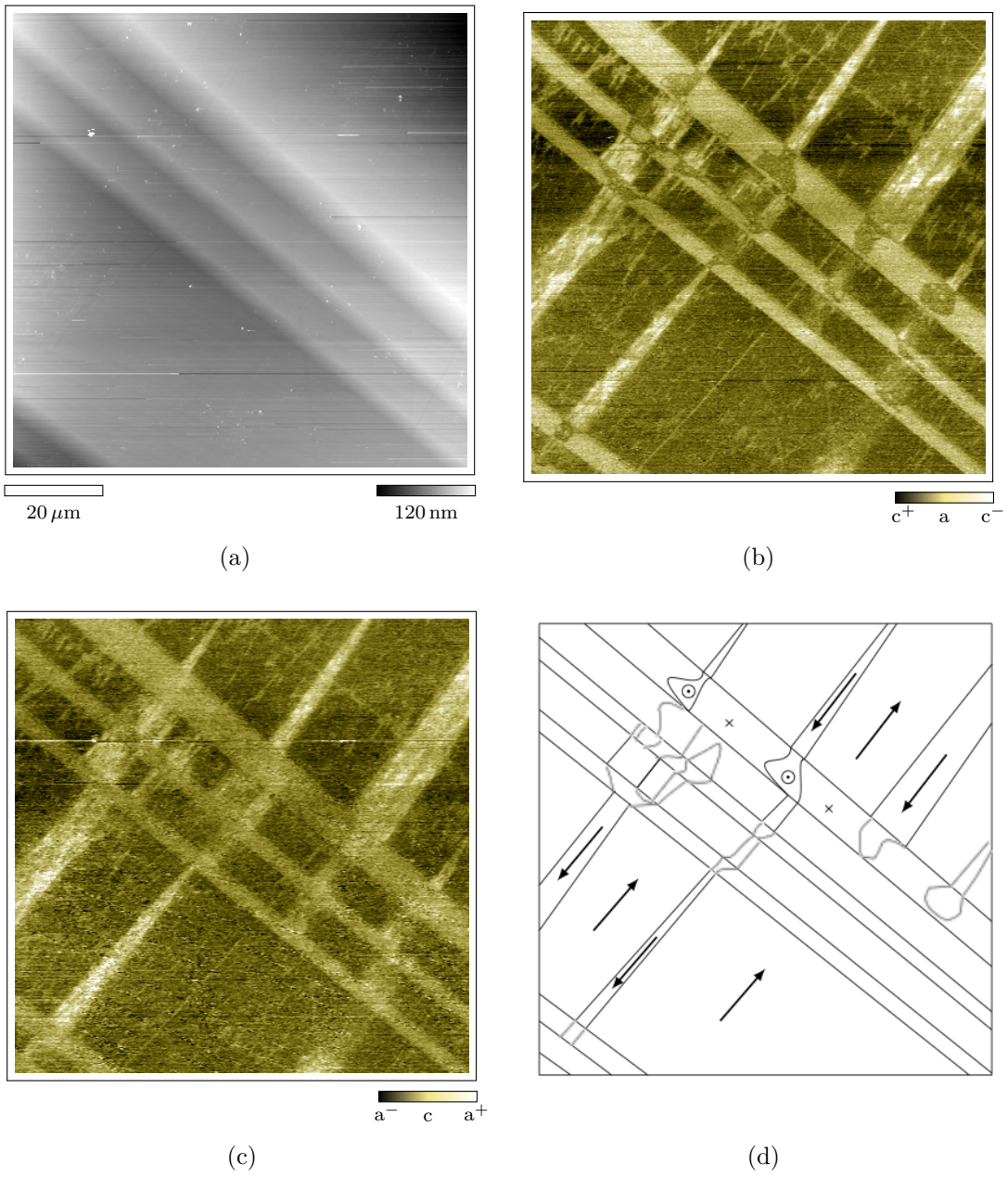

Fig. 5.3.: *Quasi-stationary cooling results in straight uncharged a-domain walls, as shown in (c). The obvious cross-talk of ip into the oop signal is rather due to a miscut of the crystal and higher sensitivity for bending than due to measurement artifacts. The major polarization orientations are illustrated in (d)*

5.2. Determination of the Miscut

During the acquisition of PFM images certain artifacts had been detected, whose appearance could not have been explained without the consideration of slight miscut or misorientation of the unit cell with respect to the surface. Since the investigated samples were polished leading to scratches and high reflection, a miscut is most likely to occur. Because most measurement techniques, such as X-ray diffraction and EBSD, are rather volume than surface sensitive, PFM was the most appropriate method to determine the corresponding angle. However, due to different elastic coefficients for bending and torsion and cross-talk, it is not possible to determine the miscut in any case.

5.2.1. Observation of a_1/a_2-Domain Patterns

One of the most suitable domain structures for the sake of miscut calculation are a_1/a_2-domain patterns, which are assigned to appear in thin epitaxial grown films due to the lattice mismatch between substrate and film [see RPS96]. Although rather unlikely to occur in single-crystals, these patterns have been observed by PFM. Apparently, within a-domains a local oop signal in the form of straight lines occurs [see Fig. 5.4(b)], which distinguishes from the case of simple cross-talk of miscut due to the restriction to the stripes. Additionally, these stripes are aligned under 45 degrees to the topographical steps, reducing their width and period by approaching the c-domain. Moreover, the contrast changes in the same way, the ip signal does, with edges parallel to the topographical steps. Since the topography is flat, ferroelastic a-c-domain walls can be excluded. For further investigations the resolution was increased resulting in Fig. 5.4(d) and (e). One notice the mentioned correlation between oop and ip signal and the stronger contrast within the straight stripes for both signals.

Assuming a slight miscut, Fig. 5.4(f) explains the contrast by displaying the polarization components. Accordingly, a_1/a_2-domain patterns are created in the vicinity of a 90° rotation of the major topographical steps, which is often the case by approaching the corners of finite crystals. The step-like contrast within the ip signal results from the formation of uncharged 90° and 180° walls. Because the tip is aligned under 45 degrees both a-domains cause the same ip signal, which does not allow a direct differentiation. Since the lattice constants do not match for c and a_2-domains, both width and period are decreased by approaching the topographical steps. The additional contrast within the oop signal is due to a miscut with a rotation axis almost perpendicular to the steps. The corresponding angle is positive for an axis oriented from lower right to upper left (x-axis). The actual quantitative calculation will be given in the next paragraph.

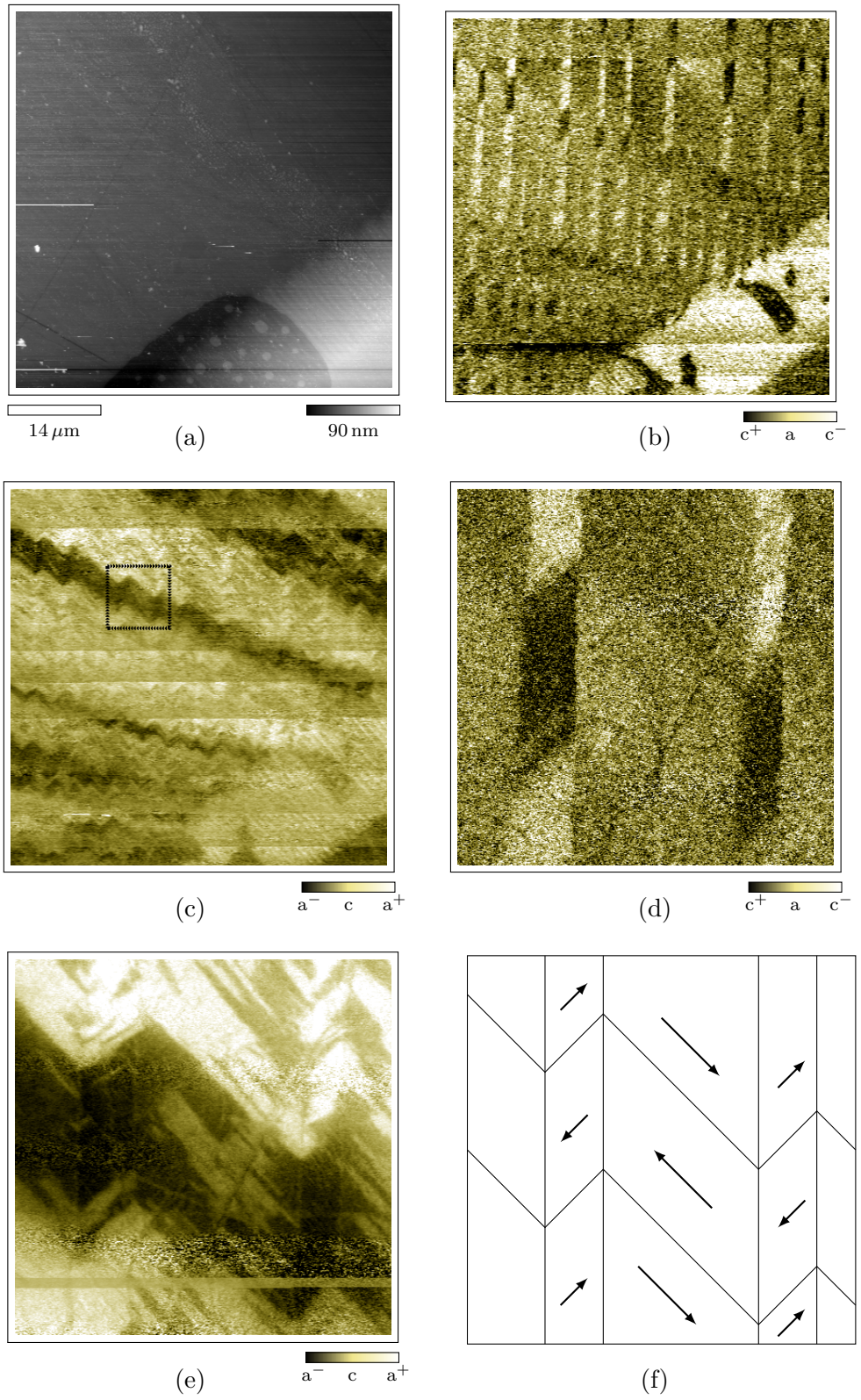

Fig. 5.4.: *The images show topography (a), oop [(b), (d)] and ip [(c), (e)] PFM signal of an area in the vicinity of a 90° rotation of major topographical steps. Additionally, (f) illustrates the corresponding in-plane polarization. Since the tip is aligned approximately under 45 degrees to the steps, the sensitivity for a_1 and a_2-domains is equal. However, due to a slight miscut of the crystal a_2-domains cause according to the modified piezoelectric coefficient an oop signal, which is apparent as vertical stripes within (b) and (d).*

In the vicinity of polishing scratches three different contrasts occur, which belong to the two in-plane orientations and a component, which causes a signal in neither ip nor oop. Such a blurring was also measured by the detection of the Second Harmonic wave of a similar area, proceeded by Thomas Kämpfe within his diploma thesis at the IAPP, TU Dresden. Although both techniques are both surface and volume sensitive, the fluctuating expansion of these grey regions in (e) suggest rather an actual physical influence than simply an artifact due to increased roughness. The occurrence of a miscut leads to a reorientation of the surface atoms, whose bindings could be affected by the scratches, resulting in rather unstructured arrangement and, hence, non-ferroelectric properties.

Another independent verification of a_1/a_2-domain patterns could be given with the aid of SEM. The same crystal was analyzed few months later, illustrating the time-stability. Fig. 5.5 shows the topography (a) and the non-topography/ interaction contributions (b) and (c). The division into these two parts was done, as explained in 3.4. Unfortunately, (a) and (b) do not fit entirely, since the topography was imaged subsequently. However, the horizontal line, displaying the only topography contrast, is apparent in both images. Hence, that line represents a topographical step and c-domain in the corresponding images. Moreover, bright stripes aligned under 45 degrees to that line occur both in the interaction contribution and the EBSD mapping (see Fig. 5.6) but are absent in the topography. Hence, these stripes are a_2-domains, which is in total analogy to the PFM images. Since SEM is rather sensitive to the orientation of the unit cell and the lattice constant than to the polarization, merely one contrast occurs for each a-domain.

With the aid of EBSD, explained in 3.4 as well, a last proof of the existence of a_1/a_2-domain patterns in single-crystals could be given. Detecting the EBSD signal, shown in Fig. 3.12, results in a sharp pattern without any kinks or steps, indicating a perfectly grown single-crystal. Since the crystal structure is known, the corresponding reflexes can be calculated and fitted to the pattern. Scanning the dashed area within Fig. 5.5(c), hence, leads to a mapping of the crystal orientation, which is displayed in Fig. 5.6. The actual angle of distortion can be calculated from the Euler angles revealing the value of $(0.6\pm0.1)^\circ$, measured by PFM.

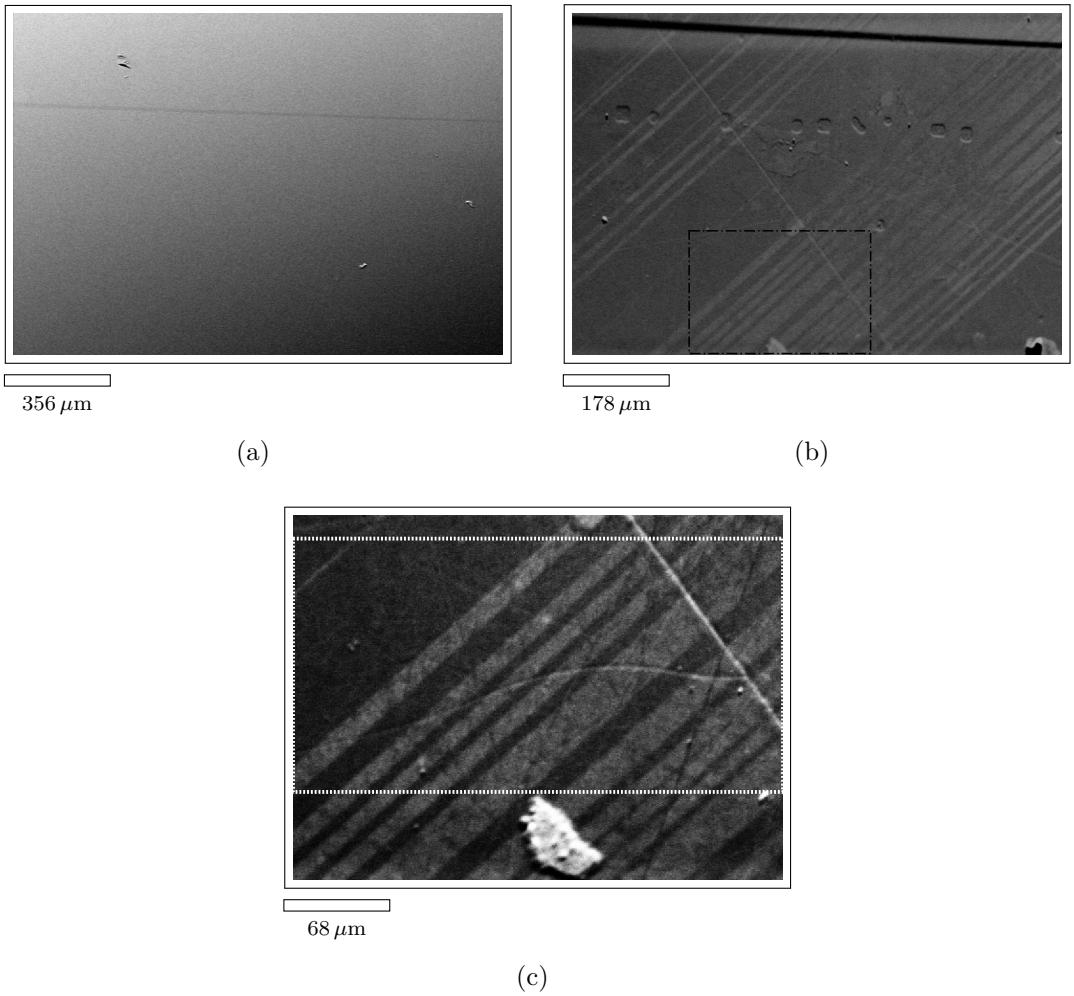

Fig. 5.5.: *The SEM images show the topography (a) and the interaction image (b) and (c). As apparant, the bright stripes within the interaction images are not visible in the topography. Since SEM is merely sensitive to the lattice constant, the actual orientation of the polarization cannot be determined. Hence, the bright stripes correspond to* a_2*-domains embedded by* a_1*-domains.*

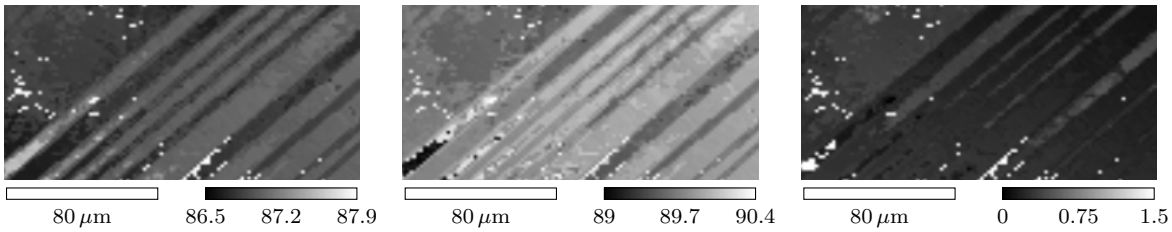

(a) (b) (c)

Fig. 5.6.: *The figures show the local deviation of the three Euler angles from the fitted crystal orientation obtained by EBSD mapping of the white-dashed area in Fig. 5.5(c). The differentiation of a_1 and a_2 is quite obvious. A calculation of the actual distortion angle reveals* $(0.6 \pm 0.1)^\circ$.

5.2.2. Calculation of the Miscut

In the following, the equality of the physical properties of samples with tilted unit cells and samples with tilted surfaces is assumed. This is reasonable, since both cases can be transformed by rotation into each other. Provided the piezoelectric coefficients for non-tilted samples are known, the Euler angles of the rotated unit cell could be calculated with the aid of the ratio of measured and given values. However, since this requires a gauge, quantitative values for elastic coefficients of the tip, deflection and lock-in parameters must be known. Using the ratio of ip and oop signal of the same domain is useless, since this implies the knowledge of those values, too. Therefore, the ratio of the oop signal of c and a-domains, obtained by the measurement, is used to determine the Euler angles. The out-of-plane component is more suited, due to its lower cross-talk and stronger signal, as well as independence of the third Euler angle. The advantage of a_1/a_2-domain patterns is the direct comparison between cross-talk and actual signal due to miscut. Since tip and scan direction were chosen to be aligned under $\pm 45^\circ$ leading to equal conditions, no contrast neither in oop nor ip should occur (see Fig. 5.4).

One of the assumption of calculating the miscut is perfect restriction and, hence, attachment of the tip, leading to a proportional relation between piezoelectric coefficient and PFM signal. For the calculation, the difference between maximum and minimum value of all three types is taken, as shown in Fig. 5.7(a). Because merely the magnitude is important, phase shift and offset do not contribute. However, since the phase difference between positive and negative orientation has to be π, the phase space, as shown in Fig. **??**, should be checked once. In this case the ratio of the oop signal of a_2 and c-domain is 0.32, whereas 0.1 belongs to a_1 and c. Although possible, the latter value was not assigned to be caused

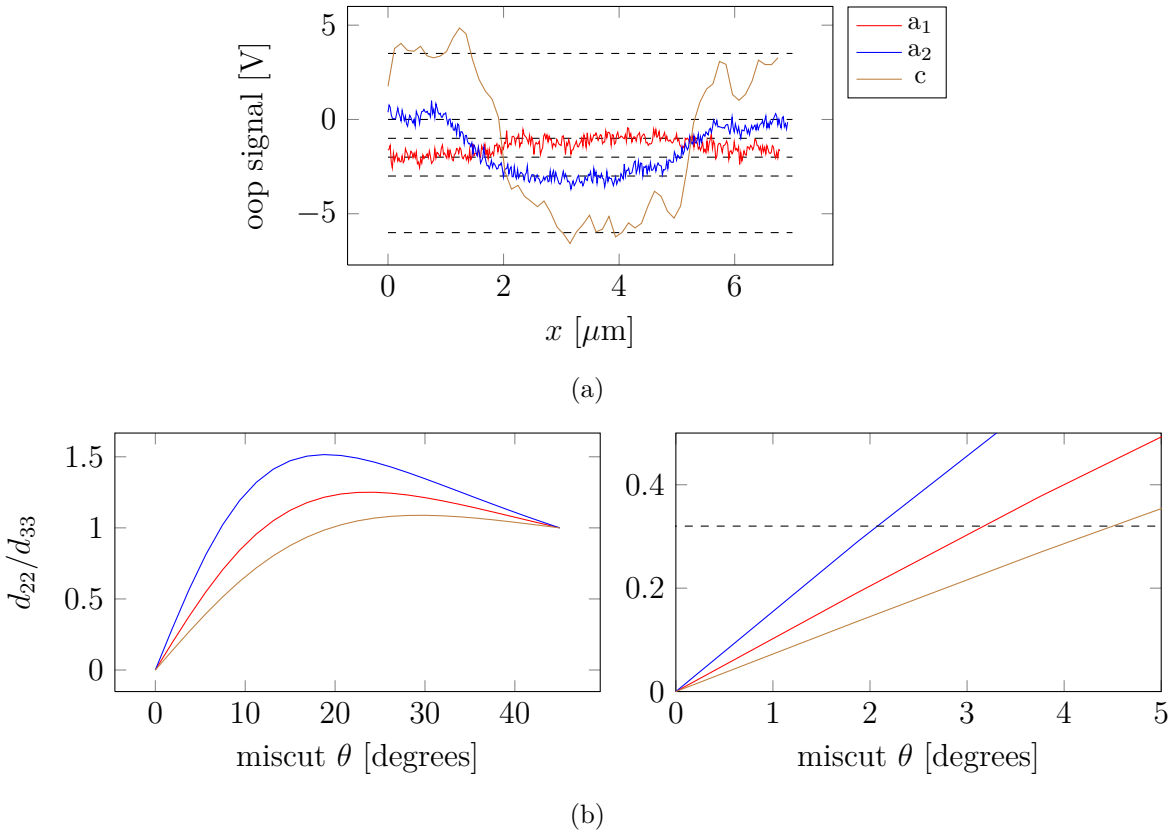

Fig. 5.7.: *(a) shows the cross-section of the oop signal, extracted from Fig. 5.4(e) for a-domains, and (d) for the c-domain. The dashed lines represent the values used for calculating the miscut/ misorientations, of the single-crystal BTO. (b) illustrates the calculated a_2-to-c oop ratio as a function of a single misorientation angle for electric fields normal to the surface and a set of piezoelectric coefficients, listed in Tab. 5.1 (——: Davis, ——: Schaefer, ——: Berlincourt). The dashed line corresponds to the experimental value of 0.32.*

by cross-talk.

In principle, an appropriate calculation of the electric field requires the actual geometry of the tip. Since this is impossible, two different boundary cases shall be given here. Because PFM operates in contact mode, the tip is usually rather flat than sharp. Taking the fabrication diameter of the tip of 30 to 50 nm into account, this suggests an electric field entirely normal to the surface and independent of the geometry. The resulting oop signal, hence, depends only on $d_{33}(\theta, \varphi)$ and on constant coefficients. Here, θ and φ are the Euler angles along x and z, respectively. The last z rotation does not affect the oop signal due to its transverse isotropy. Calculating $d_{22}(\theta, \varphi)$, which is equal to $d_{33}(\theta + \frac{\pi}{2}, \varphi)$, the ratio can be taken, plotted and compared with the measured value [see Fig. 5.7(b)]. For simplicity only one dependence is plotted. Furthermore, three different sets of piezoelectric coefficients

Tab. 5.1.: *Different sets of piezoelectric coefficients for top seeded solution grown barium titanate within the kHz range.*

	Davis [DDHS05]	Schaefer [SSD86]	Berlincourt [BJ58]
d_{33} [pm/V]	90	68.5	85.6
d_{31} [pm/V]	-33.4	-33.4	-34.5
d_{15} [pm/V]	564	647	392

of TSSG barium titanate, given in Tab. 5.1, illustrate the sensitivity. The corresponding range of the miscut angle θ is between 2 and 4.5 degrees. Taken three instead of one variable Euler angles into account, does not change θ remarkable. In fact, the angles are $\theta = 3.16°$ for 1D and $\theta = 3.32°$, $\varphi = 17.32°$ for 3D, with values listed by Davis.

The other extremum case is treated in [EKJ+07] for sharp tips, whose electrostatic sources are aligned along the surface normal leading to an electric field similar to a point source with respect to the surface. Since the theory is quite extensive, it is referred to the paper. Due to the non-normal field components a superimposition of all three piezoelectric coefficients occur, weighted by geometry factors. As a result, both d_{33} and d_{15} influence the bending of the tip, leading to a much larger angle of 18°.

Therefore, the actual angle of miscut/ misorientation is expected to be between 3 and 18 degrees, whereas the upper boundary is very unlikely, since any deformation of the tip would reduce the angle remarkably. Due to this miscut the surface atoms will reorientate by themselves, leading to a quite different arrangement at the surface. Since the corresponding angle is still small, the resulting lattice constants will remain within the uncertainty range.

Conclusion

The correlation between ferroelectric domains and topographical steps of barium titanate single-crystals can be exploited to assign domains of different lattice constants to stripes of varying intensity, observed by MOKE imaging. Thereforem a direct correlation between magnetic domains and regions of similar stress (stress domains) can be stated. Due to polishing artificial steps are induced, which do not indicate a change from a to c-domains, though. Furthermore steps, perpendicular to the major orientation, do not affect the lattice constants as well. Thus, their existence has to be considered. Besides the typically alternation of straight ferroelectric a and c-domains a_1/a_2-domain patterns occur, which show two equivalent orientations of expanded unit cells.

The calculation of the miscut due to polishing reveals an angle within the range of 3° to 18°. Accordingly, the surface atoms will adjust themselves, resulting in a slightly different

lattice constant. The influence of this effect is rather small, though.

6. Influence of Induced Stress on the Magnetic Properties of Magnetoelectric Ni/$BaTiO_3$

Within this chapter the results of both influence and generation of stress, induced into the magnetostrictive nickel film, are presented. The stress originates either from deposition or from an applied electric field. Due to the correlation between topographical steps and ferroelectric domains, stress domains can be assigned to areas of differently reflected intensity, detected optically. Besides the observation of the magnetic equilibrium states with the aid of MOKE imaging, coercivity and switching field/ anisotropy are determined by both MOKE and SQUID magnetometer.*

6.1. Room Temperature Deposition

According to Tab. 4.1, NBFL represents the sample of the lowest possible influence of both deposition rate and temperature, and suits, therefore, as reference sample. Because all other samples, as will be shown later, exhibit a change of lattice constants of barium titanate during deposition, this sample was also supposed to verify, if an unaffected deposition would even be possible. During deposition the nickel atoms are attached rather stress-free to the substrate. Since the growth is not epitaxial, the environment of any atom will differ for distinct lateral translation, which lead to slight intrinsic stress and anisotropy distributions [see FEF+89]. Because the lattice constants did not change during deposition no additional stress is induced [see Fig. 6.1(b)].

The verification of this assumption is given with the aid of Fig. 6.2. It shows the topography, the MFM phases and magnitude of an area of stress-free NBFL right after the

*Although coercivity represents a switching field as well, within this thesis switching fields are defined to be the fields, required to rotate the magnetization into the hard axis by applying a magnetic field perpendicular to the easy axis.

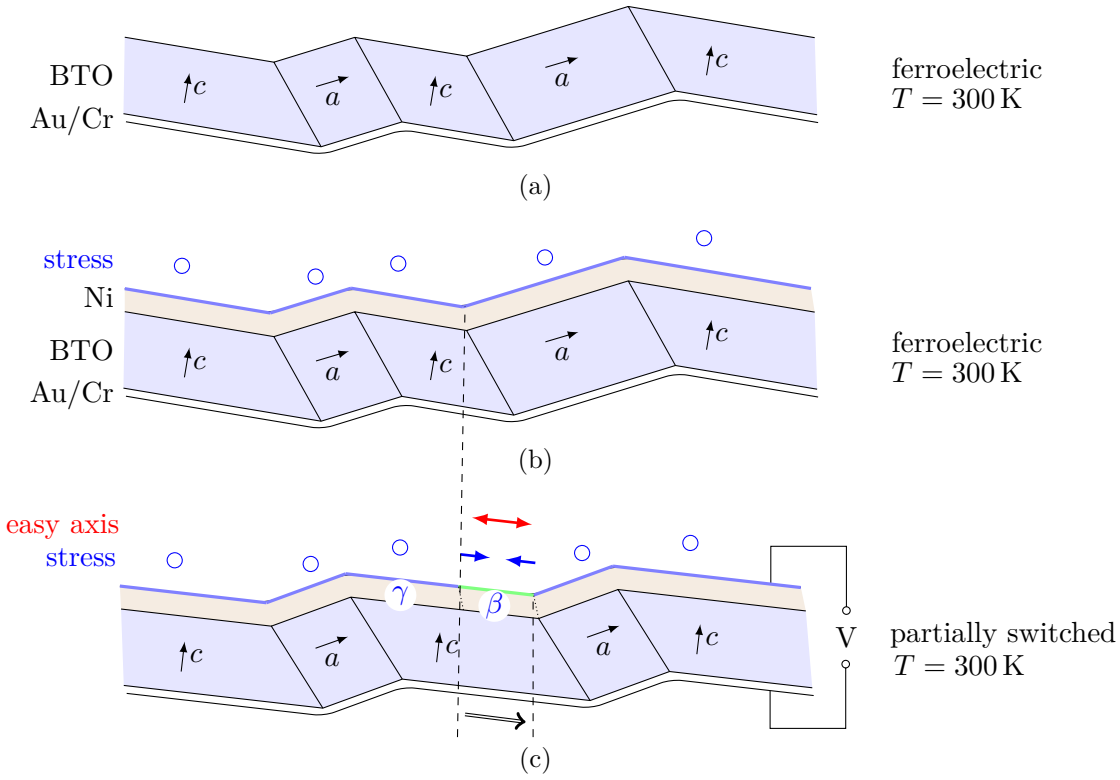

Fig. 6.1.: *(a) Since the deposition was proceeded at room temperature with a very low rate, the transferred heat does not change the lattice constants, leading to a stress-free nickel film at room temperature (b). (c) Applying an electric field to the substrate results in an increase of the density of c-domains. Due to the change of the lattice constants within new c-domains, strain and stress are induced into the nickel film. The corresponding domain, exhibiting uniaxial compressive stress perpendicular to the steps, is called β-domain. Isotropically stressed regions are declared as γ-domains. Because of negative magnetostriction an easy axis perpendicular to the topographical steps is formed, exhibiting a large anisotropy.*

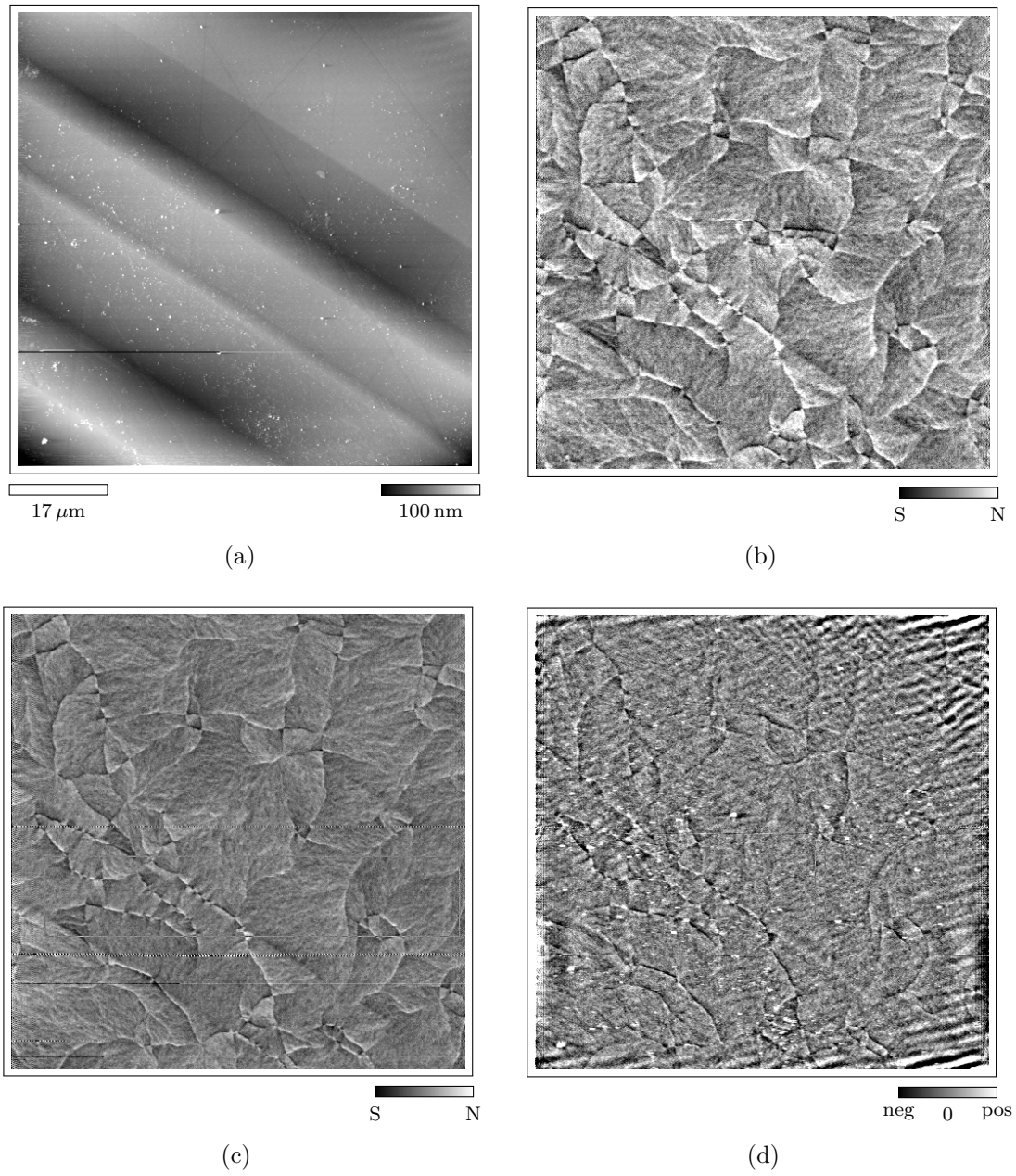

Fig. 6.2.: *Randomly distributed magnetization vectors in stress-free NBFL. (a) - (d) show the topography, MFM phase signal [tip-sample distance: 100 nm (b), 20 nm (c)] and the magnitude of an area of stress-free NBFL right after deposition. The bright and dark contrast in the MFM phases originate from the stray fields, generated by magnetic domains walls within the nickel film. The gray regions represent in-plane magnetized domains, which do not contribute to the signal, as can be seen in (d). Apparently, the minimized values of deposition rate and temperature lead to a stress-free attachment without any favored orientation of the easy axes or correlation between topography and magnetic domains.*

deposition. (b) taken at a tip-sample distance of 100 nm was the very first scan, while (c) was taken right after at a distance of 20 nm; both acquired at a line scan frequency of 0.6 Hz. Apparently, the resolution is increased, which applies also for topographical cross-talk. Since the purpose of the investigation is the qualitative analysis, a constant tip-sample distance of 100 nm is used for every scan shown in this thesis. Although the use of sharp, low-magnetized tips reduces the magnetic interaction significantly, few domain walls represented by dark and bright lines, are moved or even annihilated. The gray regions in the MFM images belong to in-plane magnetized domains, which do not contribute, due to lack of stray fields, to the MFM signal at all [see (d)]. Because out-of-plane magnetization vectors would cause, at least, the same magnitude of phase shift than domain walls, such a distinction is only available for pure in-plane magnetized domains. The absence of any favored easy axis of magnetization is quite obvious. Since the substrate does not induce any stress into the magnetostrictive film, neither a correlation between topography/ ferroelectric domains and stress/ magnetic domains nor an easy axis could be observed and expected.

Since the observed domain structures do not represent the actual equilibrium state, the sample was demagnetized by an oscillating magnetic field and investigated optically with the aid of MOKE imaging. Due to the uniform contrast of the MOKE image merely the magnetic hystereses of the stress-free sample are shown. Solid and dashed line in Fig. 6.3 display the longitudinal and transverse hysteresis, respectively. Considering s-polarized light, longitudinal contrast coincides with the magnetization component, aligned parallel to the topographical steps. In analogy, transverse refers to perpendicular alignment. The corresponding switching fields are similar due to the lack of an easy axis, namely (1.6 ± 0.3) mT. The longitudinal hysteresis has, due to the averaging of a large area including topographical steps, the shape of a superimposition of hard and easy axes switching. Although every environment would show a hysteresis like the transverse loop, slight pinning along topographical steps causes within this range significant impact. Because slightest vibration or pressure can lead according to (2.1.5) to very small motion of ferroelectric domain walls, stress is supposed to appear at the very edge of these steps, leading to an increased switching field. Since the width is too small, magnetic domains are not expected to occur. The existence is even not detectable in the transverse hysteresis.

The next step is the application of an electric field normal to the sample, leading to an increase of the density of ferroelectric c-domains. According to Fig. 6.1(c) the change of the lattice constant induces strain and stress into the nickel film. The corresponding stress domains are declared in Fig. 6.1(c) as well. Consequently, β-domains refer to uniaxial compressive stress, whereas γ-domains show isotropic stress. Since nickel is supposed

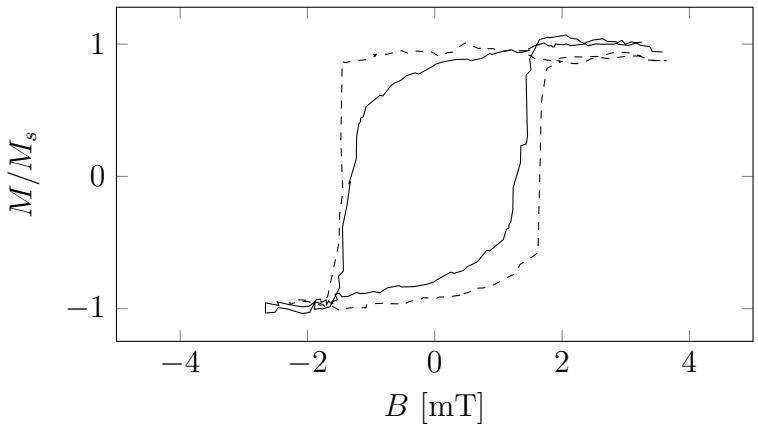

Fig. 6.3.: *Longitudinal (solid) and transverse (dashed) magnetic hystereses of stress-free NBFL verify the absence of any induced stress, originating from the substrate. The differences between both graphs are assigned to be due to slight motion of the ferroelectric domain walls sensitive to external pressure, which causes at the very edge of the topographical steps an induced stress.*

to show negative magnetostriction [Lee55], a remarkable change of both magnetic easy axis and switching field are likely to occur in β-domains (see 2.2.3). The corresponding longitudinal demagnetized state is shown during the application of a magnetic field of 60 mT [Fig. 6.4(a)] and 0 mT (c). The colors within (a), illustrating the distribution of ferroelectric domains, coincide with Fig. 6.1(c). Since the value of 60 mT is within the range of the switching field of β and γ-domains, merely the magnetic signal of those new domains is apparent, which reveals in agreement with the qualitative interpretation of the coupling an easy axis perpendicular to the steps. Although exhibiting a statistical uncertainty, the width of the magnetic domains are quite similar ($\approx 3\mu$m). The lack of contrast of the small green stripe at the right demonstrates a certain value of domain width required for reaching the saturation of stress. The occurrence of such a transition width will be treated analytically in chapter 8. Since the induced stress is smaller, the switching field will also be small. The persistent contrast in the demagnetized state (c) far away from the other two stress domains proves its existence. Because the magnetic field was oscillating parallel to the steps, the magnetization of the old unstressed domains is aligned parallel, too. Therefore, the lack of contrast at the right and left is rather physical than an artifact due to defocusing. Approaching β-domains causes a slight rotation and a formation of uncharged 180° magnetic domain walls, whose frequency of alternation increases to match the arrangement within the β-domains. The physical reason of such domain patterns is the minimization of stray field, originating from charged domain walls, and of anisotropy, which is negligible here.

The corresponding hard magnetic hysteresis of the β-domains is shown in Fig. 6.5(a).

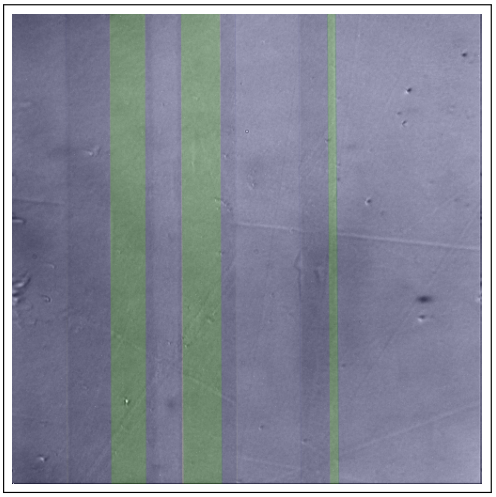

(a)

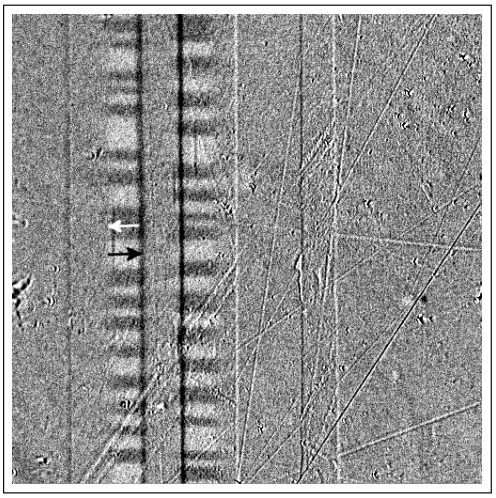

(b)

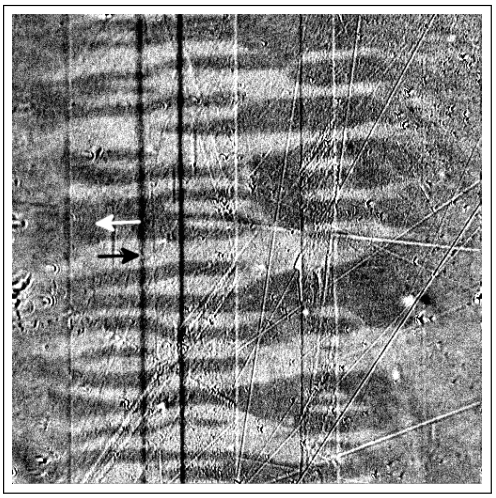

(c)

Fig. 6.4: *Demagnetized states of electrically switched NBFL. The three images (a), (b) and (c) display the distribution of stress domains and the longitudinal demagnetized state, taken during the application of an electric and a magnetic field parallel to the topographical steps of 60 mT and 0 mT, respectively. The arrows indicate the sensitive magnetization components. Due to the lack of any stress within γ-domains the magnetization is aligned parallel to the magnetic field, leading to gray contrast. Above β-domains a significant magnetic anisotropy with an easy axis perpendicular to the steps is induced [see (b)]. (c) At zero field the magnetization within the isotropically stressed regions is aligned with respect to the embedded β-domains for the sake of minimization of the stray field energy.*

It demonstrates the maximum switching field of $(220 \pm 20)\,\mathrm{mT}$, taking the saturation magnetization into account, which can be obtained with this system. A comparison with the intrinsic switching field reveals an increase of two order of magnitude, caused by a decrease of the lattice constant of 5 pm. The generation of a magnetic easy axis within β-domains causes an additional step in the transverse hysteresis, as shown in Fig. 6.5(b). The field value of $(5.7 \pm 0.2)\,\mathrm{mT}$ belongs to the coercivity of β-domains.

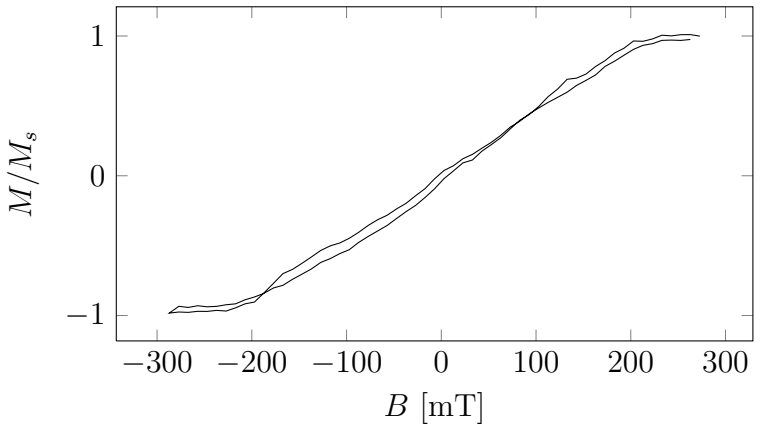

(a)

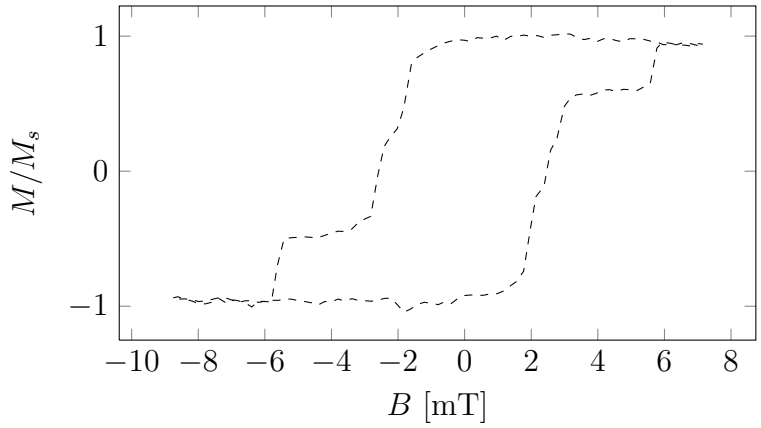

(b)

Fig. 6.5.: *The graph (a) shows the longitudinal magnetic hysteresis of the β-domains of NBFL during the application of an electric field. The significantly increased switching field of $(220 \pm 20)\,mT$ represents the maximum value, achievable with this system. It illustrates the remarkable impact of a change of lattice constants of 5 pm on the magnetic properties of magnetostrictive nickel films. Due to the generation of an easy axis an actual coercivity is induced leading to the second step at $(5.7 \pm 0.2)\,mT$ in the transverse hysteresis (b).*

6.2. High Temperature Deposition

A second way of inducing stress into the nickel film is the deposition on top of paraelectric barium titanate single-crystal. The substrate holder, fixing the substrate, was heated slowly up to 400 °C and kept at this temperature for half an hour to ensure a homogeneous transition into the cubic phase before starting deposition [Fig. 6.6(a)]. At room temperature the substrate becomes tetragonal by forming ferroelectric a and c-domains (b). Due to isotropic displacement of the surface atoms within c-domains, the resulting isotropic stress within the nickel film does not affect the magnetic properties. Therefore, an easy axis is still absent. The advantage of this deposition is the occurrence of highly tensile stressed α-domains after cooling without an external electric field and the unique correlation between ferroelectric and stress domains. Thus, the difference between para- and ferroelectric deposition is the rotation of the magnetic axis by 90 degrees, since now a-domains induce tensile stress.

The transverse demagnetized state of an area of NBPL is shown in Fig. 6.7(b) and Fig. 6.7(d) for a magnetic field of 60 mT and 0 mT, respectively. According to Fig. 6.6(b) small α-domains, exhibiting a longitudinal easy axis, show a large switching field, since

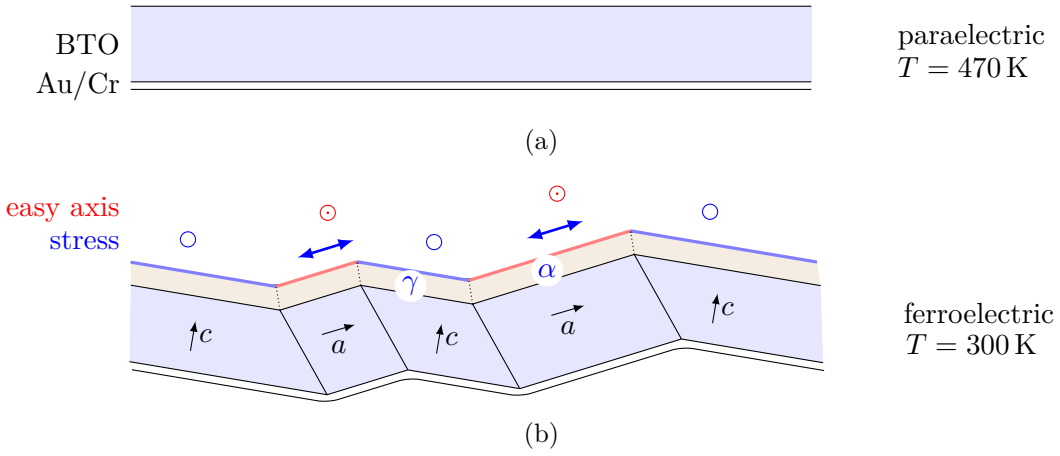

Fig. 6.6.: *(a) Heating the substrate during deposition above its transition temperature results in the attachment of nickel atoms on top of paraelectric barium titanate. (b) At room temperature the crystal becomes ferroelectric by forming a and c-domains. Therefore, tensile stress above a-domains and isotropic stress above c-domains is induced. The corresponding magnetic easy axis is aligned parallel to the topographical steps above a-domains. The in-plane magnetic properties of γ-domains are unaffected. Since the ferroelectric domains coincide with the stress domains, applying an electric field will not change the arrangement qualitatively.*

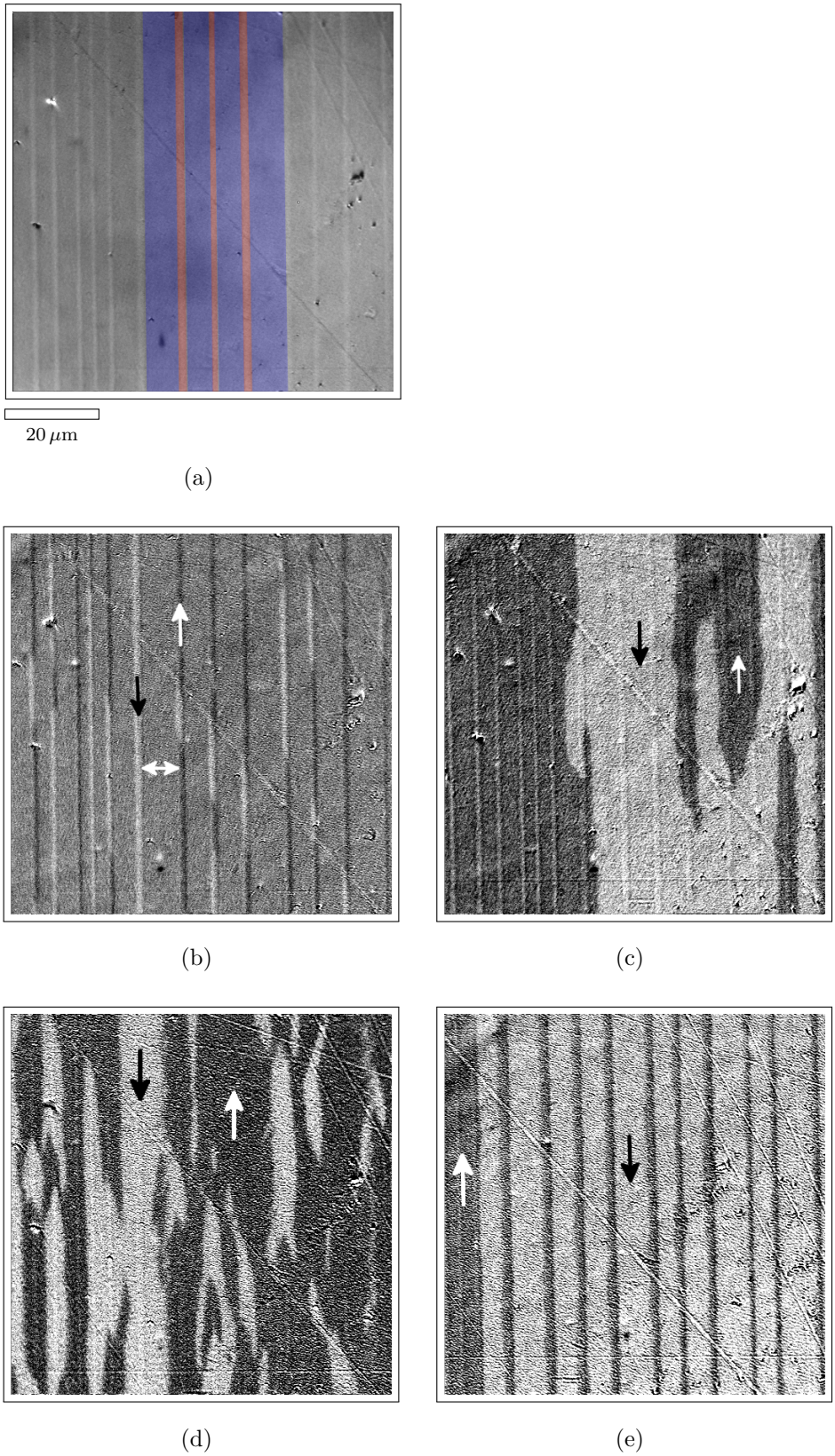

Fig. 6.7.: *Demagnetized states of as-deposited NBPL. (b) and (d) show the transverse demagnetized state within a magnetic field of 60 mT and 0 mT, respectively, of the stress domain distribution (a). At absent field the magnetization of the embedded γ-domains align according to stray field minimization parallel to the steps. (c) displays the longitudinal demagnetized state with quite large magnetic domains. For illustration (e) depicts the delayed transition of α-domains compared to γ-domains during the longitudinal hysteresis at 10 mT, plotted in Fig. 6.8(a).*

the rotation into the easy axis starts early. At absent field the magnetization within the isotropically stressed γ-domains aligns with respect to the magnetization, shown in (b). Since the distances between stress domains are constant and small compared to Fig. 6.4, no gray contrast appears. Hence, only one effective easy axis for the whole system exists.

The magnetic hystereses for both transverse magnetic field and transverse contrast are shown in Fig. 6.8(a) and (b) for γ and α-domains, respectively. The actual magnetic transition of γ-domains is apparent for fields of $(2.5 \pm 0.2)\,\mathrm{mT}$. The additional hard axis

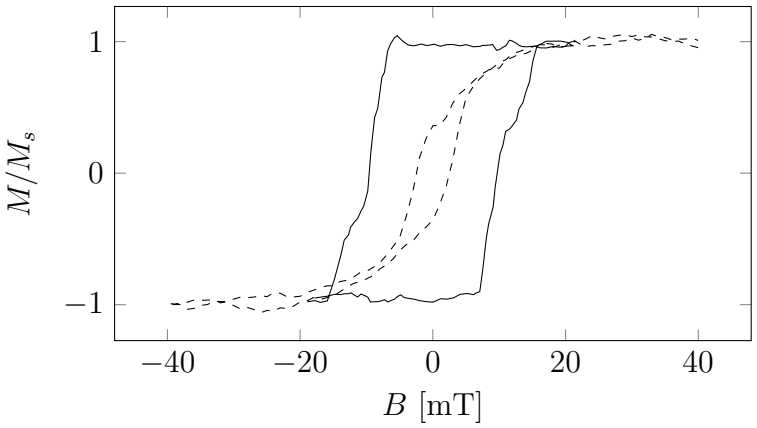

(a)

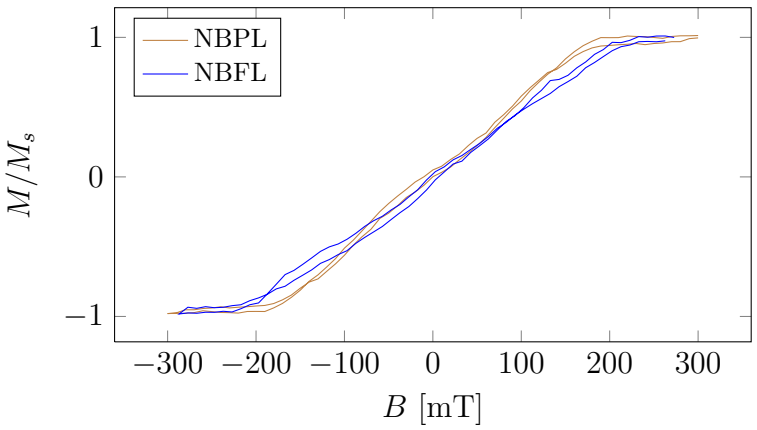

(b)

Fig. 6.8.: *(a) displays the longitudinal (solid) and transverse (dashed) hysteresis of the entire region, shown in Fig. 6.7, and of γ-domains, respectrively. The two kinks within the longitudinal loop represent the flipping of the magnetization vectors of γ and α-domains as a function of the domain width. Due to the favored orientation parallel to the steps, the transverse hysteresis shows a superimposition of two transitions. The first switching field of $(2.5 \pm 0.2)\,mT$ belongs to γ-domains. The larger one originates from the coupling appearing above narrow ferroelectric domains. A comparison (b) between the hard axis hystereses for compressive (NBFL) and tensile (NBPL) stress illustrates the higher effectivity of compression.*

characteristic is caused by the favored alignment parallel to the steps in case of narrow ferroelectric domains for the sake of stray field reduction and domain wall minimization, as can be seen in Fig. 6.7(d). The switching field of the α-domains is very high, namely $(190 \pm 20)\,\mathrm{mT}$. A comparison of the hystereses of both tensile and compressive stress illustrates a higher effectivity for compression. This difference can be assigned to a quasi-paraelectric deposition, leading to a reduced change of lattice constant and, hence, stress, and to a stronger coupling for compression than for tension of negative magnetostrictive media. Although tensile stress favors according to (2.2.9) an easy plane perpendicular to the stress direction, the dimensions of the thin film, generating a large shape anisotropy, restrict the easy plane to an easy axis, confined to the surface plane. As a result the magnitude of parallel and perpendicular magnetostriction constants should be similar.

Fig. 6.7(c) and (e) show the longitudinal demagnetized state and a shot of the longitudinal hysteresis, shown in Fig. 6.8(a), respectively. Since the magnetic field was oscillating parallel to the easy axis, the generated magnetic domains are much larger. In fact, this shot represents the most balanced equilibrium state. Because of the very small width of α-domains their magnetization will flip at a relative large field of $(14.5 \pm 0.3)\,\mathrm{mT}$, demonstrating the influence of boundaries. The actual switching process was modeled with the aid of Nmag [FF10], a hybrid finite element/ boundary element method, which solves the micromagnetic equation (see 2.2). As a result, the magnetization does not flip by 180 degrees. Instead, an almost step-like rotation occurs, which is suppressed for small narrow stripes due to a large stray field contribution. The transition at lower fields belongs to γ-domains exhibiting a rather linear dependence with negative slope of the coercivity on the domain width.

The definite verification of paraelectric or quasi-paraelectric deposition was done by applying an electric field to the sample. Fig. 6.9 displays the distribution of ferroelectric domains and the longitudinal demagnetized state of an area, which showed an arrangement, similar to Fig. 6.7, before switching. The advantage of this area is the occurrence of the tail of an a-domain located almost in the center, whose width of less than 1μm still causes sufficient stress. Since (b), taken at 10 mT, shows transverse magnetic contrast above former a-domains, the deposition was proceeded on almost paraelectric barium titanate. Because the sample was fixed with glue to the substrate holder, its bad thermal conductivity could have suppressed a complete phase transition. According to the longitudinal hysteresis (solid line in Fig. 6.10), the switching field is $(25 \pm 2)\,\mathrm{mT}$. Adding this value to 190 mT of the α-domains leads to the similar magnitude of induced stress within NBFL and NBPL. Although an entire inversion, at least with this sample, could not be observed, the derived possibility of modifying the value of the switching fields is

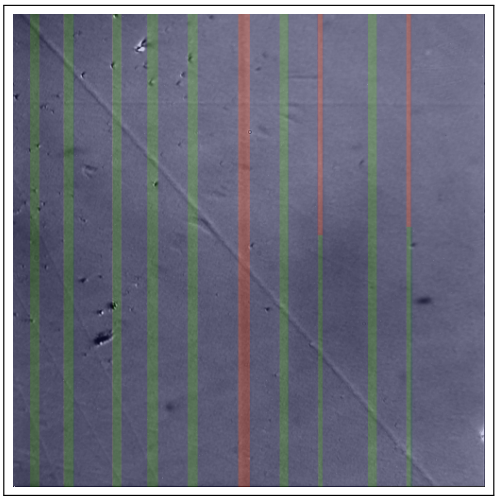

(a)

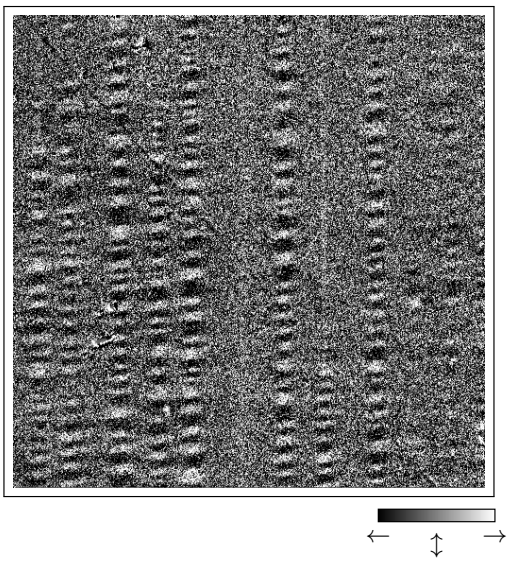

(b)

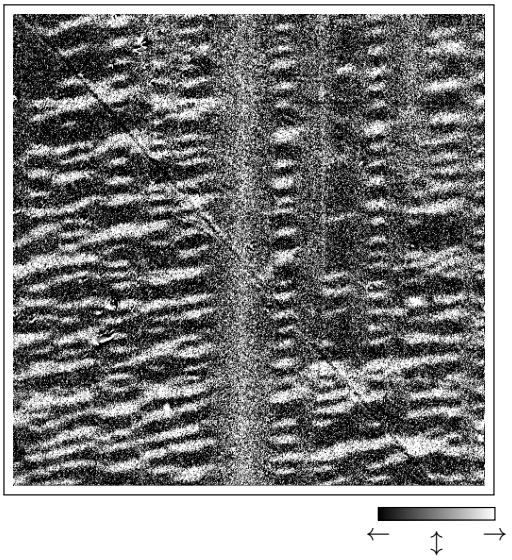

(c)

Fig. 6.9: *Demagnetized states of electrically switched NBPL. The distribution of stress domains (a) and the longitudinal demagnetized state at 10 mT (b) and zero field (c) were taken during the application of an electric field. Apparently, new c-domains induce an easy axis perpendicular to the steps, referring to quasi-paraelectric deposition. At zero field the magnetization vectors align appropriately to avoid charged domain walls. The weaker contrast within few β-domains is due to their small width.*

of much more interest. Comparing the width of both former a-domains and transverse magnetic contrast gives an impression of a continuous transition of the stress distribution within the film, as will be discussed in chapter 8. At zero field most of the magnetization vectors within γ-domains align transversely. However, there are few stripes, which show weaker contrast, suggesting a component parallel to steps and oscillated field. Since the longitudinal switching field of the γ-domains matches with the value of 2.5 mT for transverse hystereses, as can be seen in Fig. 6.10, the induced stress is isotropic and the weaker contrast does not imply an easy axis parallel to the steps. The actual reason is the small width of stress domains and the small switching field favoring slight tilts within γ-domains to minimize magnetic charges.

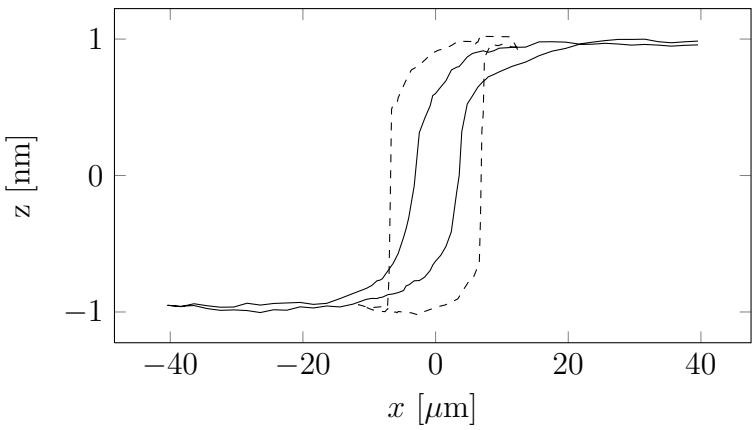

Fig. 6.10.: *The two curves display longitudinal (solid) and transverse (dashed) hysteresis of the magnetic domains, located above new and old c-domains. Since the longitudinal switching field does not vanish, the nickel was deposited on top of quasi-paraelectric BTO. Hence, a tuning of both lattice constants at the surface and induced stress should be possible. The β-domains exhibits a coercivity field of $(6.8 \pm 0.3)\,mT$, whereas the stress within γ-domains is isotropic.*

6.3. Intermediate Deposition

As could be shown in 6.1 and 6.2, the orientation of the induced magnetic easy axis can be set according to the deposition conditions, since the lattice constants of the substrate differ for different temperatures. The extremal cases of stress-free and paraelectric deposition exhibit only one effective easy axis, leading to continuous transitions. In principle, it should be possible to superimpose both cases by using both high deposition rate and high environmental temperature. An increase of the temperature, starting at room temperature, by 100 K results in a thermal expansion of the unit cell of 0.15% for a and 0.06% for c-domains [Sur11], which are roughly 10% of the change due to phase transition at 120 °C. Consequently, small tensile stress above a-domains should be continuously tunable. However, larger stresses can only be obtained by using high deposition rates. Because the distribution of the kinetic energy of nickel atoms during deposition is retained for different rates, merely the amount of heat transfer varies. An appropriate rate and environmental temperature can, therefore, cause a significant expansion of the unit cell at the surface. Due to finite heat capacity (0.527 J/gK) and thermal conductivity (6 W/mK* [Sur11]) the bulk will not be affected, though, leading to a displacement and temperature gradient. Since the magnitude of both gradients can be tuned by setting different environmental temperatures, for instance, by heating the substrate holder, the depth and, hence, the lattice constants at the surface can be set in spite of the discrete values for para- and ferroelectric phases even for large expansions, as it was apparently the case in 6.2.

Since the lattice constants differ during deposition from the room temperature values, tensile stress is induced above a-domains [see Fig. 6.11(b)]. The corresponding switching field will be much smaller compared to (quasi-)paraelectric deposition. Because the energy contribution of domain walls depends on the anisotropy, as will be discussed in 7.2, the contrast within demagnetized α-domains is not strictly uniform [see Fig. 6.12(b)]. This domain structure illustrates the influence of both high rate and high temperature on the lattice constants, since relaxation, as will be discussed later, can be excluded due to the age of the sample of few days. Moreover, the rather poor thermal conductivity seems to affect both domain structure and switching field. Contrary to the extremal cases intermediate deposition causes a broad distribution of α-domain switching fields. In our case these fields were in the range of 60 to 150 mT for different intermediate samples. Intermediate samples exhibit by definition all three stress domains due to deposition or aging. As usually, the induced isotropic stress above c-domains does not lead to a remarkable anisotropy and

*For comparison, copper and quartz exhibit a thermal conductivity of 400 W/mK [efu11] and 1.3 W/mK, respectively.

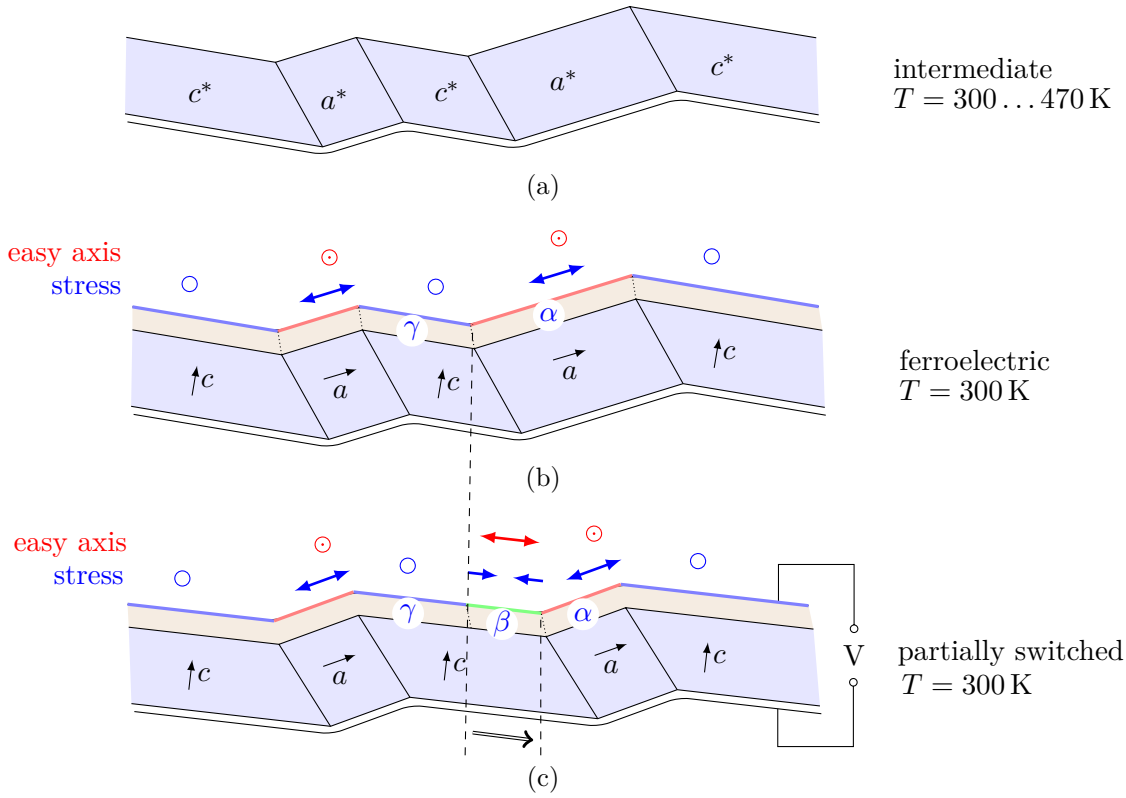

Fig. 6.11.: *(a) High deposition rate and appropriate environmental temperature cause a significant change of the room temperature lattice constants at the surface of the substrate. The tetragonal symmetry should be conserved, though. (b) According to these parameters the stress above ferroelectric a-domains and inside the nickel film varies. (c) Because the lattice constants did not match with either paraelectric nor ferroelectric values during deposition, new c-domains will induce compressive stress and a magnetic easy axis perpendicular to the topographical steps.*

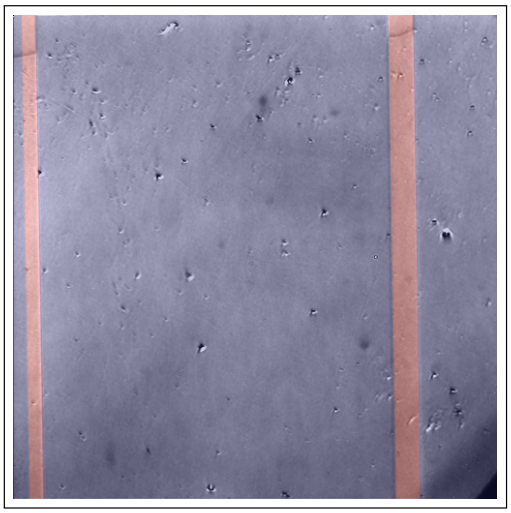

(a)

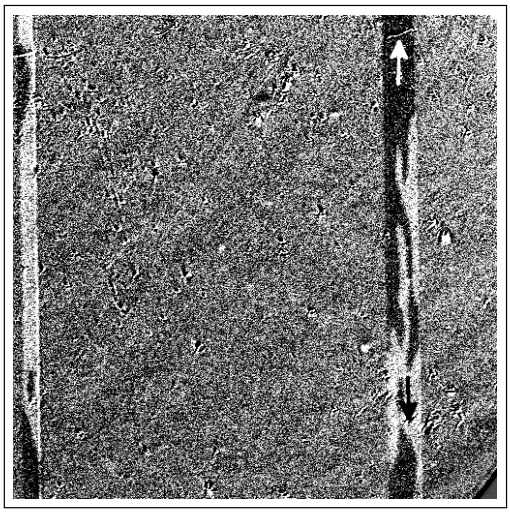

(b)

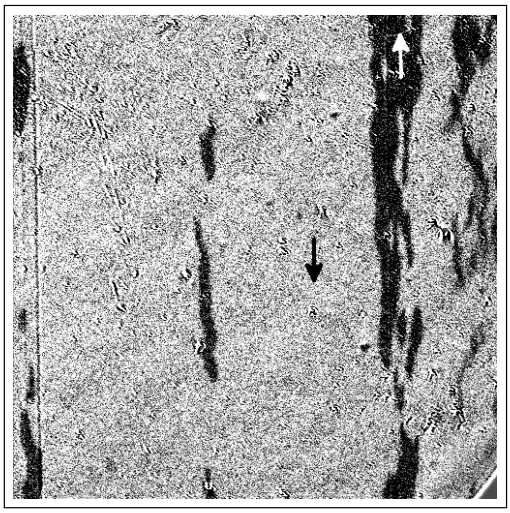

(c)

Fig. 6.12: *Demagnetized states of NBFH. Ferroelectric domain distribution (a) and transverse demagnetized state at 10 mT (b) and 0 mT (c) of NBFH are displayed. The high rate induces moderate tensile stress into a-domains favoring longitudinal alignment. Since the sample was prepared few days before, aging can be excluded, illustrating the pure influence of deposition.*

switching field. Accordingly, the value of (2.5 ± 0.3) mT can be assigned to both coercivity and switching field. Since the slope of the hysteresis is similar to Fig. 6.3 and, thus, does not reveal anything new, the graph is not shown here.

The application of an electric field for the sake of increasing the *c*-domains density leads, as shown in Fig. 6.11(c), to a second effective stress domain with an easy axis perpendicular to the topographical steps, preferring an abrupt transition. The corresponding magnetic domain patterns are shown in Fig. 6.13. In spite of the lack of far ordering, such as crystal structures, a remarkable induction of localized stress is observed. Because this area covers all three types of stress domains and does not show any normal magnetization components [see (d)], samples of this type and dimensions are expected to exhibit magnetic easy axes, which is confined to the surface plane. (b) and (c) represent the longitudinal and transverse magnetization components, respectively, of the same longitudinal demagnetized state. This could be achieved by demagnetizing and detecting the longitudinal contrast as usually. Afterwards the polarization of light was changed to p-polarization. Setting the entire signal as background image and applying an oscillating magnetic field reveals the transverse MOKE signal. Since p-polarized light is less sensitive, cross-talk is likely to occur. The most distinct feature of (c) are certainly the branching-like domain patterns, characteristic for the cross-section of out-of-plane easy axis materials, such as CoFe. An elucidate discussion on the branching feature is given in 7.1. Because of the stray field generated by broad magnetic domains above the new *c*-domains, an inversion of the contrast in (b) occurs to guarantee flux-closure.

According to 6.1 and 6.2 the sum of the stresses and switching fields of α and β-domains is in the same range. Since the intermediate deposition causes a switching field in between, the corresponding fields of β-domains will also differ from the minimal and maximal value. Fig. 6.14(a) shows the hard axis hystereses of α and β-domains of several intermediate samples. Apparently, the switching fields are similar. Please notice, that only the black curves obey the summation, since the other were taken at different areas, illustrating the largest values, which could be obtained by these samples. Furthermore, a general statement on summation is not possible due to varying volume density (see 6.7), affecting saturation magnetization and magnetostriction constant and elastic coefficients.

Another parameter is the age of the stress domains, since a relaxation occurs. As apparent in Fig. 6.14(b), the switching field of the β-domain differs from the value of old β-domains, switched several months before. Differences due to thermal conductivity can be excluded, since both hystereses were measured few micrometers away from each other. Because the width of the β-domains is roughly $10\,\mu$m, the measured field represents the actual value, unaffected by boundary effects. Due to the lack of any crystalline arrange-

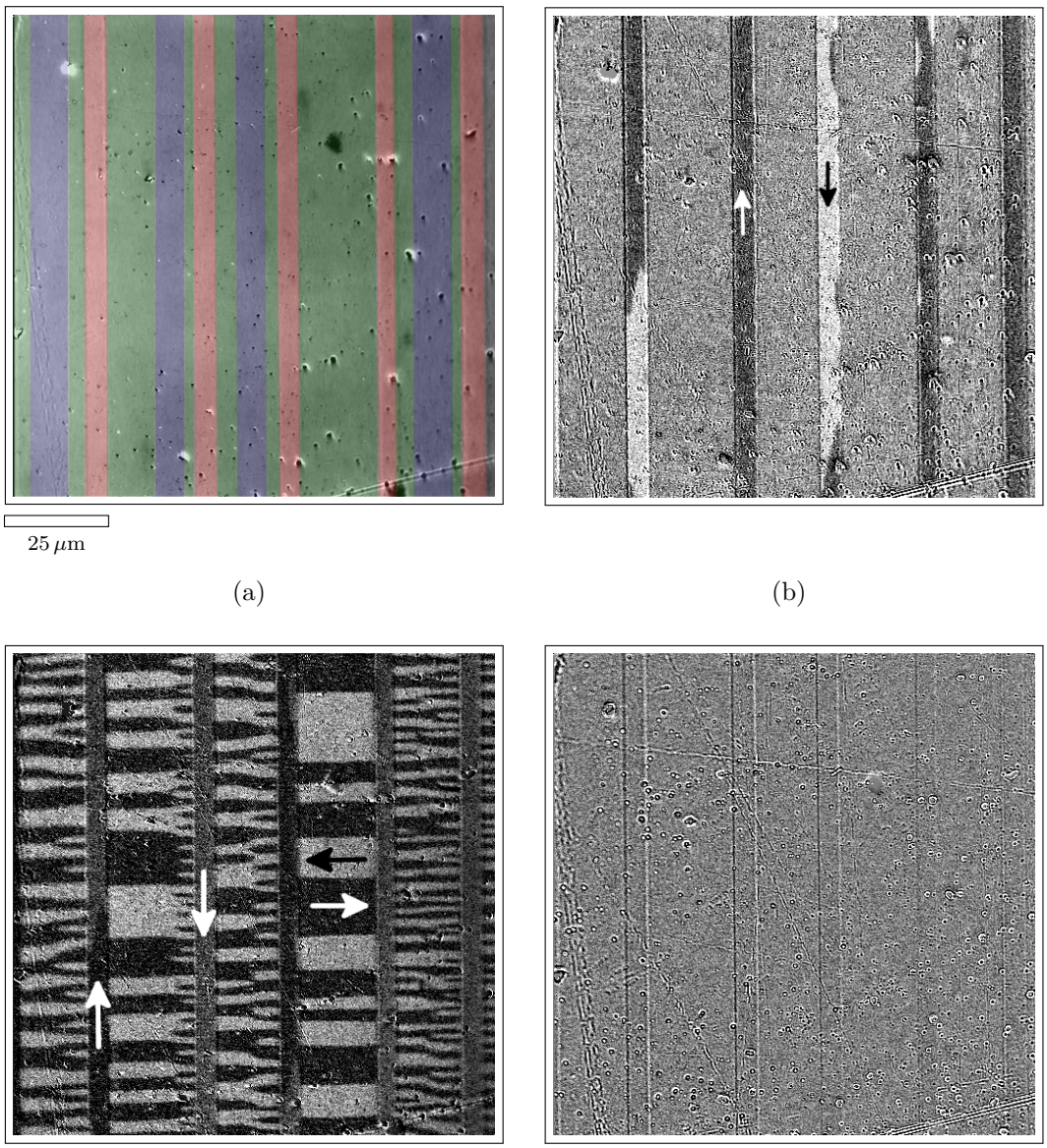

Fig. 6.13.: *Demagnetized states of electrically switched NB100. The images (a) - (d) depict the ferroelectric domain distribution, the transverse and the longitudinal contrast of the longitudinal demagnetized state and the polar MOKE contrast of NB100, respectively. Due to high rate and proceeded age old and new c-domains induce different magnitude of stress and anisotropy, leading to branching-like domain patterns apparent in (c). Due to broad magnetic domains, located above new c-domains, flux-closure domains are formed within α-domains [see (b)]. For completeness, the out-of-plane contrast is shown in (d), revealing entirely in-plane magnetized domains.*

ment it is likely, that the atoms will adjust their interatomic distances to minimize the elastic energy, reducing thereby stress and switching field. Consequently, even the two cases, discussed in the previous sections, should show in time two effective stress domains. Although compressive and tensile stress perpendicular to the topographical steps alternate by applying an electric field, the compression along the steps can not be refreshed, demonstrating irreversible aging of the nickel film.

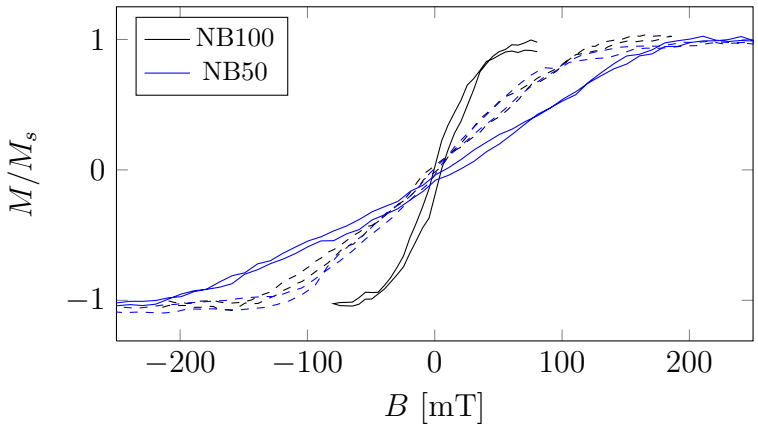

(a)

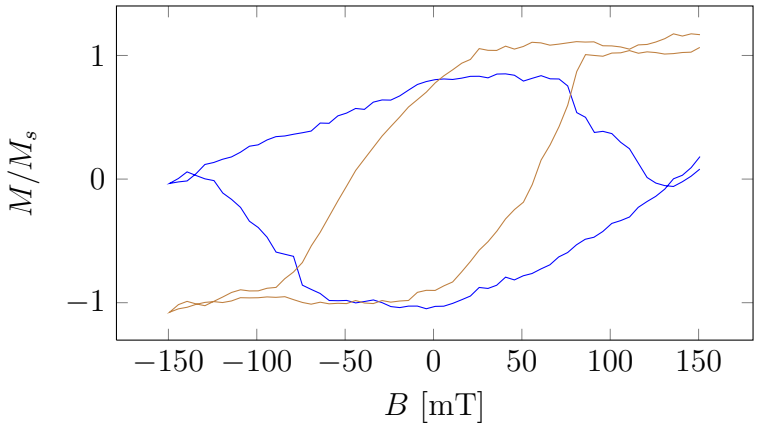

(b)

Fig. 6.14.: *(a) shows few hard axis hystereses of α (dashed) and β-domains (solid) of NB100 (black) and NB50 (blue). Since the saturation magnetizations of both samples are similar, switching fields of the same value should be expected. However, due to aging and inhomogeneous heating of the substrate, the values can differ for different areas and samples. To illustrate the aging effect, (b) shows the transverse contrast during a longitudinal magnetic hysteresis for new (blue) and rather old β-domains (brown). The corresponding switching fields are 130 mT and 85 mT, respectively.*

6.4. a_1/a_2-Domain Patterns

The correlation between ferroelectric and stress domains allows a pre-structuring of the substrate either by writing c-domains via conductive AFM into a-domains or by applying stress to the substrate, which affects the period of alternation. Here, we will focus on deposition on a_1/a_2-domain patterns, since the corresponding features distinguish from the usual domain structures.

Fig. 6.15 shows transverse and longitudinal MOKE signal of the same longitudinal demagnetized state, located above a large new c-domain, partially divided by small a-domains, as apparent by distinct contrast in (b) and the topographical cross-talk in (a). Obviously, the area of perpendicular easy axis is much larger than of parallel one. To avoid charged domain walls the magnetization vectors are aligned properly, leading to an almost inverted contrast. Since the stripes of magnetic contrast appear always at the same location, the observed patterns are imprinted and display no randomized distribution. As discussed in 5.2.1, the existence of a_1/a_2-domains is not restricted to epitaxial films, but was observed by 3 of 8 single-crystals. Taking their occurrence into account, magnetic domain structures, as shown in Fig. 6.15, can be explained. Accordingly, a_1-domains, exhibiting a transverse expansion, are more favored than a_2-domains due to the match of the lattice constant. Consequently, β-domains show two different easy axes with a major axis perpendicular to the steps. The switching fields of both orientations are similar, as expected. Due to aging their values will differ, though.

Within small β-domains the existence of two easy axes affects the switching behavior, since charged domain walls are formed during the hysteresis. Thus, demagnetized states will exhibit a rather uniform magnetization.

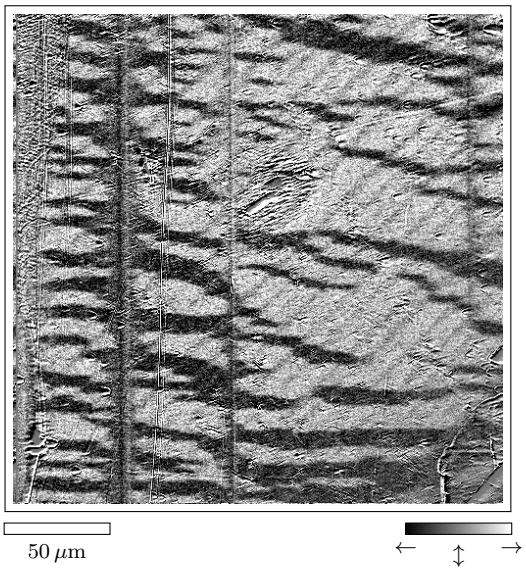

(a)

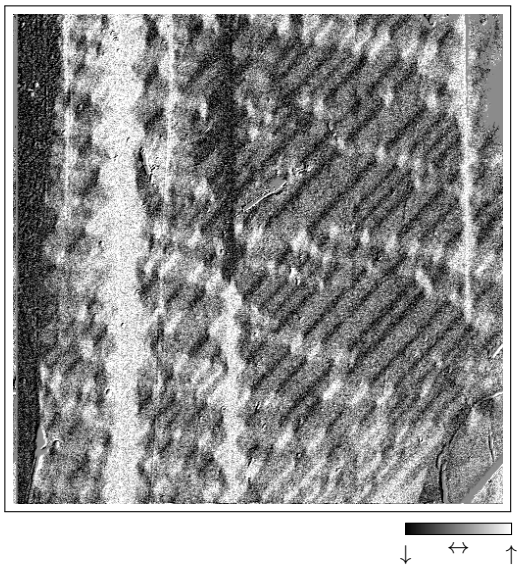

(b)

Fig. 6.15.: *The two images show the transverse and longitudinal magnetization components of the same longitudinal demagnetized state of a β-domain, partially divided by small α-domains. The distinct difference of two easy axes above one ferroelectric domain is due to the deposition on a_1/a_2-domain patterns, leading afterwards to compressive stress parallel and perpendicular to the topographical steps. Due to the avoidance of charged domain walls the contrast of both images is almost inverted.*

6.5. Parallel and Perpendicular Easy Axes

Within this section a method to determine precisely the orientation of the easy axis is presented. Although both contrast of magnetic domains and corresponding domain walls (see for instance Fig. 6.13) suggest an alignment of the easy axes of a and c-domains parallel and perpendicular to the steps, respectively, the final verification was done with the aid of magnetic hystereses.

For this purpose the magnetic field was applied and tuned perpendicularly to the assumed easy axis, while detecting the complementary in-plane magnetization component. Fig. 6.16(a) compares the common hard axis hysteresis, similar to a sinusoidal shape of rotation [see Fig. 2.2], with that loop. The switching fields are equal, although the solid graph allows a more accurate determination. Additionally, the magnetization components can be observed during switching, offering a very sensitive way to measure the orientation of the easy axis, as shown in (b). Since the magnetization is confined to the surface plane, the component along the easy axis can be obtained from (2.2.12). However, because of the size of the sample non-uniform rotation takes place, exhibiting a smaller average signal. According to Nmag the symmetry will retain, though. If the magnetic field is aligned precisely perpendicularly to the easy axis, the hysteresis will show a continuous transition. Small deviation from the alignment causes an additional flip of the magnetization, apparent as a jump in the hystereses. The discontinuity is suppressed in the common hard axis hysteresis, though.

Consequently, this kind of hysteresis could verify a perfectly parallel and perpendicular alignment of the easy axis for tensile and compressive stress within α and β-domains, respectively.

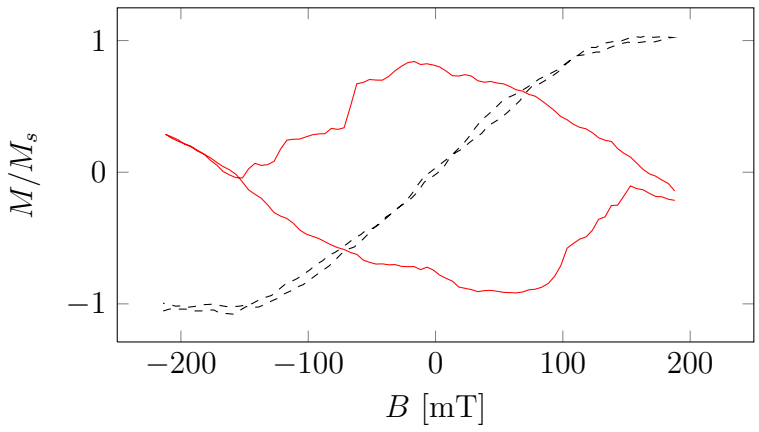

(a)

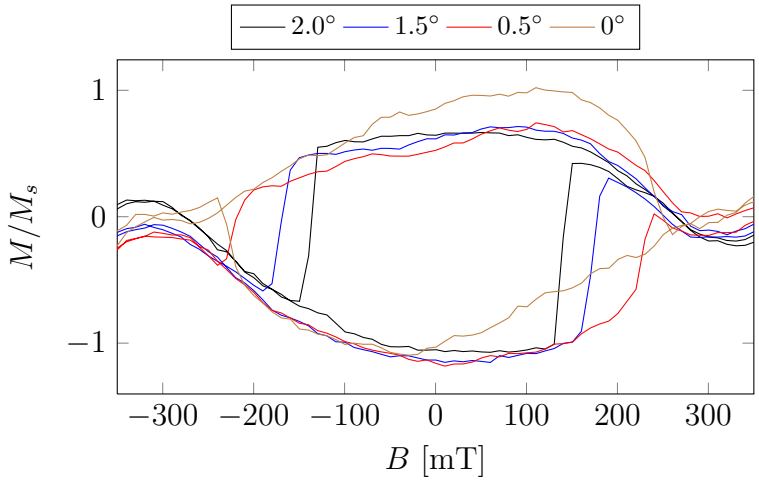

(b)

Fig. 6.16.: *Common hard axis hysteresis (dashed) and corresponding complementary magnetization component (solid) are shown in (a). Since the rotation is confined to the surface plane, both switching fields coincide. (b) The observation of the component parallel to the easy axis allows a more sensitive determination of the orientation, though.*

6.6. Integral SQUID hystereses

In 6.1 – 6.3 the switching fields of several samples and magnetic domain structures have been measured. Although their value is relevant for any magnetic treatment, the knowledge of the magnetic anisotropy would be of more interest for physical reasons. For this purpose integral magnetic hystereses were measured with the aid of a SQUID magnetometer, allowing the determination of the saturation magnetization. Moreover, since SQUID is volume sensitive, the acquired hystereses contain informations of the whole system. Therefore, it is an alternative to MOKE, which can be used to determine the field values by a second technique.

6.6.1. Influences of Deposition Conditions

Following the order of Tab. 4.1, we first focus on stress-free NBFL and NBPL. Both Ni films were sputtered at very low rate but different substrate temperatures, namely 300 K and 470 K. Since both samples have been neither thermal nor electrically treated between deposition and SQUID measurement, states and properties, extracted from the hystereses, can be assigned directly to the deposition conditions. The corresponding hystereses are shown in Fig. 6.17. The brown curve belongs to NBFL, whose lattice constants were not affected remarkably during deposition, as verified by MOKE imaging (see 6.1). Therefore, the induced stress is rather negligible leading to a small switching field and one uniform transition. The non-vanishing anisotropy is due to the intrinsic coupling within amorphous glasses [see FEF+89]. With the aid of the saturation magnetization [(300 ± 42) kA/m], the corresponding switching field of (8.0 ± 1.0) mT can be converted into the anisotropy of (1.2 ± 0.3) kJ/m^3, which represents a typical value for amorphous glasses. For comparison, polycrystalline ferromagnets exhibit an anisotropy of ≈ 500 J/m^3, whereas the crystal anisotropy is many orders higher [HS09]. The two coercivities of -1 mT and 1.7 mT demonstrate the dependence of the field correction on the discretization, mentioned in 3.3.2. The actual coercivity is the mean value of both, since no physical reason would verify an asymmetry. Besides these values the hysteresis shows a curvature at much larger fields, namely (220 ± 20) mT. Although no external fields were intentionally applied, the slightest pressure, for instance, during attachment causes locally a transition into new c or a-domains, whose existence leads to those large switching fields.

The blue lines represent the hystereses of NBPL, whose substrate holder was heated up to 470 K during deposition. Since this value is much higher than the transition temperature of barium titanate, it was supposed to deposit Ni on the paraelectric phase. Although this treatment had a significant influence on the lattice constants, the crystal did not become

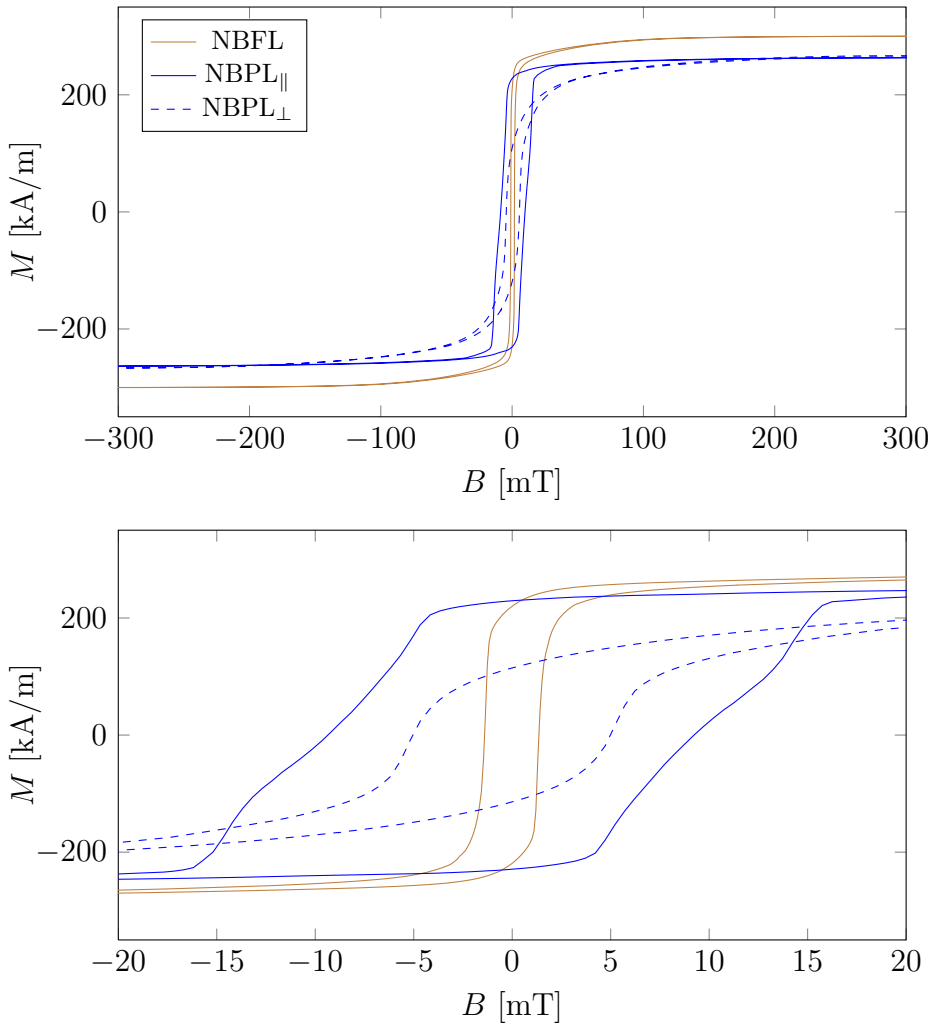

Fig. 6.17.: *The three graphs show the SQUID hystereses of stress-free NBFL and of the quasi-paraelectric NBPL for different ranges. The influence of the temperature during deposition is represented by single and two phase transition. With the saturation magnetizations of NBFL and NBPL of* $(300 \pm 42)\ kA/m$ *and* $(265 \pm 37)\ kA/m$*, respectively, the anisotropies can be determined to be* $(1.2 \pm 0.3)\ kJ/m^3$ *and* $(30.5 \pm 6.7)\ kJ/m^3$ *(α-domain).*

entirely paraelectric, as was shown in 6.2. Because the displacement induces stress domains, the orientation of the sample with respect to the magnetic field becomes important, which was not the case for NBFL. Therefore, hystereses of parallel (solid) and perpendicular (dashed) alignment of the topographical steps with respect to the magnetic field and sensitive axis were measured. As a result, the dashed curve reveals coercivity of γ-domains* and switching fields/ anisotropy of α-domain. One notice the much larger switching field of α-domains of $(230 \pm 20)\,\mathrm{mT}$, corresponding to an anisotropy of $(30.5 \pm 6.7)\,\mathrm{kJ/m^3}$. The increased error of switching fields with increasing fields is due to their flattening. The coercivity of γ-domains can be estimated to be $(8.5 \pm 1.0)\,\mathrm{mT}$. The parallel hysteresis, also known as longitudinal, can not be analyzed without the knowledge obtained by MOKE imaging. In the hysteresis two kinks appear, which can be assigned to coercivity and anisotropy of each domain type, since merely two stress domains should exist. Here, the smaller value belongs to the hard axis transition of γ-domains with switching field of $(8.0 \pm 1.0)\,\mathrm{mT}$, which coincides with both coercivity and switching field of stress-free NBFL. Consequently, the induced stress is truly isotropic. The larger value of $(14.5 \pm 2.0)\,\mathrm{mT}$ represents the width dependent coercivities of α-domains, which show a rather continuous transition.

Fig. 6.18 shows longitudinal and transverse SQUID hystereses of NBFH, which was prepared at room temperature with a sputter rate 10 times larger than for NBFL and NBPL. For comparison, NBFL is plotted as well. According to 6.3 a distinct change of the lattice constants from their room temperature values occurs, leading to intermediate values during deposition. Consequently, the hystereses of as-deposited NBFH should look similar to those of NBPL but with smaller switching fields. As before, solid and dashed curves belong to parallel and perpendicular alignment, respectively. Apparently, the solid hysteresis shows a much harder switching behavior than the dashed one, which can be assigned to the larger change of lattice constant within a-domains due to the larger transverse anisotropy. Since the displacement above c-domains is due to the symmetry isotropic, the resulting magnetic anisotropy is zero. According to switching field and anisotropy of α-domains of $(100 \pm 20)\,\mathrm{mT}$ and $(14.0 \pm 3.1)\,\mathrm{kJ/m^3}$, respectively, the effect is approximately half as large as for heating the substrate holder up to 470 K. The saturation magnetization is $(280 \pm 39)\,\mathrm{kA/m}$. Contrary to NBPL, NBFH and all following samples show anisotropies larger than the corresponding coercivities. The coercivity of both α and γ-domains are simultaneously $(1.7 \pm 0.5), \mathrm{mT}$, which is slightly larger than for NBFL.

*Although isotropically stressed γ-domains do not show an easy axis, coercivity and switching field are assigned, according to the orientation in β-domains.

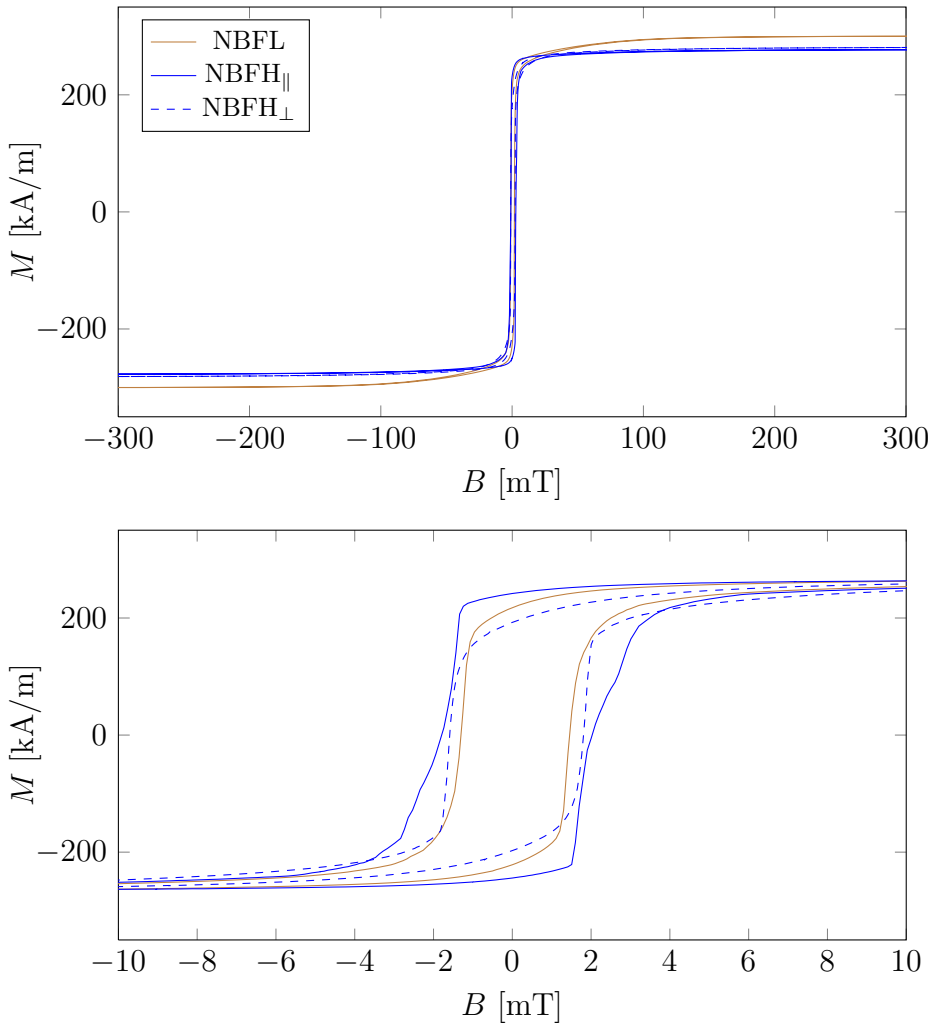

Fig. 6.18.: *The graphs show the SQUID hystereses of NBFH and, for comparison, NBFL. Solid and dashed lines correspond to parallel and perpendicular alignment of the steps with respect to the magnetic field. The saturation magnetization was determined to be* $(280 \pm 39)\,kA/m$*, while the anisotropy of* α*-domains is* $(14.0 \pm 3.1)\,kJ/m^3$*. An improved heat transfer causes a change of the lattice constants, as apparent by different shapes of hysteresis.*

6.6.2. Applying an Electric Field

In the following the SQUID hystereses of the remaining samples NB20, NB50 and NB100, prepared with EBVD, are shown. Since they had been already investigated and electrically switched before measuring with SQUID, additional kinks, illustrating new coercivity and larger switching fields, are expected to appear. Fig. 6.19 displays the magnetic switching behavior of NB20 and NBFH, already discussed above. Apparently, both longitudinal hystereses exhibit a large step for the same small value of coercivity. Since the coercivity depends both on the width of the ferroelectric domains and on the saturation magnetization, which will differ, this coincidence is rather unfortunate. Although there are, if not entirely saturated, favored areas for renucleation after switching off the electric field, namely the former ones, new both a and c-domains, causing much larger magnetic anisotropy, are created. The relative amount can be determined by the ratio of the height of the kinks. The resulting ratio of all four domains is 1:1:1:1, at least in this case. With the aid of the saturation magnetization of $(254 \pm 36)\,\mathrm{kA/m}$ switching field and anisotropy are $(200\pm20)\,\mathrm{mT}$ and $(25.4\pm5.6)\,\mathrm{kJ/m^3}$ of α-domains, and $(260\pm20)\,\mathrm{mT}$ and $(33.0\pm7.3)\,\mathrm{kJ/m^3}$ of β-domains, respectively. Due to the large amount of old domains, their transition is still apparent within the hystereses at very small fields. Comparing the value of 1.5 mT with those of NBFL and NBFH and considering the saturation magnetization shows good agreement. The additional kinks within the hystereses at $(5.2\pm1.0)\,\mathrm{mT}$ and $(6.0\pm1.0)\,\mathrm{mT}$ can be assigned to coercivities of α and β-domains, respectively.

The values of both saturation magnetization and switching fields of the last two samples, NB50 and NB100, shown here, will be smaller due to their age. As already discussed in the previous section, a relaxation of the induced stress within the nickel film occurs in time. Since the thickness of the film is reduced during each cleaning, the determined volume is, particularly for NB100, too large*. However, for any calculation the values, measured by S. Geprägs at the WMI Garching right after deposition, are used, which were also measured for NB20. Because these samples were exposed to an electric field many times before, sophisticated hystereses, as shown in Fig. 6.20, are likely to occur. At least, the shape of the longitudinal hysteresis of NB50 within the range of -20 to 20 mT is similar to those of NBPL and NBFH. The corresponding values of $(4.9\pm0.5)\,\mathrm{mT}$ and $(7.5\pm1.0)\,\mathrm{mT}$ belong to the width-dependent coercivity of β-domains and to the anisotropy of old α-domains, which either have not changed their lattice constant yet or did it long time ago. With a saturation magnetization of $(255\pm36)\,\mathrm{kA/m}$ the anisotropy of β-domains becomes

*The calculated saturation magnetization of NB100 was half the actual value. Since neither X-ray Photoelectron Spectroscopy nor magnetic hystereses reveal any difference at all, antiferromagnetism due to oxidization of Ni can be excluded.

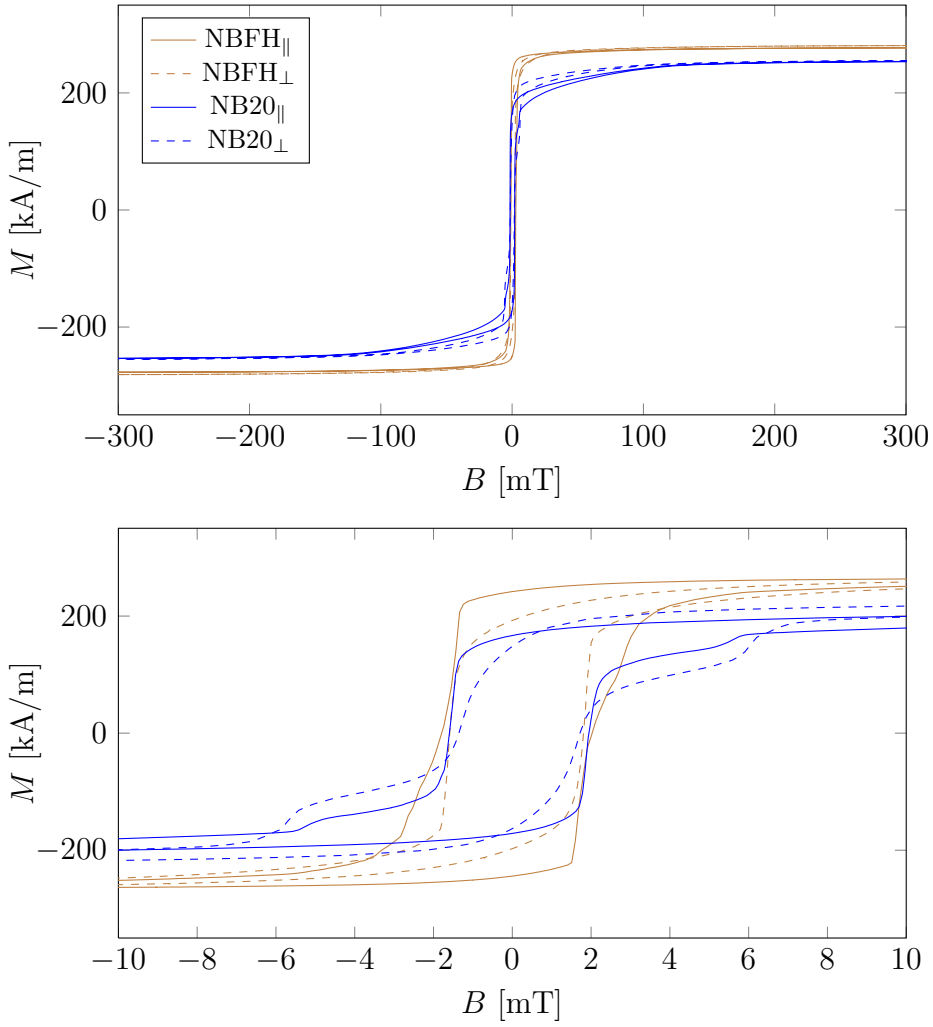

Fig. 6.19.: *SQUID hystereses of NB20 and, for comparison, NBFH are plotted to illustrate the differences after applying an electric field and forming new a and new c-domains, apparent by much larger switching fields and additional coercivities. The saturation magnetization is* $(254\pm36)\,kA/m$*; Anisotropy of* α *and* β*-domains are* $(25.4\pm 5.6)kJ/m^3$ *and* $(33.0\pm7.3)\,kJ/m^3$*, respectively.*

$(15.3 \pm 3.5)\,\mathrm{kJ/m^3}$. This value is, as expected, much smaller than for NB20. Because SQUID is volume sensitive, this circumstance can not be assigned to thickness dependence. The two kinks in the transverse hysteresis (left) originate from α-domains, located either above former ferroelectric a_1/a_2-domain patterns or c-domains. Both switching field and anisotropy of the first case are $(180 \pm 20)\,\mathrm{mT}$ and $(23.0 \pm 5.0)\,\mathrm{kJ/m^3}$, respectively. Consequently, the current state of NB50 consists mainly of new α-domains, exhibiting a larger anisotropy than β-domains.

Since NB100 were switched much more frequently, leading to various magnitudes of stress and switching fields, even more kinks within the transverse hysteresis are apparent. Every kink could be observed by MOKE imaging as well, allowing the assignment of $(3.4 \pm 0.5)\,\mathrm{mT}$ and $(8.0 \pm 1.0)\,\mathrm{mT}$ to coercivity fields of β-domains and of $(14.0 \pm 2.0)\,\mathrm{mT}$ to the anisotropy of $(1.7 \pm 0.4)\,\mathrm{kJ/m^3}$ of β-domains, located above a_1/a_2-domain patterns. The switching field and anisotropy of α-domains are $(130 \pm 20)\,\mathrm{mT}$ and $(15.9 \pm 3.5)\,\mathrm{kJ/m^3}$, respectively. Moreover, β-domains can be switched by magnetic fields of $(210 \pm 20)\,\mathrm{mT}$, which is equal to an anisotropy of $(25.7 \pm 6.2)\,\mathrm{kJ/m^3}$.

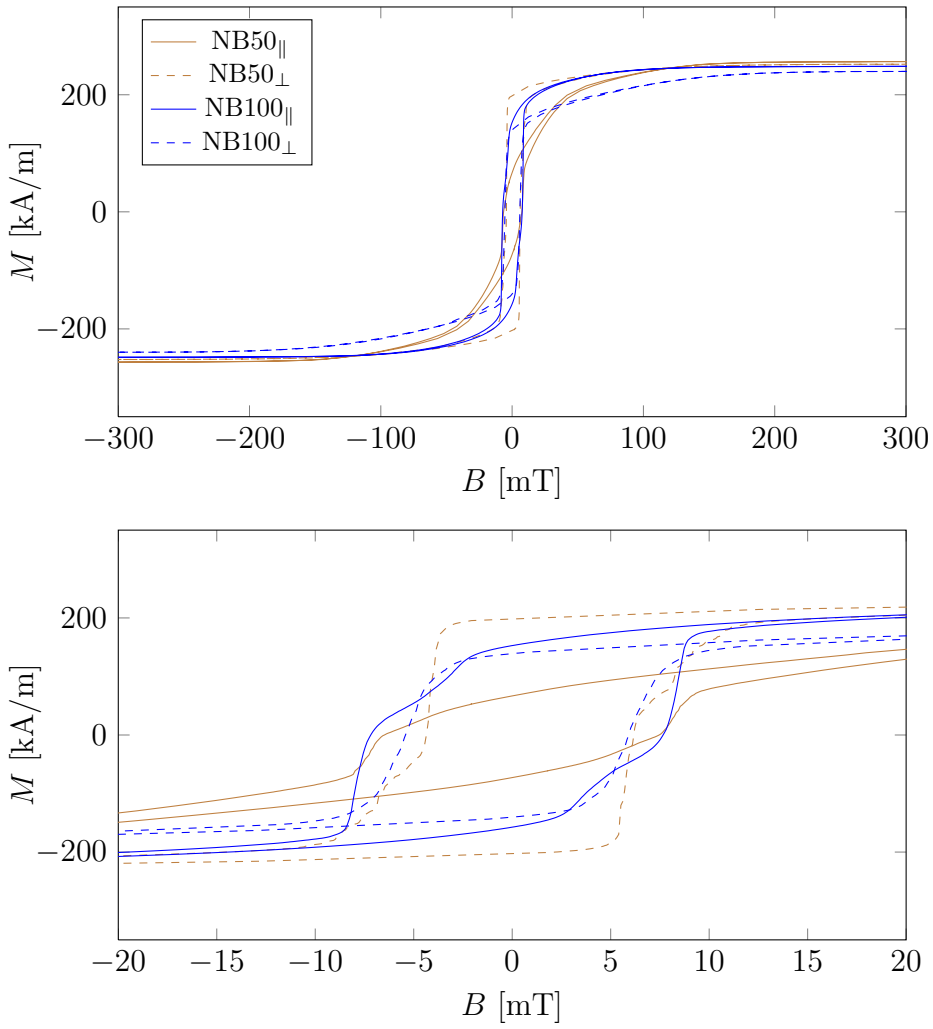

Fig. 6.20.: *The graphs show the SQUID hystereses of NB100 and NB50 after proceeding several electric loops. Due to the occurrence of a_1/a_2-domain patterns and randomly distributed nuclei the hystereses exhibit many features. The actual saturation magnetization of NB50 and NB100 are* $(255\pm36)kA/m$ *and* $(245\pm34)kA/m$*, respectively. Hence, the anisotropies for α and β-domains could have been calculated to be* $(23.0\pm5.0)\,kJ/m^3$ *and* $(15.3\pm4.5)kJ/m^3$ *for NB50, and* $(15.9\pm3.5)\,kJ/m^3$ *and* $(25.7\pm6.2)\,kJ/m^3$ *for NB100, respectively.*

6.7. Summary of Magnetic Properties

Within this section, a summary of coercivity, anisotropy and saturation magnetization of all six investigated samples is given. Since the values obtained by MOKE and SQUID match quite well, their reliability could be confirmed. Moreover, the derived volume density is much smaller than for poly- and even nanocrystalline nickel, suggesting a rather amorphous arrangement.

6.7.1. Saturation Magnetization

Because the saturation magnetization is proportional to both volume and density, an accurate determination is crucial. The volume was calculated by measuring the edges of the rectangular samples and considering the surface roughness, shown in Fig. 6.21(a) for NBFL. The corresponding values are very small indicating a flat sample. Only the heated samples, NBPL and NBFH, show a structured surface, which was taken into account by determining the ratio of the 100 nm deep valleys [see (b)]. Due to deviations from the ideal rectangular shape and measurement accuracy, the volume exhibits a relative uncertainty of 14%.

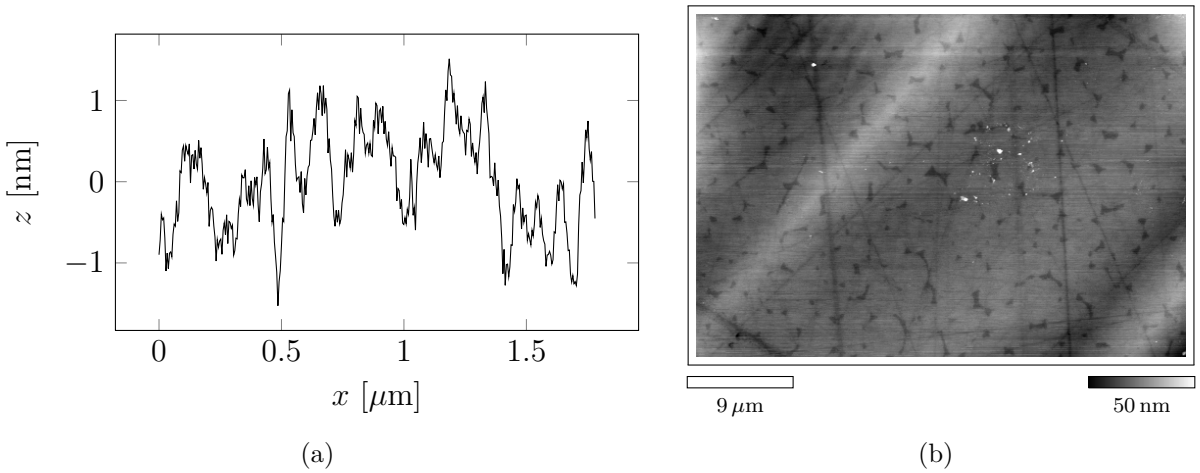

Fig. 6.21.: *(a) shows the topographical cross-section of NBFL, demonstrating a rather flat surface for non-heated samples (roughness:* 0.29 ± 0.29 *nm, waviness:* 0.42 *nm). (b) Contrary, NBPL and NBFH exhibit structured surfaces, which have to be considered in volume calculation.*

According to Tab. 6.1 all prepared samples show a saturation magnetization between 250 and 300 kA/m, which is far below the bulk value for single-crystals of 487 kA/m [see BH70, DHM68]. Since the investigated samples are supposed to be amorphous thin films,

the density will differ according to [HGKM+05] from the bulk value of 8.905 g/cm^3. The corresponding scaling factor for non-crystalline arrangement of 0.82 fits very well with the measured saturation magnetization of 390 kA/m of the Ni/Cu sample, used for determining the scaling factor of radial offset. Moreover, since neither XRD reflexes nor EBSD patterns could have been observed with these flat surfaces, the assumption of amorphous thin film should have been proven extensively. Even if the atoms are arranged in nanocrystalline structures, the contribution of non-crystalline volumes would not distinguish from pure amorphous morphology. The much lower value of all other Ni/BTO samples, is assigned to be caused by inappropriate lattice constants and lower volume density, since a lower thickness due to worse attachment of the atoms could not been verified. Furthermore, since a saturation magnetization of 255 kA/m for NB50 was measured by Gepraegs from WMI Garching, too, the calculated values are reliable. As apparent in the magnetic domain structures and the anisotropy, the deposition conditions affect the lattice constants during deposition, which could result in a difference of saturation magnetization as well. However, the slight change of the lattice constant due to heating the surface compared to Ni (3.52 Å), Cu (3.61 Å) and barium titanate (4 Å) should not cause such a remarkable distribution.

6.7.2. Anisotropy and Coercivity

In 3.3 the influence of a radial offset of the sample on both magnetization and switching field was investigated. The comparison suggested the measurement of values slightly larger than the actual ones. Additionally, since the stress within the film will show a maximum near the interface and a minimum near the surface (see 8), the switching field should be larger for SQUID than for MOKE. However, as shown in Tab. 6.1, both coercivity and anisotropy coincide within the range of uncertainty. The SQUID anisotropy is usually slightly larger, though. Consequently, the depth dependence of the stress should be rather weak. The coercivity represents a mean value, which exhibits a rather large error due to the width dependence and local variation. The width dependence is particularly apparent in small α-domains of NBPL. Moreover, since SQUID reveals only transitions proceeded by a certain volume ratio, coercivities, measured by MOKE, far off these values are not listed here to suit the purpose of comparison.

According to deposition conditions and time, passed since the last electric switching, the anisotropy, caused by the strain-mediated coupling, is within the range of 15 to 35 kJ/m^3, intrinsic stress excluded. The significant deviation of the intrinsic stress of NBFL is rather due to the sensitivity on local variations than caused by insufficient discretization during the MOKE hysteresis, as can be seen in other low-anisotropic areas.

Tab. 6.1.: *The table lists important magnetic properties of the investigated Ni/BTO samples, such as saturation magnetization, anisotropies of α, β and γ stress domains, obtained by MOKE and SQUID and the corresponding coercivities. Considering the errors, the values of both techniques match pretty well. The list is limited to the largest values measured many times by MOKE.*

sample	saturation magnetization [kA/m]	domain type	anisotropy MOKE [kJ/m^3]	anisotropy SQUID [kJ/m^3]	coercivity MOKE [mT]	coercivity SQUID [mT]
NBFL	300 ± 42	all	0.5 ± 0.5	1.2 ± 0.3	1.6 ± 0.5	1.4 ± 0.5
		β	33.8 ± 7.5	33.0 ± 7.3	5.7 ± 0.2	–
NBPL	265 ± 37	a	25.2 ± 5.5	30.5 ± 6.7	14.5 ± 2.0	14.5 ± 2.0
		γ	1.5 ± 0.3	1.2 ± 0.3	8.5 ± 1.0	5.0 ± 0.5
NBFH	280 ± 39	α	12.6 ± 2.8	14.0 ± 3.1	2.0 ± 0.5	1.7 ± 0.5
NB20	254 ± 36	α	24.2 ± 5.3	25.4 ± 5.6	5.9 ± 0.7	5.2 ± 0.5
		β	31.7 ± 7.0	33.0 ± 7.3	6.0 ± 0.8	6.0 ± 0.8
		γ	–	–	1.5 ± 0.5	1.5 ± 0.5
NB50	255 ± 36	α	25.5 ± 5.6	23.0 ± 5.0	5.0 ± 0.5	4.9 ± 0.5
		β	14.9 ± 3.4	15.3 ± 3.5	6.5 ± 1.0	7.8 ± 1.0
NB100	245 ± 34	α	16.5 ± 3.6	15.9 ± 3.5	13.0 ± 2.0	13.5 ± 2.0
		β	23.3 ± 5.1	25.7 ± 6.2	8.0 ± 1.0	8.0 ± 1.0
		β_{a_2}	1.8 ± 0.5	1.7 ± 0.4	–	–

Conclusion

In spite of the amorphous ordering within the nickel film, a remarkable influence of induced strain on the magnetic properties was observed. Since the stress domains originate from the change of the lattice constants within the BTO substrate, different types of stress, such as uniaxial compression and tension as well as isotropic compression, can be obtained by setting appropriate deposition conditions (6.1 - 6.3). The resulting magnetic easy axes are either perpendicular or parallel to the topographical steps 6.5. Due to the lack of a crystal lattice the persistent stress within the film decreases in time to minimize the elastic energy. The distribution of anisotropy will, therefore, become broader. Because the overall change of lattice constant is limited to 5 pm, the sum of switching fields before and after switching is conserved (≈ 220 mT). Since volume sensitive SQUID and surface sensitive MOKE hystereses coincide within their errors, neither depth or thickness dependence could be determined (see Tab. 6.1).

The determined saturation magnetization of nickel on BTO of 255 to 300 kA/m represent 52 to 62% of the value of single-crystalline Ni. Moreover, the saturation magnetization of nickel on Cu is 390 kA/m, representing the ordinary amorphous phase value.

7. Arrangement of the Magnetization in Stress Domains

The change of lattice constants of the ferroelectric domains causes a significant impact on the magnetic properties of the magnetostrictive film, as discussed in the previous chapter. Consequently, the magnetic domain structure will be affected as well. Within 6.1 and 6.2 continuous transitions were observed due to the lack of either α or β-domains. Here, we focus on intermediate samples, since they exhibit all three kinds of stress domains.

7.1. Magntic Domains in Boundary Areas

As already mentioned in 6.3, high deposition rate and appropriate environmental temperature cause two effective stress domains, which leads to two magnetic easy axes. An area, consisting of all three types of stress domain, is shown in Fig. 6.13. The asymmetric distribution of the magnetic domains above c-domains is explained as follows. Since the substrate exhibits topographical steps, the weight is hold by few peaks at the bottom. Further increase of the ferroelectric c-domain in the direction of such a peak would cause an even higher pressure. Since external stress affects the free enthalpy of the substrate [see (2.1.5)], this pressure initiates a transition from c to a-domain, suppressing, therefore, the growth in that direction.

The energy of a magnetic stripe, consisting of periodically alternating domains with an easy axis perpendicular to the stripe, as it is the case in β-domains, can be approximated by stray field and wall energy contributions only. This simplification is valid for hard magnetic materials, whose magnetization vectors do not tilt significantly to reduce the stray field. Although, β-domains, exhibiting flux-closure domains, were observed, it is not the case here. With w and l as domain width and stripe thickness, respectively, the energy density can be determined by $E = E_d w + \gamma_w l/w$. Here, E_d and γ_w are stray field (2.2.6) and wall energy (2.2.14), respectively. The actual energy values are of no particular interest, though. Since the first term is linear in the width and the second is linear in

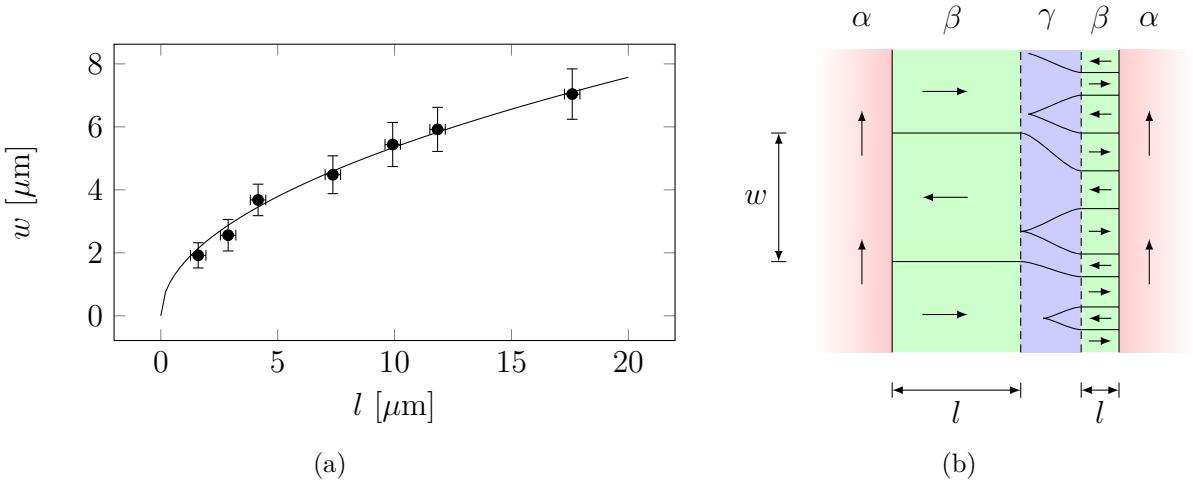

Fig. 7.1.: *The graph shows the width w of the branching-like domains as a function of the width l of the new underlying c-domains. The square root relation suggests an open domain structure, whereas actual branching would lead to a linear dependence.*

the density, minimization leads to a square root relation between width and thickness. As a result, the frequency of magnetic contrast inversion is higher in small β-domains than in larger ones [see (b)]. The data points in Fig. 7.1 show the determined period w as a function of the displacement l of the ferroelectric c-domain with errors, originating from statistical deviation. Using the derived correlation for fitting reveals a good match. Due to the continuous stress distribution within the film (see chapter 8) and the optically limited resolution, the actual width of the γ-domains appears smaller. As will be mentioned below, the tip of the branching-like domains does not mark the end, but approximately the center of the γ-domain. Instead, the position of the first curvature can be handled as the edge between β and γ-domains. Demagnetizing the system more than 5 times did not change the values, demonstrating the reliability. With increasing width of the β-domain both statistical deviation and the deviation from the square root relation increases due to the formation of flux-closure domains within α-domains [see Fig. 6.13(c)], moving the equilibrium to broader domains. In even larger areas the periodicity is completely absent. The most important result of this square root relation is the exclusion of an actual branching, which shows a linear dependence and would occur at both edges [HS09].

To clarify the physical origin of these patterns the demagnetization states at 100 mT and 0 mT are presented in Fig. 7.2, supported by an illustration of the switching process. Sufficiently large magnetic fields, exceeding each switching field, cause an alignment of the magnetization vectors along the field axis [see (a)]. Since the switching field of β-domains is much larger, e.g. 240 mT, the magnetization vectors align during the demagnetization pro-

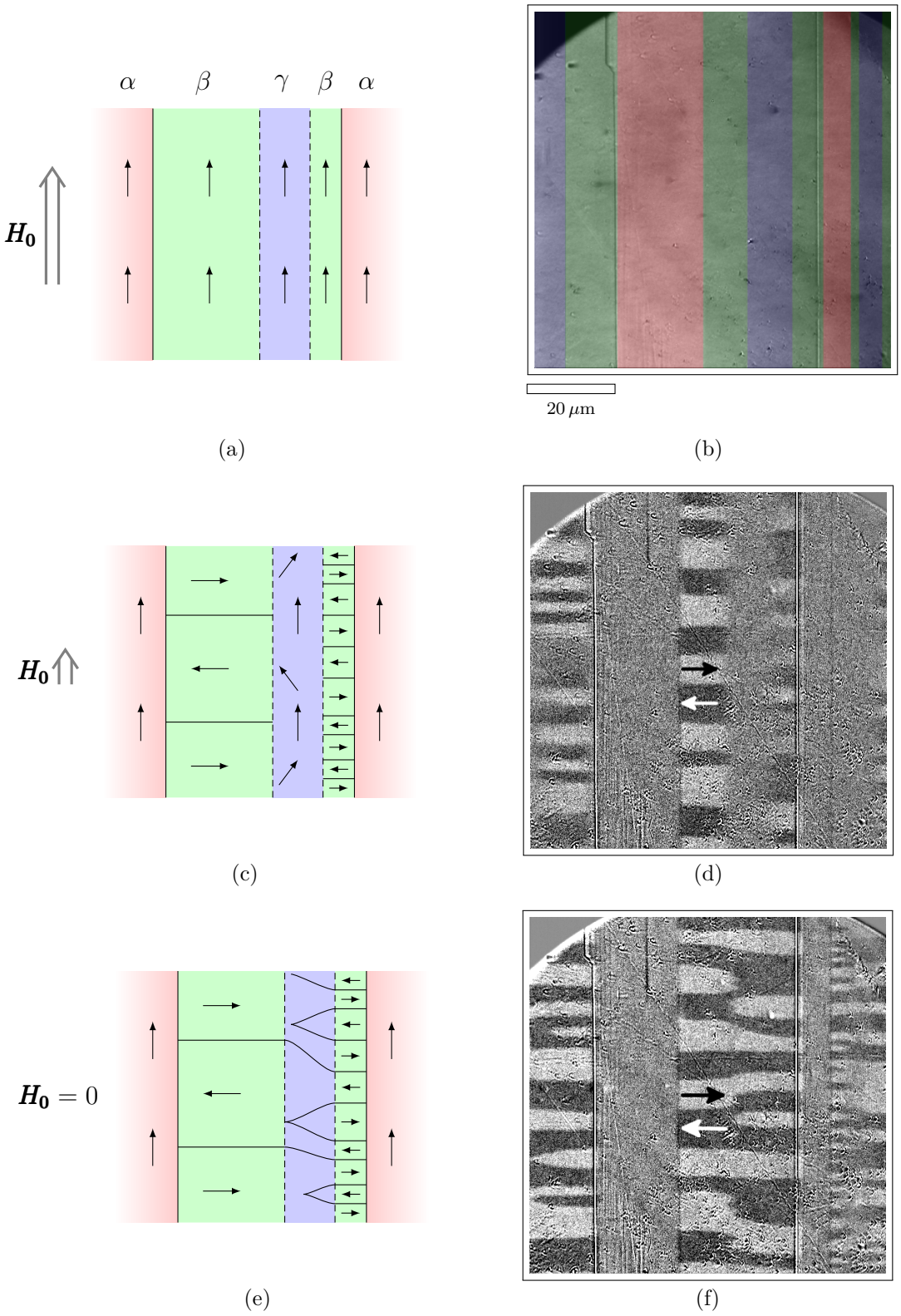

Fig. 7.2.: *The three sketches illustrate the switching behavior of β-domains in the vicinity of γ-domains in a longitudinal magnetic field, shown at the right. (a) Sufficiently large fields cause a saturation along their direction. (c) Below the switching field of β-domains the magnetization rotates into the easy axis. Because the system avoids charged domain walls, the vectors within γ-domains are slightly tilted. Depending on their width small domains will become visible at lower fields. (e) Within γ-domains the magnetization vectors are tilted to match the different widths, presenting branching-like domain patterns.*

cess within each stripe independently and according to Fig. 7.1, as illustrated in (c). The rather large values of anisotropy of α and β-domain cause an abrupt transition and strong contrast at the corresponding edge, suppressing any tilt of the magnetization. At the edge between β and γ-domain the contrast becomes weaker due to blurring, representing the tilt of magnetization vectors. The resulting configuration minimizes both the anisotropy and stray field energy*. The actual equilibrium of the overall energy depends on the width of the β-domain, demonstrating a smaller switching field for small widths [see (c)], since the impact of stray fields retains, whereas the anisotropy scales. Moreover, according to this width, the dimensions of the magnetic domains vary. Asymmetric growth induces, therefore, charged magnetic domain walls, which can be eliminated by tilting the magnetization and curving the domain walls within γ-domains. Consequently, a branching-like domain pattern is formed, whose curvature is confined to the area of the lowest anisotropy [see (e)]. For symmetrically grown c-domains the branching does not have to occur in any case.

The branching-like domain patterns, however, appear only in the absence of a magnetic field, if two c and β-domains, respectively, merge during the application of an electric field. As could be shown in Fig. 7.3, once the magnetic system is demagnetized an increase of the underlying ferroelectric c-domain does not lead to an adjustment of the width of magnetic domains according to Fig. 7.1. Since the magnetic domain structure of the "old" region is fixed and does not jump into another state, a tilting of the magnetization in β-domain would be required. This causes, unfortunately, due to the deviation from the easy axis and longer domain walls, a significant increase of the energy, which restrains the motion immediately. Instead, the magnetization vectors of the recently switched domains align to retain the width Fig. 7.3(d). This holds both for in- and decrease of ferroelectric c-domains and is a fundamental requirement for the occurrence of zig-zag walls, observed in α-domains.

*Since the exchange energy is independent from stress and magnetic field, and has to be considered always, it was and will never be mentioned explicitly.

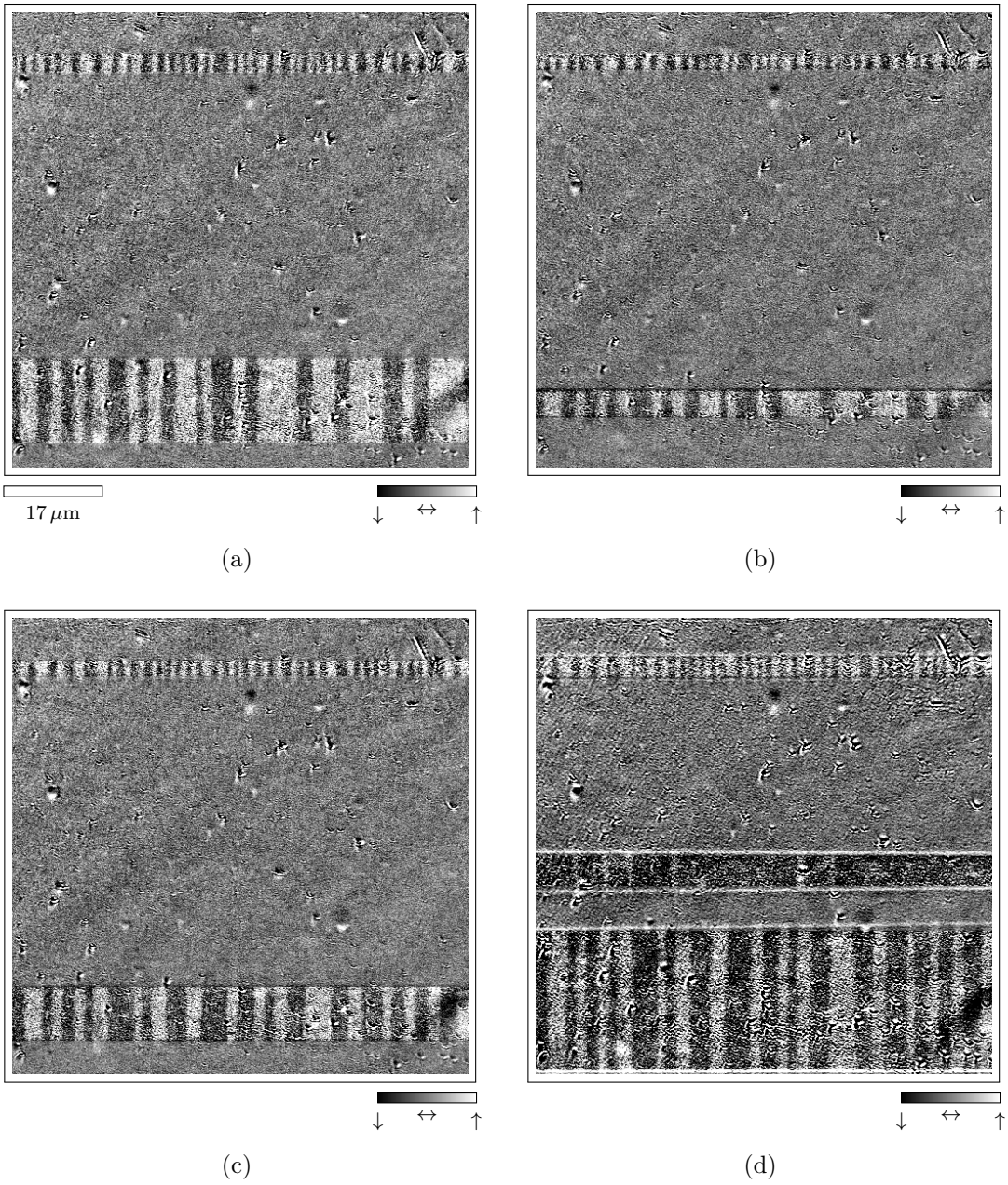

Fig. 7.3.: *Conservation of the magnetic domain width during the application of an electric field. Once the magnetic system is demagnetized [(a), (c)], the width of the magnetic domains retains, even if the underlying ferroelectric domain de- or increases [(b), (d)]. The ground state of the new configuration can only be obtained by applying an oscillating magnetic field. Moreover, conservation of the width is required for the existence of zig-zag domain walls, observed in "virgin" samples after several electric hystereses.*

7.2. Magnetic Domain Walls

Although magnetic domains could, in principle, be investigated by MOKE imaging as well, MFM seems more suited due to its high resolution and charge sensitivity. Furthermore, the interaction does not destroy the current state, as the application of a magnetic field it does. Fig. 7.4 shows the MFM phase of an area, consisting of all three types of stress-domains. The corresponding features are branching-like domains, straight and zig-zag domain walls. Zig-zag walls can originate from two complementary sources. Assuming crystalline morphology, the easy axes of nickel, coinciding with the diagonals of a cube <111>, would result for a <100> oriented surface in such an arrangement [see HS09]. However, there are plenty of aspects, which prohibit this case. The first point is the morphology of the film, which would not change exactly at the edge of each ferroelectric domain, as it has to, since the magnetic structure is totally different within α and β-domains. Moreover, a distinct out-of-plane contrast in both MOKE and MFM images would have to appear. Thirdly, the film thickness of few tens of nanometers does not allow volume domains.

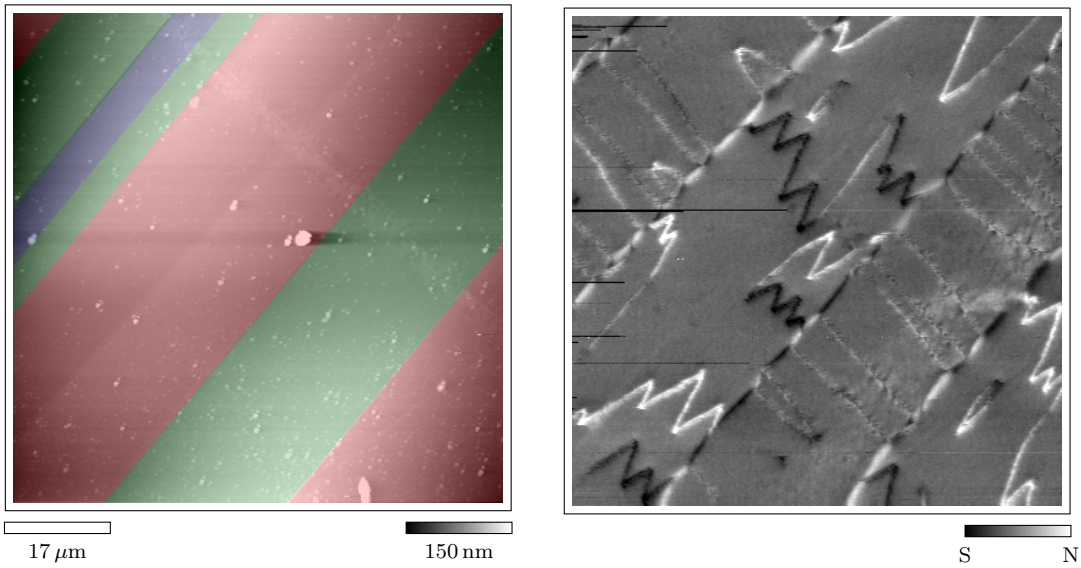

Fig. 7.4.: *Topography (a) and MFM signal (b) of NB100, taken before exposing to an artificial magnetic field, used by MOKE, illustrate the connection between topographical steps and stress domains. Because the magnetization is pointing perpendicularly to the steps within β-domains, lines of alternating contrast covering the peaks and hills appear. The zig-zag walls above α-domains, rarely observed by MOKE as relaxation states, are caused by the intention of decreasing both stray field and wall energy during the electric hysteresis and exhibit, therefore, the opposite contrast.*

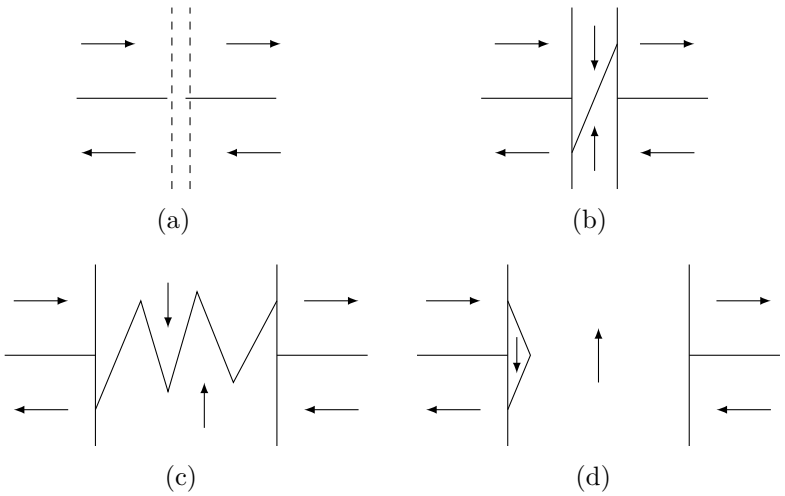

Fig. 7.5.: *Remarks on the formation of zig-zag walls. (a) Assuming a continuous nucleation of a-domains within c-domains (illustrated by dashed lines), the occurrence of magnetic charges results in a magnetic head-to-head domain wall within α-domains for the sake of flux-closure (b). Increasing the size of the a-domain further, causes a change of the angle between wall and magnetization, because both ends are bounded. (c) Exceeding a certain angle, kinks are induced. Exposing the system to a magnetic field, destroys usually every zig-zag wall, since both the anchors of the walls are vanquished and the rotation of the magnetization near these walls results in divergence contribution. Instead, two different types of configurations are preferred. Since broad c-domains favor large magnetic domains, the generated stray field is usually reduced by flux-closure arrangement, as illustrated in (d) and observed in Fig. 6.13. The most common type is a slightly curved wall, similar to (b).*

Instead, these zig-zag walls are formed during the growth of new a-domains for the sake of flux-closure. For further clarification Fig. 7.5 illustrates the physical origin of zig-zag walls and their derivatives. According to Fig. 7.1 the width of a magnetic domain within β-domains depends on the width of the underlying ferroelectric domain. Consequently, new β-domains, which nucleate within α-domains, exhibit small magnetic domains. The width will increase, when the β-domains are sufficiently broad. As a result, the width of magnetic domains will be few micrometers. If the sample was exposed to a magnetic field, the width of magnetic domains will be larger and branching-like domain patterns will occur. Reducing the electric field causes nucleation of a-domains [see Fig. 7.5(a)], which induce tensile stress and an easy axis parallel to the steps. If the reduction is done rather slowly, the resulting surface charges can be minimized by forming flux-closure domains, which correspond in that case, according to (b), to a domain wall, fixed at the middle of similar charged edges of magnetic β-domains. Since the wall contains energy, the length of the edge has to exceed a certain value. Therefore, the flux is conserved, minimizing the stray field energy. The resulting head-to-head and tail-to-tail domain walls cause an inverted

magnetic signal, compared to the surface charges, the walls originate from [see Fig. 7.4(b)]. To minimize the stray field the magnetization in the vicinity of the wall is supposed to tilt slightly [HS09]. Decreasing the electric field further increases the angle between wall and step due to pinning of the anchor points. If the projection of magnetization exceeds a certain value, which depends on the wall energy density (2.2.13) and the wall length, a kink is induced into the wall [see (c)], representing the first zig. At zero field α-domains will show a lot of zig-zag walls of different elongation but rather similar frequency. The elongation is, apparently, influenced by the velocity of ferroelectric domain growth.

Since these walls are magnetic monopols, which are merley pinned at the anchor points, the interaction with the magnetic tip during two-pass scan induces motion, as shown in Fig. 7.6. Hence, dark lines are pushed, while bright ones are pulled, leading to an annihilation of narrow domain walls with small elongation. This mobility and the possibility of contrast inversion (see straight white line) suggests further a totally in-plane magnetization and the instability of these zig-zag walls. Due to the lack of anchor pinning and the corresponding wall energy, zig-zag walls were rarely observed by MOKE imaging. A derivative is shown in Fig. 7.5(d), which is favored in case of large c-domains, such as

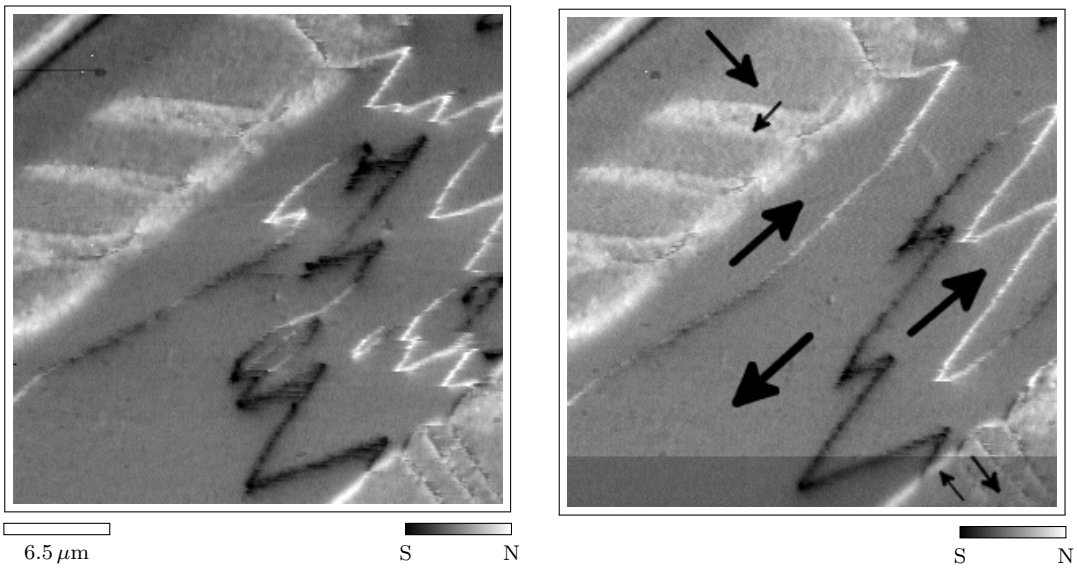

Fig. 7.6.: *Mobility of zig-zag walls. Both MFM images were obtained by scanning the sample with common magnetic tips right after each other, leading to a strong interaction. Apparently, these walls are moved and even annihilated by the tip. As a result, the density is reduced and the wall length is increased. Moreover, since the long straight wall aligns parallel to the easy axis, the contrast and orientation of the Bloch wall change. The magnetization of the domains are indicated by arrows.*

Fig. 6.13. Another type is a simple, slightly curved wall, similar to (b). This wall exhibits a lower energy, since divergences caused by tilting are avoided. Comparing the angles of zig-zag and simple wall of $(50 \pm 1)^\circ$ and $(40 \pm 1)^\circ$, respectively, illustrates the contribution.

Whereas domain walls in stress-free NBFL [Fig. 6.2(b)] often belong to cross-tie walls, which are favored in low-anisotropic media [HS09], NB100 and other intermediate samples exhibit two different wall types. According to (2.2.13) the two magnetization components of a 1D domain wall are symmetric (2.2.16) and asymmetric (2.2.15). Since Bloch walls do not show volume divergence, merely surface charge $\sigma = \boldsymbol{nM}$ contribute. Assuming a flat surface, the phase difference (3.1.7) can be approximated by the second derivative of the magnetization. The symmetric phase shift [see Fig. 7.7(a)] above a-domain walls suggests, therefore, Bloch walls, whose existence was verified by micromagnetic calculations with the aid of Nmag [FF10]. Although the head-to-head and tail-to-tail configuration causes a strong monopol field, higher orders, originating from volume divergences, would have some impact on the symmetry. Contrary, the straight 180° β-domain walls are asymmetric. In case of symmetric 1D Néel walls surface charges are avoided, since the rotation takes place in-plane. Apparently, the resulting divergence can be described by (2.2.15), which originally determined the in-plane component of Bloch walls. Because both walls only distinguish in x and y, this relation is quite intuitive. Following the mentioned steps leads to the fit, shown in Fig. 7.7(b). Despite the approximations both data and fit match very well. The occurrence of 2D domain walls, such as asymmetric Bloch walls, would cause a superimposition of both phase shifts, leading to a quite different shape.

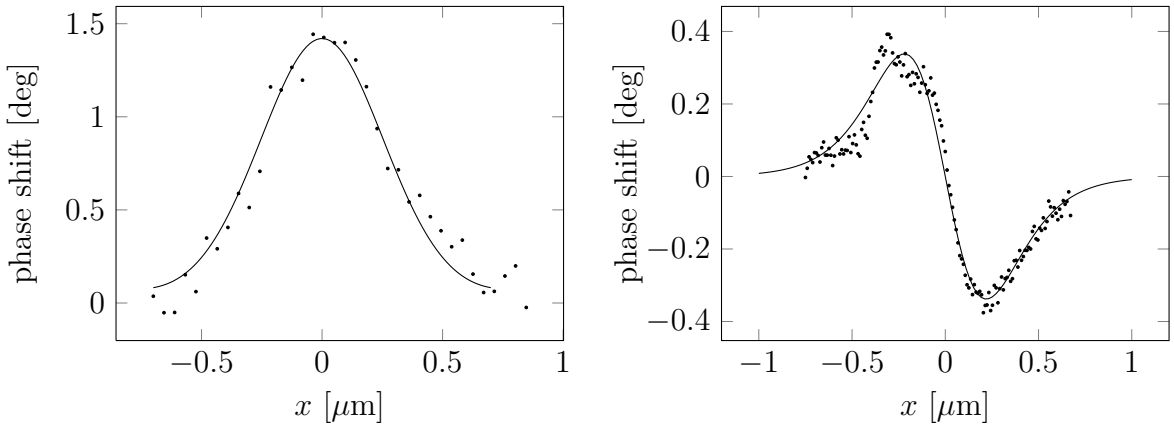

Fig. 7.7.: *The two graphs show the phase shift, extracted from MFM images, of zig-zag walls (a) and the straight walls (b) located above a and c-domains, respectively. The line plots represent the fit for a symmetric 1D Bloch and Néel wall, apparently matching very well.*

7.3. Mapping of In-Plane Anisotropy

During the investigation of several intermediate samples areas of slightly bright contrast, such as Fig. 7.8(b), were observed. Although some contrast originates from Néel walls, the main contribution is an area effect. Due to their coincidence with topographical steps, which correlate with ferroelectric domains, a superimposition of magnetostatic and electrostatic interaction could be likely. Therefore, the magnetic tip was replaced by a conductive Au tip, allowing the detection of electrostatic charges separately (d). The images show an area, slightly translated due to the different tip geometry. Since the sample is homogeneous, it does not affect the results. Because of the shielding of free carriers within the nickel film no electrostatic signal was observed. Instead, a cross-talk of the topography is displayed. Thus, the bright stripes belong to an actual magnetic signal. According to (3.1.9) merely magnetic surface charges are detected by MFM. Since volume divergences are confined to domain walls or vortex states, they are of no importance here. Consequently, these areas heave to exhibit magnetization components normal to the surface. However, this objects the results, obtained by MOKE imaging [see Fig. 6.13(d)], and the physical explanation, mentioned in the previous section.

As shown in Fig. 7.6, the interaction between tip magnetization and surface charges is very strong, particularly due to the first pass, proceeded in intermitted mode. In 2.2.4 the energy density of an uniform magnetic domain within an magnetic field is given. Minimizing the energy (2.2.10) with respect to the magnetic field leads to the magnetization curve. Thus, each line scan, performed with a magnetic tip, affects the easy axis of the sample by favoring a small out-of-plane component. Since the exchange energy is not considered by this formula, an uniform magnetic field and homogeneous magnetic properties throughout the sample are required. The latter case excludes boundary regions. Moreover, the presence of a magnetic field causes in the first order a tilting angle distribution of the shape of a gaussian function with a center below the tip. Since the image is detected pixel-wise, the measured phase shift is always affected by the same gaussian distribution as long as no topographical cross-talk and boundary effects contribute. Consequently, although the measured signal is homogeneous shifted, qualitative analyses can be proceeded. Assuming a linear relation between applied field and normal component, which is most likely, the slope depends, according to $B_s = 2K/M_s + \mu_0 N M_s$, both on the overall uniaxial anisotropy constant and the shape of the sample. Here, B_s describes the switching field. Since α-domains exhibit easy planes, their anisotropy constant should not contribute. The constant compression along the topographical steps will ensure a small easy axis parallel to the steps, though. On the other side, the longitudinal alignment results in a demagnet-

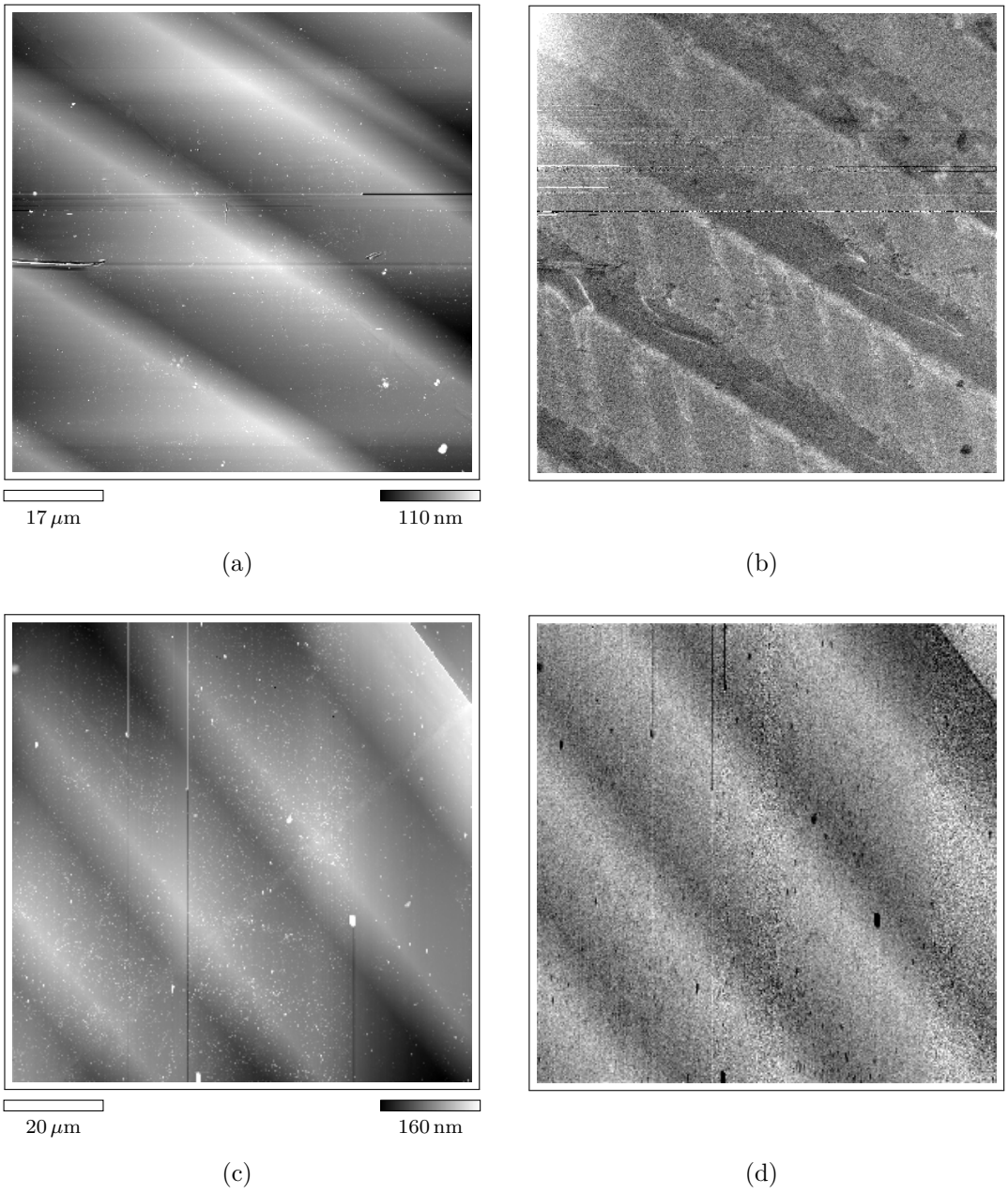

Fig. 7.8.: *Because of similarities of magnetic phase contrast (b) and the underlying ferroelectric domains (a), one could assign the stripes to some electrostatic cross-talk. To verify this assumption a non-magnetic, conductive Au cantilever was used. The corresponding topography and EFM phase are shown in (c) and (d), respectively. Since the contrast does not originate from electric interaction, it displays areas of low in-plane anisotropy.*

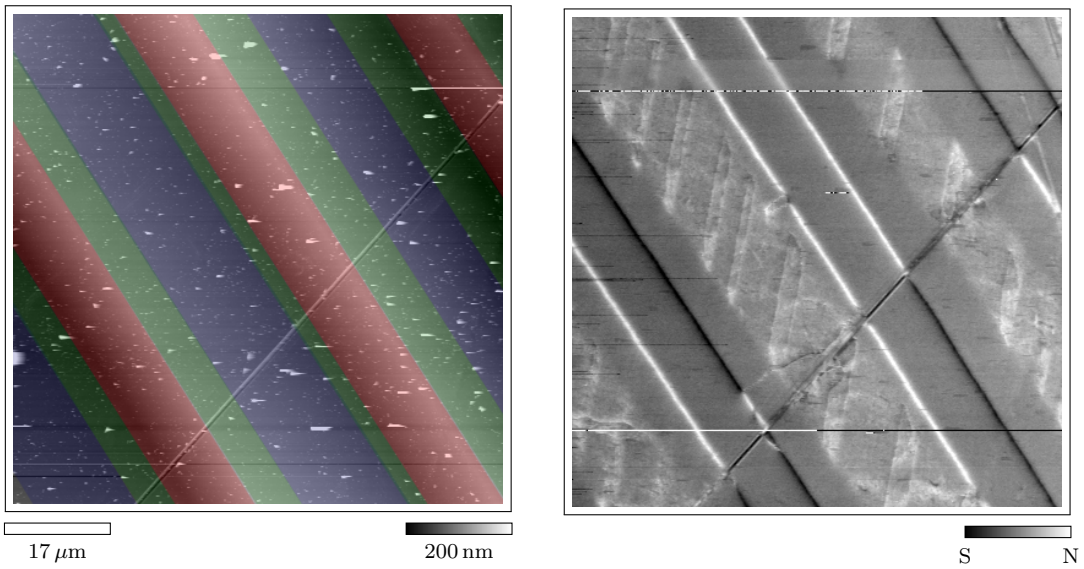

Fig. 7.9.: *(a) and (b) show topography with distribution of stress domains and MFM signal after exposing NB100 to both electric and magnetic field, respectively. Since the magnetic field, which was oscillating perpendicularly to the steps, allows the system to get rid of the unfavored zig-zag walls, nothing similar is observed. The 90° domain walls within the bright stripes, located above c-domains, illustrate both a deposition on a_1/a_2-domain patterns and the aging of the film. Therefore, the anisotropy decreases in time, leading to slight tilting of the magnetization vector within a normal magnetic field, as the tip generates.*

ization factor $N \simeq 1$, as could be determined by Nmag. Contrary, the decrease of the lattice constant leads to transverse isotropic stress above old c-domains. New c-domains induce large compressive stress perpendicular to the steps. In either way, the in-plane anisotropy constant differs from zero. The demagnetization factor is for widths of ferroelectric c-domains of few tens of micrometer larger than 0.95. As a result, γ-domains do not show a strong in-plane preference, leading to bright areas in MFM images. Although this is qualitatively persuasive, the small difference between the demagnetization factors should not have a significant impact.

Such a tilt is in β-domains suppressed due to the large in-plane anisotropy, as apparent in Fig. 7.9. Here, the system was demagnetized by a magnetic field perpendicular to the steps. Therefore, no straight Néel walls within β-domains are observed. The violation of the alternating surface charges in the upper right is quite unusual, though. Since the contrast within α and β-domains is equal to zero, the corresponding magnetization vectors are not affected by the tip. Furthermore, the appearance of domain walls, aligned under 45 degrees to the steps, above old c-domains is a certain proof for the relaxation of the

nickel film in time. A few remarks on this topic were already given in 6.3 at the end. As shown in Fig. 6.15, the deposition on top of a_1/a_2-domain patterns results in an alternation of parallel and perpendicular easy axes. Since the sample was exposed to an electric field, these patterns are conserved by rotating the easy axes by 90 degrees due to the reversed sign of stress. In time the film relaxes, decreasing both stress and switching field. Because the boundary regions changes by applying an electric field quite often the sign, the frequently refreshed stress is sufficiently high to suppress tilting of the magnetization.

Conclusion

Distinct magnetic domain patterns were observed within different types of stress domains, which induce varying magnitude of anisotropy and orientation of the easy axis. For instance, the occurrence of a β-domain leads to continuous transitions of the magnetization alignment within isotropically stressed γ-domains. A more frequently arrangement of β-domains results in branching-like domain patterns above old and new c-domains due to spatial separation and corresponding decoupling (see 7.1).

The increase of c-domains by driving electric loops does not change the period of alternating magnetic domain walls. Consequently, new α-domains, nucleating in β-domains, exhibit magnetic domains for flux-closure, which are pinned to the charged edges between α and β-domains. Further increase of α-domains leads to zig-zag walls, showing Bloch wall symmetry. Contrary, the magnetic domain walls within β-domains are Néel walls.

Mapping the in-plane anisotropy by means of MFM, results in an affection of γ-domains due to absent anisotropy. α and β-domains do not show a detectable tilt of the magnetization vector. Therefore, for α-domains the consideration as an easy plane, which is suppressed by the shape anisotropy, is insufficient.

8. Modeling the Stress Distribution within the Film

Although the qualitative explanation of induced anisotropy, used in 6.1 - 6.3, is intuitive and applies in many cases, an advanced model is presented here. With the aid of the coherence technique, the stress distribution within the film is modeled, allowing statements, for instance, on transition areas and saturation stress.

Fig. 8.1 shows the transverse contrast of a longitudinal demagnetized state of the stress domain distribution (a) of an intermediate sample. Since the branching-like domains were already discussed in 7.1, we will focus here on the vicinity of the two small (red) α-domains. Similar states were obtained by demagnetizing the system for more than five times, demonstrating the reliability. The alternating contrast in between these α-domains in the center of (b), which obeys the width-width relation (see Fig. 7.1), verifies the existence of actual tensile stress within the α-domains. The upper end, however, does not show such an alternation. Instead, both width and longitudinal offset of the large magnetic β-domains coincide, suggesting a coupling beyond the stress domains. The corresponding transition width of the stress is certainly of interest for scaling applications, since it demonstrates the minimum size.

In 6.7.2, volume and surface anisotropies were compared, exhibiting negligible differences. Since there will definitely be a gradient, its magnitude would be of interest. Moreover, the mentioned deviation from the polycrystalline saturation magnetization proposes a true amorphous morphology with distinct volume density (see 6.7). Because elastic coefficients and magnetostriction are further properties, which depend on the density, the final stress will be affected.

8.1. Adaption to Ni/$BaTiO_3$

For this purpose the coherency technique is adapted to an amorphous, isotropic thin film, whose bottom surface was stressed with respect to the change of the lattice constants of

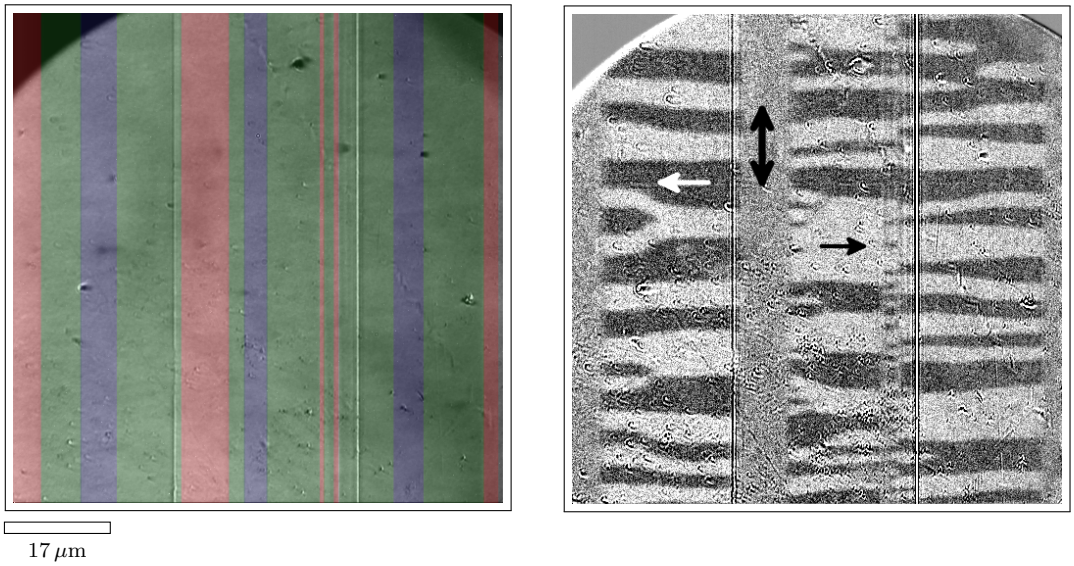

(a) (b)

Fig. 8.1.: *Stress transition width. Distribution of stress domains (a) and longitudinal demagnetized state (b) of NB100 are shown. Apparently, a coupling abroad the boundaries occurs.*

the substrate (see Fig. 2.6) due to either thermal or electric phase transition. Within this framework, merely stress, according to dislocation theory, is considered. Consequently, back coupling of the film, elastic and further magnetic energy contributions are neglected. Since the substrate is both single-crystalline and much larger in size, the first simplification is appropriate. Whereas the neglect of the elastic energy is an actual approximation, magnetic contributions, particularly stray fields, will affect the resulting magnetic domain structures rather than the stress distribution itself. Because the analytical theory is restricted to plane-strain, the final stress distribution is obtained by linear superimposition, as it is done, for instance, for the uniform compression along the topographical steps. With the aid of the relation of magnetostriction (2.2.9), the calculated stress is converted into the anisotropy.

With the aid of the analytical formulae (A.2), the shear modulus $\mu = 40.5\,\mathrm{GPa}$ and the Poisson ratio $\nu = 0.3$ of nickel [HGKM+05], both stress and anisotropy distribution were calculated. Fig. 8.2 shows the transverse stress component σ_{yy} [(a), (b) and (c), (d)] and the transverse anisotropy [(e), (f)] for paraelectric deposition (NBPL). Whereas (a) and (b) display the stress due to the displacement perpendicular to the steps, (c) and (d) consider additionally the topographical steps and the constant compression along the steps. Consequently, peaks and a constant offset are induced. Since the calculation was done for various depths, different line colors refer to interface, surface and embedded area.

Moreover, [(a), (c), (e)] and [(b), (d), (f)] belong to periods of 6 μm and 1 μm, respectively.

8.2. Discussion

Due to the absence of crystalline ordering, the peaks, originating from topographical steps, will certainly disappear soon. Since these peaks are very small, they are not observable by MOKE imaging. However, their occurrence does not have an influence on the transition width or saturation stress. Although the expansion of the unit cell in a-domains causes a significant contribution in (a) and (b), the compression along the steps induces via Poisson ratio a constant compression. Since the anisotropy is determined by all three components, a superimposition of easy plane and easy axis occurs. As a result, the in-plane anisotropy of α-domains differs from zero and has to be considered for out-of-plane fields (see 7.3). Becaus the isotropically stressed γ-domains exhibit the same compressive stress, but show a rather low in-plane anisotropy, the geometry of the thin film must have an impact on the easy axis of α-domains. Although the qualitative explanation, used in 6.1 - 6.3, does not consider this coupling, its results are similar for in-plane properties by minimized complexity.

Apparently, the transition between compressive and tensile stress is determined by the theory itself and does not depend on parameters, which is characteristic for continuum mechanics. The elastic and magnetostriction constants modify the saturation stress, though. The actual stress and anisotropy depend on the thickness-to-period ratio, which can be adjusted by an external electric field. Consequently, domains with a width of $< 2\mu$m do not reach their saturation anisotropy in 50 nm thick films. Significantly smaller domains could even exhibit reversed stress. Despite the limited resolution, a verification cannot be given, since the stray field contribution will already cause a rotation of the easy axis by 90° at small anisotropy values. Moreover, γ-domains exhibit small anisotropy, too, which could not be verified for the same reason.

As apparent in Fig. 8.2, both stress and anisotropy do not depend on depth for investigated thicknesses and resolvable periods. Additionally, the difference between the anisotropy of 20 nm and 100 nm thick Ni films is $(4.0 \pm 1.6)\,\mathrm{kJ/m^3}$. Considering the error, the stress does not show a remarkable thickness dependence either, which was verified by SQUID and MOKE.

Although the applied elastic coefficients were already scaled according to [HGKM+05] by 0.9 to consider nanocrystal morphology, the calculated anisotropy values are far too large. A reduced change of lattice constants of the substrate due to the film is unlikely. In 6.7.1, a volume density of 0.8 times the single-crystal value was determined from the

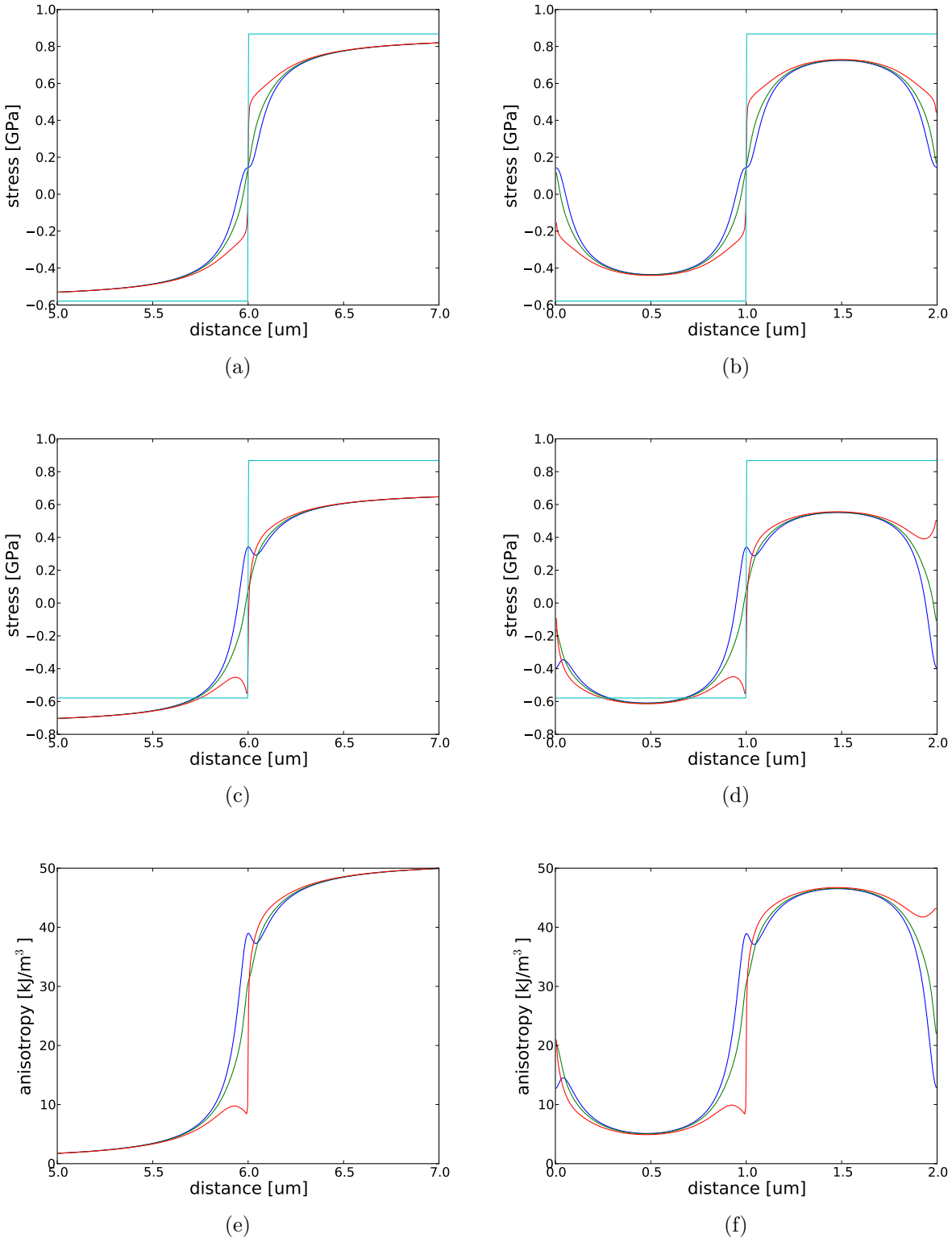

Fig. 8.2.: *Calculated transverse stress and anisotropy distributions for NBPL for two different widths of ferroelectric domains: 6µm [(a), (c), (e)]; 1µm [(b), (d), (f)]. (a) and (b) plot the transverse stress due to compression perpendicular to the steps. (c) and (d) consider additionally the slope due to topographical steps and the compression along the steps. — displays the value for an infinitely extended stress domains. (e) and (f): effective in-plane anisotropy (if positive, easy axis perpendicular to steps). Different depths are considered: 50 nm: — , 25 nm: — , 0 nm: — .*

ratio of saturation magnetizations. As mentioned, this value fits quite well with 0.82, determined in this paper for inter-crystalline volumes. Consequently, conserving the Poisson ratio, the shear modulus becomes for amorphous nickel (0.61 ± 0.25) times the nanocrystal value 40.5 GPa. Here, both calculated and measured anisotropy of $(50 \pm 10)\,\mathrm{kJ/m^3}$ and $(30.5 \pm 6.7)\,\mathrm{kJ/m^3}$, respectively, are used. The error for calculation considers the uncertainty of both shear modulus and displacement. Unfortunately, a literature values was not available. Assuming a linear dependence of the elastic coefficients on the volume density, the corresponding scaling factor of 0.54 with respect to single-crystal values is within the range of 0.52 to 0.62, determined from the ratio of saturation magnetizations.

The application of the coherence technique to non-paraelectric deposition leads to appropriate in-plane values, too. Unfortunately, the out-of-plane anisotropy of α-domains increases remarkably. Because no phase shift was ever observed above α-domains during MFM scan, this order of increase is not physical. However, since it was not intended to determine out-of-plane anisotropies, the consideration as an appropriate method for stress and anisotropy calculation within films is still justified.

Conclusion

Within the framework of the coherence technique, both stress and anisotropy distributions were calculated. As a result, for non-ferroelectric deposition, the tensile stress perpendicular to the topographical steps within α-domains is significantly reduced, while compressive stress along the steps occurs. Therefore, α-domains exhibit a superimposition of easy plane and easy axis. The calculated anisotropy of α-domains in case of paraelectric deposition is similar to the value of β-domains in case of ferroelectric deposition, namely $(50 \pm 10)\,\mathrm{kJ/m^3}$. This value is approximately 1.6 times the measured value. Applying the scaling factor of the volume density, determined in 6.7.1, leads to a good match. Since the transition is determined by the theory itself, merely stress magnitude can be set by varying thickness-to-period ratio. Consequently, small stress domains do not reach the saturation stress. If the period is sufficiently small, the stray field will ensure a coupling abroad the domain boundaries. Furthermore, neither thickness nor depth dependence of the stress was observed within the investigated ranges, which is in agreement with experiments.

9. Summary and Outlook

9.1. Summary

Within the present thesis, the strain-mediated coupling in magnetoelectric composites was investigated. For this purpose, magnetostrictive nickel was deposited on top of ferroelectric barium titantate (BTO) single-crystal. Due to the change of lattice constants within the substrate either by temperature, pressure or electric field, strain and stress were induced into the film, leading to an influence on the magnetic properties. A series of samples had been prepared by Sputtering and Electron Beam Vapor Deposition to determine the dependence of induced stress on deposition rate and temperature as well as thickness.

Since the stress originates from the change of lattice constants, the ferroelectric domain structure of the substrate was investigated first by Piezoresponse Force Microscopy. As a result, a correlation between topography and ferroelectric domains was observed, which is caused by the tetragonal symmetry of the unit cell. The typical topographical steps with a slope of 0.6° were used to assign the ferroelectric domains in optical observation techniques. Furthermore, a_1/a_2-domain patterns were found to occur also in single-crystals.

The investigation of the magnetic properties was carried out with the aid of Magnetic Force Microscopy (MFM), Magneto-Optical Kerr Microscopy (MOKE imaging) and a Superconducting Quantum Interference Device (SQUID) magnetometer. Whereas MFM is sensitive to magnetic stray fields, MOKE imaging dispalys the magnetization component, perpendicular to the polarization plane of the linear polarized light. Consequently, magnetic domain walls were observed by MFM, while demagnetization states, coercivity and anisotropy were investigated by MOKE. For calculation of the anisotropy, the saturation magnetizations were determined by SQUID.

The deposition at room temperature and low rate led to no induced stress. The corresponding anisotropy of $(1.2 \pm 0.3)\mathrm{kJ/m^3}$ displayed the intrinsic anisotropy of magnetostrictive glasses. The application of an electric field induced locally a magnetic easy axis perpendicular to the topographical steps and an anisotropy of $(33.0 \pm 7.3)\mathrm{kJ/m^3}$ due to both negative magnetostriction and electric phase transition from a to c-domains within BTO, corresponding to a displacement of the unit cell of 5 pm.

The deposition on (quasi-)paraelectric BTO resulted in an easy axis parallel to the steps with an anisotropy of $(30.5 \pm 6.7)\mathrm{kJ/m^3}$ in absence of an external electric field. The application of an electric field caused a rotation of the easy axis by 90° and an anisotropy of $(3.3 \pm 0.7)\mathrm{kJ/m^3}$. Since this value differed from the intrinsic one a tuning of the lattice constant was suggested, in spite of the discrete room temperature values.

An appropriate adjustment of deposition rate and temperature led to the coexistence of two easy axes with remarkable anisotropy. Because of varying anisotropy branching-like domain patterns were observed above *c*-domains. Moreover, different types of domain walls occurred above *a* and *c*-domains, which could be assigned to Bloch and Néel walls.

The determined saturation magnetization of all samples was within the range of 255 to 300 kA/m, representing 52 to 62% of the single-crystal value. Neither thickness nor depth dependence of the stress could have been observed.

The adaption of an analytical approach allowed the quantitative illustration of the stress distribution within the nickel film. The use of polycrystal values for magnetostriction and shear modulus cause a too large anisotropy, though. Since the volume density of the film was determined to be 52 to 62% of the single-crystal value, the shear modulus was also multiplied by 0.54, leading to coincidence.

9.2. Outlook

Within this thesis, the strain-mediated coupling in $Ni/BaTiO_3$ was investigated. Due to general mechanisms, the derived results are, in principle, applicable to other magnetoelectric composites. This implies both magnetostrictive film and dielectric substrate.

The 90° rotation of the magnetic easy axis within these composites makes them very interesting as spin-polarized electron sources. However, since emission requires insulators, magnetostrictive antiferromagnets are necessary. Therefore, the use of single-phase magnetoelectric media is recommended.

A. Appendix

A.1. Exchange Energy in Continuum

The Heisenberg exchange energy $\mathcal{H} = -\sum_{(ij)} J_{ij}\boldsymbol{S}_i\boldsymbol{S}_j$ describes the interaction of the electron spin $\boldsymbol{S}_i$ at the i-th lattice point with its neighbors (see Fig. A.1). Since $\boldsymbol{S}_i$ are normalized, the scalar product can be transferred into $\boldsymbol{S}_i\boldsymbol{S}_j = \cos\varphi_{ij} = 1 - \frac{1}{2}\varphi_{ij}^2$. This approximation is valid, due to the rather small spin rotation. Furthermore, the relations $\varphi_{ij} = \frac{r_{if}}{|\boldsymbol{S}_i|} = r_{ij} = |\boldsymbol{S}_i - \boldsymbol{S}_j|$ can be applied. The latter relation is an approximation, since the angle is defined rather by the energy contributions than by the lattice constant. However, due to the transfer to continuum, the actual length does not matter here. With the aid of the Taylor expansion this leads to $\varphi_{ij} = |(r_{ij}\nabla)\boldsymbol{S}_i|$. Assuming a periodic arrangement with the lattice constant $a = r_{ij}$ and the exchange constant J, the exchange energy reads in continuum:

$$\mathcal{H} = -J + \frac{J}{2a}\int (\nabla\boldsymbol{S})^2 \, \mathrm{d}^3r \,. \tag{A.1.1}$$

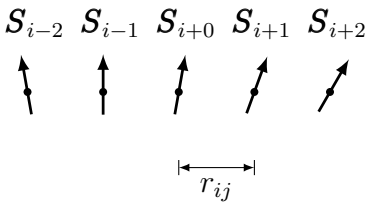

Fig. A.1.: *Sketch illustrates the geometry of a spin lattice, required for transformation into continuum.*

A.2. Stress Field Distributions in Thin Films

In the following, the stress field distributions σ_{ij} within thin films originating from a change of lattice constants are given. They have been calculated according to 2.4 with the aid of edge dislocations for a periodic arrangement of κ domains. The corresponding domain widths are considered by l_g, whereas $l_0 = 0$ and l_κ is the period p. x, y and z are normal,

perpendicular and parallel component with respect to the topographical steps, respectively. Due to the reduction to two dimensions, plane-strain conditions can be used, at least in first order. H displays the film thickness and Θ is the Heaviside function. μ and ν are shear modulus and Poisson ratio, respectively. Moreover, $x_p = x + H$, $x_m = x - H$ and:

$$f(x,y) = \arctan\left[\frac{\tan\frac{y}{2}}{\tanh\frac{x}{2}}\right] + \pi \operatorname{sgn} x \operatorname{sgn} y \left[\Theta(y+2\pi)\Theta(-y-\pi) + \Theta(y-\pi)\Theta(2\pi-y)\right] . \tag{A.2.1}$$

Summation over all domains reveals the overall stress field distribution:

$$\sigma_{ij} = \frac{\mu}{2\pi(1-\nu)} \sum_{g=1}^{\kappa} \varepsilon_g \left[F_{ij}\left(\frac{x}{p}, \frac{y-l_g}{p}\right) - F_{ij}\left(\frac{x}{p}, \frac{y-l_{g+1}}{p}\right)\right] , \tag{A.2.2}$$

with

$$F_{xx}(x,y) = \frac{x_p}{2}\left(\frac{\sin y}{\cosh x_p - \cos y} - \frac{\sin y}{\cosh x_m - \cos y}\right) - xH\frac{\sinh x_m \sin y}{(\cosh x_m - \cos y)^2} , \tag{A.2.3}$$

$$\begin{aligned} F_{yy}(x,y) = {} & 2f(x_p,y) - 2f(x_m,y) - \frac{x_p}{2}\frac{\sin y}{\cosh x_p - \cos y} + \\ & + \frac{x-3H}{2}\frac{\sin y}{\cosh x_m - \cos y} + xH\sinh x_m \frac{\sin y}{(\cosh x_m - \cos y)^2} \end{aligned} , \tag{A.2.4}$$

$$\begin{aligned} F_{xy}(x,y) = {} & \frac{1}{2}\left[\ln\left(\frac{\cosh x_m - \cos y}{\cosh x_p - \cos y}\right) - x_p\frac{\sinh x_p}{\cosh x_p - \cos y} + \right. \\ & \left. + x_m\frac{\sinh x_m}{\cosh x_m - \cos y} - 2xH\frac{1-\cosh x_m \cos y}{(\cosh x_m - \cos y)^2}\right] , \end{aligned} \tag{A.2.5}$$

$$F_{zz}(x,y) = \nu(F_{xx}(x,y) + F_{yy}(x,y)) . \tag{A.2.6}$$

A.3. Proportionality of SQUID-Signal and Magnetization

There are two different effects exploited by SQUID: quantization of the flux and the Josephson effect, which are discussed further in the following. Here, we will follow [CB04], which is very recommended for any theoretical question concerning SQUID. In quantum theory electrons are described by a phase φ, which displays the exponent of the wavefunction. Moreover, the expectation value of the momentum is given by:

$$\langle p \rangle = \nabla\varphi = \frac{1}{\hbar}\left(m\boldsymbol{v} + q\boldsymbol{A}\right) . \tag{A.3.1}$$

Here, m is the mass, q the electron charge and $\boldsymbol{A}$ the vector potential. With the aid of the Bohr-Sommerfeld quantization $2\pi k = \oint \nabla\varphi \,\mathrm{d}\boldsymbol{l}$ and the superconducting current density $\boldsymbol{j} = qn\boldsymbol{v}$, one obtains for a superconductor:

$$k\phi_0 = \mu_0\lambda_l^2 \oint \boldsymbol{j} \,\mathrm{d}\boldsymbol{l} + \phi\,, \tag{A.3.2}$$

with the London penetration depth $\lambda_l = (m/\mu_0 q^2 n)^{-1/2}$ of the order of micrometers, superconducting electron density n, the flux quantum $\phi_0 = \frac{h}{2e}$ and the magnetic flux ϕ caused by an external magnetic field. That means, that the change of an external field results in a very small superconducting current to guarantee the validation, which is the origin of the interference exploited by SQUID. On the other side, applying (A.3.1) to a superconductor-insulator-superconductor junction with a barrier smaller than the λ_l, the actual current is determined by the current over the insulator:

$$j_z = \frac{nq\hbar}{m}\left(\partial_z\varphi - \frac{2\pi}{\phi_0}A_z\right)\,. \tag{A.3.3}$$

Introducing a new phase δ, which will be the most important parameter, it becomes:

$$j_z = \frac{nq\hbar}{m}\partial_z\delta \qquad \text{with} \quad \delta = \varphi(z) - \frac{2\pi}{\phi_0}\int_0^z A_z \,\mathrm{d}z\,. \tag{A.3.4}$$

Now, it is possible to calculate the phase δ across a SQUID, consisting of a superconductive ring and two insulators, as illustrated in Fig. A.2:

$$\partial_x\delta \overset{!}{=} \delta_2 - \delta_1 = \frac{2\pi}{\phi_0}\left(\phi + \mu_0\lambda_l^2\left(\int_2^1 \boldsymbol{j}\,\mathrm{d}\boldsymbol{l} + \int_{1'}^{2'} \boldsymbol{j}\,\mathrm{d}\boldsymbol{l}\right)\right)\,. \tag{A.3.5}$$

The closed path integral of A_z was already transferred into the magnetic flux ϕ.

Due to time reversal, gauge invariance and strong convergence, the superconducting current can be Fourier transformed to:

$$j_s = j_0 \sin\delta\,, \tag{A.3.6}$$

which is named first Josephson relation. Differentiation with respect to time and application of induction law allows the derivation of the second Josephson relation:

$$\hbar\partial_t\delta = 2qU(t)\,, \tag{A.3.7}$$

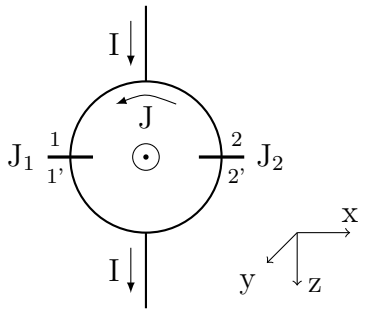

Fig. A.2.: *The sketch shows a dc-SQUID with two Josephson junctions J_1 and J_2. The superconducting current J flows within the device. The magnetic field points out of the plane.*

which leads to an oscillation of the current for a constant voltage.

Assuming perfectly similar Josephson junctions, no additional terms are required. Hence, integration over time of the measured voltage over the SQUID reveals the phase δ, which is according to (A.3.5) proportional to the flux. In other words, a SQUID is a quite sensitive flux-to-voltage converter.

$$\bar{U}(\text{actual SQUID signal}) \propto \delta \propto \phi(3.3.2) \propto \boldsymbol{B} \propto \boldsymbol{M} \tag{A.3.8}$$

Bibliography

[ALK+04] A. M. Andrews, R. LeSar, M. A. Kerner, J. S. Speck, A. E. Romanov, A. L. Kolesnikova, M. Bobeth, and W. Pompe. Modeling crosshatch surface morphology in growing mismatched layers. part ii: Periodic boundary conditions and dislocation groups. *J. Appl. Phys.*, 95:6032–6047, 2004.

[BH70] R. Baron and R. W. Hoffman. Saturation magnetization and perpendicular anisotropy of nickel films. *J. Appl. Phys.*, 41:1623–1632, 1970.

[BJ58] D. Berlincourt and H. Jaffe. Elastic and piezoelectric coefficients of single-crystal barium titanate. *Phys. Rev.*, 111:143–148, 1958.

[CB04] J. Clarke and A. I. Braginski. *The SQUID Handbook*. Wiley, 2004.

[DDHS05] M. Davis, D. Damjanovic, D. Hayem, and N. Setter. Domain engineering of the transverse piezoelectric coefficient in perovskite ferroelectrics. *J. Appl. Phys.*, 98:014102, 2005.

[Des10a] Quantum Design. SQUID VSM Application Note: Accuracy of the Reported Moment: Sample Shape Effects. `http://www.qdusa.com/sitedocs/appNotes/squid-vsm/1500-015.pdf`, Nov 2010.

[Des10b] Quantum Design. SQUID VSM User's Manual. Apr 2010.

[DHM68] H. Danan, A. Herr, and A. J. P. Meyer. New determinations of the saturation magnetization of nickel and iron. *J. Appl. Phys.*, 39:669–670, 1968.

[efu11] efunda. Thermal conductivities. `http://www.efunda.com/materials/elements/`, Mar 2011.

[EKJ+07] E. A. Eliseev, S. V. Kalinin, S. Jesse, S. L. Bravina, and A. N. Morozovska. Electromechanical detection in scanning probe microscopy: Tip models and materials contrast. *J. Appl. Phys.*, 102:014109, 2007.

[EMS06] W. Eerenstein, N. D. Mathur, and J. F. Scott. Multiferroic and magnetoelectric materials. *Nature*, 442:759–765, 2006.

[FBPR07] N. Farag, M. Bobeth, W. Pompe, and A. E. Romanov. Modelling of structural domains and elastic strain calculation in rhombohedral $La_{1-x}Sr_xMnO_3$ films on (110) $SrTiO_3$. *Philosophical Magazine*, 87:1478–6435, 2007.

[FEF+89] M. Fähnle, C. Elsässer, J. Furthmüller, R. Pawellek, E. H. Brandt, and M. C. Böhm. Local magnetic anisotropy and magnetostriction of amorphous ferromagnets. *Physica B: Condensed Matter*, 161:225–231, 1989.

[FF10] H. Fangohr and T. Fischbacher. Nmag - computational micromagnetism. `http://nmag.soton.ac.uk/nmag/`, Dez 2010.

[GBO+10] S. Geprägs, A. Brandlmaier, M. Opel, R. Gross, and S. T. B. Goennenwein. Electric fields controlled manipulations of the magnetiziation in $Ni/BaTiO_3$ hybrid structures. *Appl. Phys. Letters*, 96:669–670, 2010.

[Har99] U. Hartmann. Magnetic force microscopy. *Annu. Rev. Mater. Sci.*, 29:53–87, 1999.

[HGKM+05] D. C. Hurley, R. H. Geiss, M. Kopycinska-Müller, J. Müller, Read D. T., J. E. Wright, N. M. Jennett, and A. S. Maxwell. Anisotropic elastic properties of nanocrystalline nickel thin films. *J. Mater. Res.*, 20:225–231, 2005.

[HL82] J. P. Hirth and J. Lothe. *Theory of Dislocations*. Wiley, 2 edition, 1982.

[HS09] A. Hubert and R. Schäfer. *Magnetic Domains*. Springer, 3 edition, 2009.

[Hub70] A. Hubert. Stray-field-free and related domain wall configurations in thin magnetic films (ii). *physica status solidi (b)*, 38:699–713, 1970.

[Jun06] T. Jungk. *Untersuchung der Abbildungsmechanismen ferroelektrischer Domänen mit dem Rasterkraftmikroskop*. PhD thesis, Rheinische Friedrich-Wilhelms-Universität Bonn, 2006.

[Lab11] Argonne National Laboratory. Magnetic films. `http://www.msd.anl.gov/groups/mf/jmkerrcalc.php`, Mar 2011.

[Lee55] E W Lee. Magnetostriction and magnetomechanical effects. *Reports on Progress in Physics*, 18:184, 1955.

[LL85] L. D. Landau and E.M. Lifschitz. *Lehrbuch der Theoretischen Physik, Elektrodynamik der Kontinua.* Akademie Verlag, 1 edition, 1985.

[LL91] L. D. Landau and E.M. Lifschitz. *Lehrbuch der Theoretischen Physik, Elastizitätstheorie.* Akademie Verlag, 7 edition, 1991.

[MMF+09] J. McCord, I. Mönch, J. Fassbender, A. Gerber, and E. Quandt. Local setting of magnetic anisotropy in amorphous films by Co ion implantation. *J. Appl. Phys. D*, 42:055006, 2009.

[MS07] T. Maitland and S. Sitzman. Electron Backscatter Diffraction (EBSD) Technique and Materials Characterization Examples. In *Scanning Microscopy for Nanotechnology Techniques and Applications*, volume 14 of *Ferroelectrics*, pages 41–75. Springer, 2007.

[PLW+07] A.-B. Posadas, M. Lippman, F. J. Walker, M. Dawber, C. H. Ahn, and J.-M. Triscone. Growth and novel applications of epitaxial oxide thin films. In *Physics of Ferroelectrics*, volume 105 of *Topics in Applied Physics*, pages 219–304. Springer, 2007.

[RPS96] A. E. Romanov, W. Pompe, and J. S. Speck. Theory of microstructure and mechanics of the $\ldots a_1/a_2/a_1/a_2 \ldots$ domain pattern in epitaxial ferroelectric and ferroelastic films. *J. Appl. Phys.*, 79:4037–4049, apr 1996.

[SL98] B. A. Strukov and A. P. Levanyuk. *Ferroelectric Phenomena in Crystals.* Springer, 1 edition, 1998.

[Spa07] N. Spaldin. Analogies and differences between ferroelectrics and ferromagnets. In *Physics of Ferroelectrics*, volume 105 of *Topics in Applied Physics*, pages 175–218. Springer, 2007.

[SSD86] A. Schaefer, H. Schmitt, and A. Dörr. Elastic and piezoelectric coefficients of tssg barium titanate single crystals. In *Ferroelectrics*, volume 69 of *Ferroelectrics*, pages 253–266. Gordong and Breach Science, 1986.

[Sur11] SurfaceNet. Crystal properties. `http://surfacenet.de`, Mar 2011.

[TWH92] G. Traeger, L. Wenzel, and A. Hubert. Computer experiments on the information depth and the figure of merit in magnetooptics. *physica status solidi (a)*, 131:201–227, 1992.

[VV53] J. H. Van Vleck. Models of exchange coupling in ferromagnetic media. *Rev. Mod. Phys.*, 25:220–227, 1953.

[YK98] N. Yamamoto and A. Kitajima. Reflection electron microscopy of ferroelectric domain walls in batio$_3$. *Journal of Electron Microscopy*, 47:201–209, 1998.

[YS96] Chun-Yeol You and Sung-Chul Shin. Derivation of simplified analytic formulae for magneto-optical kerr effects. *Appl. Phys. Letters*, 69:1315–1317, 1996.

List of Figures

List of Tables

Acknowledgements

Within the last year, many scientists have contributed to my thesis, who I would like to acknowledge in the following. Without their support I would have never succeeded in my work.

Prof. Lukas Eng (Technische Universität Dresden), who offered me the diploma position and introduced me to the area of magnetoelectric coupling.

Prof. Rudolf Groß (Technische Universität München), who proposed the interest of the investigated system.

Dr. Oliver Mieth (Technische Universität Dresden), who introduced me to PFM and guided me during my thesis.

Dr. Denny Köhler (Technische Universität Dresden), who showed me the basics of MFM and offered discussion about the fundamental mechanisms.

Dr. Alexander Haußmann (Technische Universität Dresden), who was very helpful during writing the thesis.

Dr. Rudolf Schäfer (Leibniz-Institut für Festkörper- und Werkstoffforschung Dresden), who offered me the opportunity to measure the magnetic properties via MOKE imaging. I am really grateful for that.

Claudia Patschureck and Stefan Pofahl (Leibniz-Institut für Festkörper- und Werkstoffforschung Dresden), who introduced me to MOKE imaging and temporary assisted me.

Dr. Stephan Geprägs (Walther-Meißner-Institut Garching), who provided the first samples, showing interesting features.

Dr. Denys Makarov and Frau Cornelia Krien (Leibniz-Institut für Festkörper- und Werkstoffforschung Dresden), who provided the samples for the investigation of the dependence of deposition conditions.

Dr. Anja Wolter and Sebastian Gaß (Leibniz-Institut für Festkörper- und Werkstoffforschung Dresden), who offered me the opportunity to measure the saturation magnetizations via SQUID.

Thomas Kämpfe (Technische Universität Dresden), who took time for discussion.

Dr. Manfred Bobeth and Nayel Farag (Technische Universität Dresden), who shared their experience of the coherence technique with me.

Thanks to all other members of FERROIX and SPM2, who were interested in my topic.

Erklärung

Hiermit versichere ich, dass ich die vorliegende Arbeit ohne unzulässige Hilfe Dritter und ohne Benutzung anderer als der angegebenen Hilfsmittel angefertigt habe. Die aus fremden Quellen direkt oder indirekt übernommenen Gedanken sind als solche kenntlich gemacht. Die Arbeit wurde bisher weder im Inland noch im Ausland in gleicher oder ähnlicher Form einer anderen Prüfungsbehörde vorgelegt.

Robert Streubel
Dresden, 14. Juni 2011